Design of a Vehicular Liquefied Natural Gas Fuel Storage Vessel

by

Gregory Iuzzolino
B.A.Sc., University of British Columbia, 2003

A Thesis Submitted in Partial Fulfillment of the
Requirements for the degree of

MASTER OF APPLIED SCIENCE

in the Department of Mechanical Engineering

Supervisors: Dr. P.Wild, Dr. A. Rowe

Abstract

Liquefied natural gas (LNG) buses and trucks will require fuel storage vessels. In this report, an aluminum Insulated Pressure Vessel (IPV) capable of storing 135 kg of LNG is designed. The IPV is lighter than current stainless steel vessels, does not require an expensive composite overwrap, and has a seamless inner vessel.

Finite element models are developed and validated by modeling simple pressure vessel shapes with closed form mathematical expressions. These models are then used to perform a structural and thermal analysis of the IPV. Additional thermal analysis calculation methods for the IPV are developed to determine the IPV's heat leak, hold time, and boil off rate. Results indicate the IPV has lower heat leak and boil off rate, and higher hold time than current vessels. Sensitivity analysis is used to determine how the IPV performance and design is affected by changes in operating pressures and IPV dimensions.

Supervisors: Dr. P.Wild, Dr. A. Rowe, (Department of Mechanical Engineering)

Table of Contents

List of Tables

List of Figures

Notation

Dimensional

A	Area [m]^2
A_{plate}	Cross-sectional Plate Area [m]^2
A_{G10}	Cross-sectional G-10 Pin Area [m]^2
D	IPV inner diameter [m]
e	Eccentricity [1]
h	Depth [m]
L_{axial}	Axial length [m]
L_{block}	Valve Block Length [m]
$L_{bushing}$	Bushing Length [m]
$L_{closed\ end}$	Length of Closed End [m]
L_{cup}	ZD154 Liner Cup Length [m]
$L_{cylinder}$	Cylinder Length [m]
L_{dome}	Length of Dome Region [m]
L_{G10}	Length of G-10 Pin [m]
$L_{housing}$	Length of Pump Shaft Housing [m]
L_{IPV}	Length of IPV [m]
L_{liner}	Liner length [m]
L_{plate}	Length of Plate [m]
L_{shaft}	Length of Pump Shaft [m]
L_{tubing}	Tubing Length [m]
L_{ZD154}	ZD154 Liner Length [m]
r	Radius [m]
r_{ave}	Average internal radius of IPV inner vessel [m]
r_{axial}	Axial Radius [m]
$r_{housing}$	Pump Shaft Radius [m]
r_{in}	Inner Radius [m]
$r_{knuckle}$	Knuckle Radius [m]
r_{major}	Major Radius [m]
r_{minor}	Minor Radius [m]
r_{out}	Outer Radius [m]
r_{shaft}	Radius of Pump Shaft [m]
$r_{spherical}$	Spherical Radius [m]
S	Shape Factor [m]
S_{block}	Shape Factor for Valve Block [m]
S_{G10}	Shape Factor for G10 [m]
$S_{housing}$	Shape Factor for Pump Housing [m]
S_{plate}	Shape Factor for Plate [m]
S_{tubing}	Shape Factor for Tubing [m]
t	Wall Thickness [m]
$t_{cylinder}$	Cylinder Thickness [m]
t_{dome}	Dome Thickness [m]
t_{hold}	Hold Time [s]

Dimensional (cont)

t_o	Start time [s]
$t_{housing}$	Pump Shaft Wall Thickness [m]
θ	Angular Position [rad]
u	Independent variable [1]
u_{axial}	Axial Displacement [m]
V	Volume [L]
V_{dome}	Volume of material in dome region $[m]^3$
V_{liquid}	Liquid Volume [L]
V_{LNG}	LNG Volume [L]
V_{total}	Total Volume [L]
V_{ullage}	Ullage Volume [L]
x	Position [m]

Structural

v	Poisson's Ratio [1]
E	Elastic Modulus [GPa]
g	Gravitational acceleration [m s^{-2}]
k	Independent variable [GPa][m]^{3}
λ	Independent variable [1]
$M\phi$	Meridonial Bending Moment [N]
m	Mass [kg]
$m_{boil\ off}$	Boil off rate [kg s^{-1}]
m_{LNG}	LNG mass [kg]
m_{liquid}	Liquid Mass [kg]
m_{total}	Total Mass [kg]
m_{vapor}	Vapor Mass [kg]
ρ	Density [kg m^{-3}]
ρ_{Al}	Aluminum Density [kg m^{-3}]
ρ_{LNG}	LNG Density [kg m^{-3}]
ρ_{liquid}	Liquid Density [kg m^{-3}]
ρ_{vapor}	Vapor Density [kg m^{-3}]
ρ_{Steel}	Steel Density [kg m^{-3}]
$\rho_{storage}$	Fuel Storage Density [kg m^{-3}]
ρ_{total}	Total Density [kg m^{-3}]
P	Internal Vessel Pressure [psi]
$P_{hydrostatic}$	Hydrostatic Pressure [psi]
$P_{failure}$	Vessel Failure Pressure [Pa]
$P_{collapse}$	Vessel Collapse Pressure [Pa]
σ_{axial}	Axial Stress [Pa]
σ_{θ}	Hoop Stress [Pa]
σ_{Φ}	Meridonial Stress [Pa]
σ_{radial}	Radial Stress [Pa]
σ_{u}	Ultimate Tensile Stress [Pa]
$\sigma_{Von\ Mises}$	Von Mises Stress [Pa]
σ_{y}	Yield Stress [MPa]
SF	Factor of Safety [1]
$Weight_{Al}$	Weight of Aluminum IPV [kg]
$Weight_{Steel}$	Weight of Steel IPV [kg]
X	Vapor mass fraction [1]

Thermal

CTE	Coefficient of Thermal Expansion [μm m^{-1} K^{-1}]
C_S	Coefficient for Mylar MLI [Wm$^{0.56}$K^{-2}]
ε	Emissivity [1]
h_f	Enthalpy in Liquid State [kJ kg^{-1}]
h_g	Enthalpy in Gas State [kJ kg^{-1}]
h_{fg}	Change in enthalpy from Liquid to Gas State [kJ kg^{-1}]
K	Thermal Conductivity Integral [1]
K_H	Thermal Conductivity Integral (External End) [1]
K_C	Thermal Conductivity Integral (Internal End) [1]
k_t	Effective Thermal Conductivity [Wm^{-1}K^{-1}]
$m_{boil\ off}$	Boil off rate [g h^{-1}]
N	Number of MLI Layers [1]
Q	Heat Leak [W]
$Q_{housing}$	Heat Leak for Pump Housing [W]
Q_{MLI}	Heat Leak for MLI [W]
Q_{plate}	Heat leak for plate [W]
Q_{shaft}	Heat Leak for Pump Shaft [W]
$Q_{supports}$	Heat Leak for Supports [W]
Q_{total}	Total Heat Leak [W]
$Q_{valve\ block}$	Heat Leak for Valve Block [W]
R	Thermal Resistance [KW^{-1}]
$R_{valve\ block}$	Valve Block Resistance [KW^{-1}]
$R_{bushing}$	Bushing Resistance [KW^{-1}]
R_{pins}	Pin Resistance [KW^{-1}]
R_{plate}	Plate Resistance [KW^{-1}]
R_{G10}	G10 Resistance [KW^{-1}]
σ	Stefan Boltzman Constant [Wm^{-2} K^{-4}]
T	Temperature [K]
T_H	Ambient Temperature [K]
T_C	Internal Vessel Temperature [K]
TC_{outer}	Temperature of External End of Outer Valve Block [K]
TC_{inner}	Temperature of External End of Inner Valve Block [K]
TH_{G10}	Temperature of External End of Bushing [K]
TC_{G10}	Temperature of Internal End of Bushing [K]
T_{INT}	Intermediate Temperature [K]
U	Internal Energy [J]
u	Specific Internal Energy [J kg^{-1}]

Chapter 1

Introduction

1.1 Background

Modern vehicles rely primarily on petroleum based fuels such as gasoline and diesel. These fuels produce over two Gigatonnes of greenhouse gases and particulate matter every year, and are becoming more expensive and difficult to obtain [1]. Natural gas is more evenly distributed globally than crude oil, which may provide some energy security [2]. In North America there are substantial natural gas reserves and a developed natural gas distribution system.

Natural gas is a more abundant and cleaner burning alternative fuel [1]. Natural gas vehicles produce smaller quantities of greenhouse gases and pollution compared to equivalent gasoline or diesel vehicles. Studies have found that natural gas powered vehicles produce, on average, 70% less carbon monoxide, 89% less non-methane organic gas, and 87% less NO_x than traditional gasoline powered vehicles [1, 3].

The large global reserve of natural gas could be used in the transportation sector. As of 2002, natural gas accounted for over 21% of the world's total primary energy supply while petroleum accounted for 35% [2]. The transportation sector alone accounted for 66% of the total U.S. petroleum consumption (1997) [4]. In contrast, all alternative fuels together account for less than 0.22% of total fuel currently being used by vehicles [5].

Natural gas has been extensively tested in vehicles as a compressed gas or cryogenically stored liquid. Liquefied natural gas (LNG) has several additional benefits compared to compressed natural gas (CNG). LNG has a relatively high energy density of 7216 Wh/L compared to 4000 Wh/L for CNG at 20.7 MPa (3000 psi), and 9000 Wh/L for gasoline [6].

Nevertheless, natural gas has many disadvantages which must be addressed before widespread adoption can occur. Natural gas exists as a vapor at ambient temperatures and must be compressed to high pressures (>248 Bar) or liquefied to achieve an adequate energy density for desired vehicle range [15]. This adds the additional costs of compression and liquefaction to the product. Additionally, LNG is a cryogenic liquid and requires low storage temperatures of roughly 115 K [4]. Clearly, specialized pressure vessels are required to store fuel as CNG or LNG.

Current insulated pressure vessels (IPVs) used for the storage of liquefied natural gas (LNG) suffer from a number of deficiencies. They are costly, heavier than gasoline and diesel tanks, and have limited hold-times (length of time prior to venting). If a low-cost, lightweight, improved performance LNG storage vessel could be manufactured, it would give vehicle manufacturers more incentive to adopt LNG technology into their fleets.

Dynetek Industries is producing tanks consisting of high-pressure aluminum liner vessels with composite overwrap for storage of natural gas. The Dynetek aluminum liners appear to be ideal for LNG storage since they are lighter than current stainless steel vessels, and are seamless.

1.2 Objectives

The objectives of the current research are to design an aluminum IPV for LNG based on the designs of the liners used in the Dynetek composite-wrapped pressure vessels. The performance and size of the vessel is to be comparable to existing vehicular LNG tanks manufactured by companies such as Taylor Wharton.

1.3 Methodology and Outline

The research objectives are achieved using the following methodology. In Chapter 2, various existing liquefied and compressed natural gas on-vehicle storage systems are reviewed. The vessel designs provide ideas for the various insulation, fuel delivery strategies, and materials that could be used to construct an IPV. The vessel costs help determine the cost needed to build an IPV. Finite element (FE) analysis is used to determine IPV vessel stresses. The FE technique is initially used in Chapter 3 to analyze common pressure vessel shapes. The FE results are then validated by comparing the vessel's FE derived stresses to closed-form solutions. The FE analysis method is further validated by analyzing two current Dynetek liners in Chapter 4. IPV inner and outer vessel designs based on the design of Dynetek liners are then developed in Chapter 5 using Dynetek manufacturing processes. FE and thermal analysis is conducted on the IPV design to ensure it satisfies the design criteria in Appendix A1.1. In Chapter 6, a sensitivity analysis is conducted on the IPV to determine how the IPV performance and design is affected by changes to variables such as vessel length, thickness, and operating pressure.

Chapter 2

Literature Review

2.0 Introduction

The use of hydrogen and natural gas as a vehicle fuel is expected to increase, but fuel storage is constantly being identified as a technical hurtle [1,3]. Current fuel storage vessels are heavy and expensive. Several insulated liquefied and compressed natural gas and hydrogen on-vehicle storage vessel designs are investigated. Existing designs provide ideas for the various insulation, fuel delivery strategies, and materials that could be used to construct an IPV. The vessel's costs help determine the cost needed to build an IPV. The performance and validation tests discussed help determine required tests needed to validate IPV design.

2.1 Compressed Natural Gas and Hydrogen Storage

Compressed hydrogen and natural gas require specialized vessels capable of withstanding high pressures. Some vessel designs contain aluminum or stainless steel liners and a composite wrap [11,20] while others use high molecular weight polymer liners impermeable to hydrogen and wrapped with a carbon fiber shell and a hard fiber/resin external shell [21]. These vessels are typically much more expensive than liquefied natural gas and hydrogen storage vessels.

The disadvantages of storing fuel using compressed gas are that it is an inefficient use of space aboard a vehicle. Pressures between 35 and 70 MPa are required to overcome storage inefficiencies [21]. Compressed gas vessels can suffer from permeation losses (particularly with synthetic liners) and become difficult to refuel at higher pressures. Compressed hydrogen has permeation losses through the vessel that are 4 times greater than natural gas and many metals suffer hydrogen embrittlement, which increases with increasing pressure [20].

Many companies and research institutions are developing high pressure natural gas and hydrogen storage vessels for vehicular use. The advantages of compressed gas storage compared to liquid storage are that pumps are not required to inject fuel into an internal combustion engine or fuel cell, the vessels do not suffer fuel venting when idle, and ambient temperature operation is possible. The following are examples of several developed pressure vessel designs.

2.1.1 General Dynamics

The General Dynamics natural gas/hydrogen tank [22] is an all composite design consisting of a durable plastic liner fully wrapped with epoxy impregnated carbon and glass fiber. The liner is made from high density polyethylene and has two aluminum end bosses. The plastic liner eliminates the limitations of fatigue cycle life experienced by metal liners. The carbon fiber provides a high strength to weight performance, excellent fatigue properties, insensitivity to environmental degradation and performance reliability. Glass fiber enhances the durability of the fuel tank. An external fiberglass over-wrap protects the pressure vessel from chemical or environmental attack and abrasion from handling. Foam inserts are placed over the tank dome sections separating the over-wrap from the vessel. The reduced thickness in the dome regions are more susceptible to damage if dropped or impacted. The high density polyethylene liner and the composite shell are compatible with hydrogen, and the aluminum end bosses do not degrade in high pressure hydrogen.

Vessels can be packaged to conform to a non-cylindrical cavity such as a traditional gasoline fuel tank compartment. The natural gas vehicle tanks can also be adapted for compressed hydrogen with operating pressures of 350 bar.

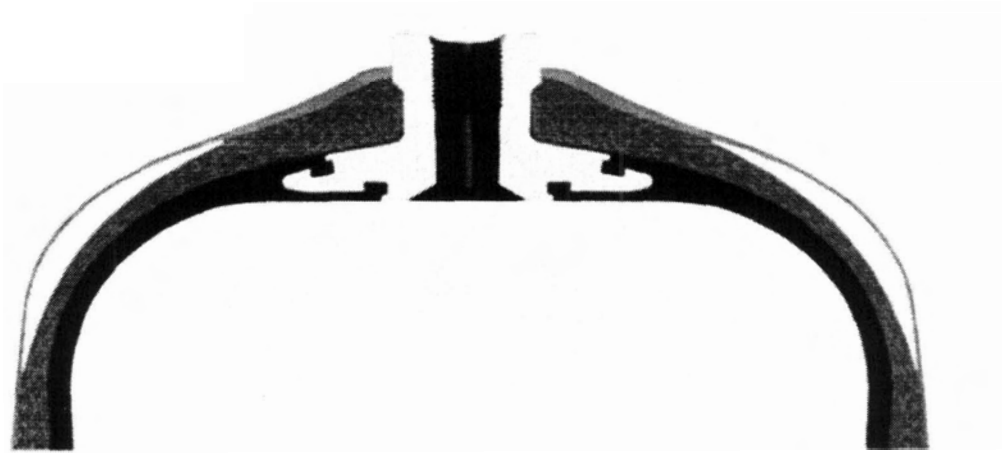

Figure 2.1: Section view of dome portion of General Dynamics Vessel [22]

2.1.2 Thiokol

Thiokol's unique conformable hydrogen tank design concept is shown in Figures 2.2-2.3 [23]. Thiokol's tank uses plastic liners, aluminum polar bosses and carbon fiber filament wound composites. The conformable tank design is capable of storing 11.3% of its total weight as hydrogen, which is higher than values attainable by traditional cylindrical tanks. Thiokol's 5000 psi tank has a 68 liter water volume. Tank wall thickness and weight are decreased by using hoop and helical composite layers. The tank burst at 10950 psi, giving a safety factor of 2.19. Internal web reinforcement provides internal support for individual cells.

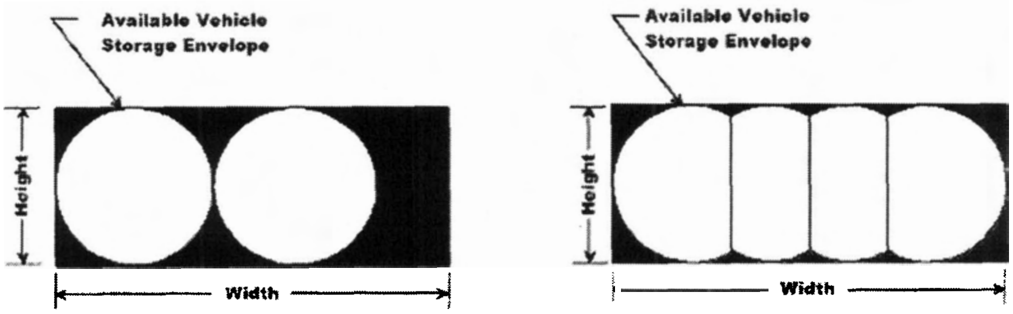

Figure 2.2: Cylinder versus conformable tank in a rectangular envelope [23]

Figure 2.3: Thiokol Conformable Hydrogen Tank [23]

2.1.3 Quantum Technologies

Quantum technology's compressed hydrogen tank is a 350 bar composite tank with polymer liner. It has a burst pressure greater than 790 bar [24], giving a factor of safety of 2.26 against burst.

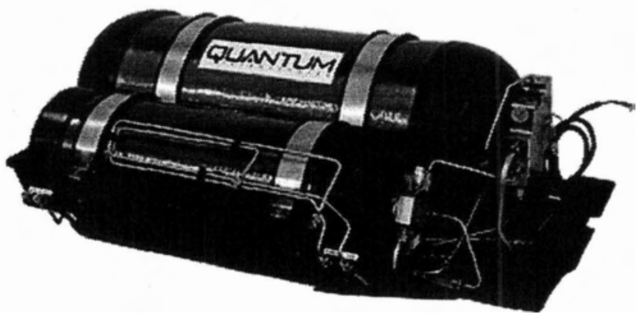

Figure 2.4: Quantum Technologies Compressed Hydrogen Tank [24]

2.2 Liquid Natural Gas and Hydrogen Storage

Liquefied natural gas and hydrogen are stored in insulated pressure vessels (IPV). The basic design is a double walled vessel consisting of an inner vessel used for fuel storage and an outer vessel housing. An ullage volume is often used to ensure there is an expansion space available to limit the rate of pressure increase. The IPV is insulated by maintaining a vacuum between the two vessels and wrapping multi-layer insulation around the inner vessel. Other IPV features include connections for filling and withdrawing fuel, and a pressure relief valve.

There are several disadvantages with LNG and LH2 storage. Heat leakage into the pressure vessel vaporizes some of the liquid, and as pressures rise, losses to the environment can occur. Another disadvantage is that the fuel pressure and density need to be increased so that fuel can be injected into an internal combustion engine or fuel cell. Current vessels are typically constructed using stainless steel, and tend to be heavier than tanks used to store petroleum based fuels.

There are several advantages with LNG and LH2 storage. High strength storage vessels are not required since operating pressure is much lower than for compressed gas storage tanks, and these vessels are sometimes less expensive than compressed natural gas and hydrogen storage vessels since they do not require a composite overwrap to increase vessel strength [11,18].

Many companies and research institutions are developing vessels for the storage of LNG and LH_2 for vehicular use. The following are examples of several developed pressure vessel designs.

2.2.1 Linde-AG

Linde has been designing cryogenic vessels since the sixties and has supplied more than 10,000 tanks with sizes from 600 litres to 300,000 litres. More recently they have been developing smaller cryogenic vessels for use in vehicles. A patent application has been filed for an efficient re-cooling system (CoolH$_2$ system) that minimizes evaporation losses. This innovation significantly extends the time before evaporation losses occur. When the vehicle is in operation, this time can be extended further.

In the CoolH$_2$ system, the surrounding air is drawn in, dried, and then liquefied by the energy released as the hydrogen increases in temperature. The cryogenically liquefied air (-191°C) flows through a cooling jacket surrounding the inner tank which acts as a heat absorber. This leads to a significant delay in the temperature increase of the LH$_2$ and is a sensible use for the energy stored in the liquid hydrogen when being consumed by the vehicle. Linde claims that since the cooling system can be accommodated in the existing insulating layer of the tank, it does not affect the tank size [13]. It does, however, contribute to tank complexity and overall cost. Figure 2.5 shows the CoolH$_2$ tank [13].

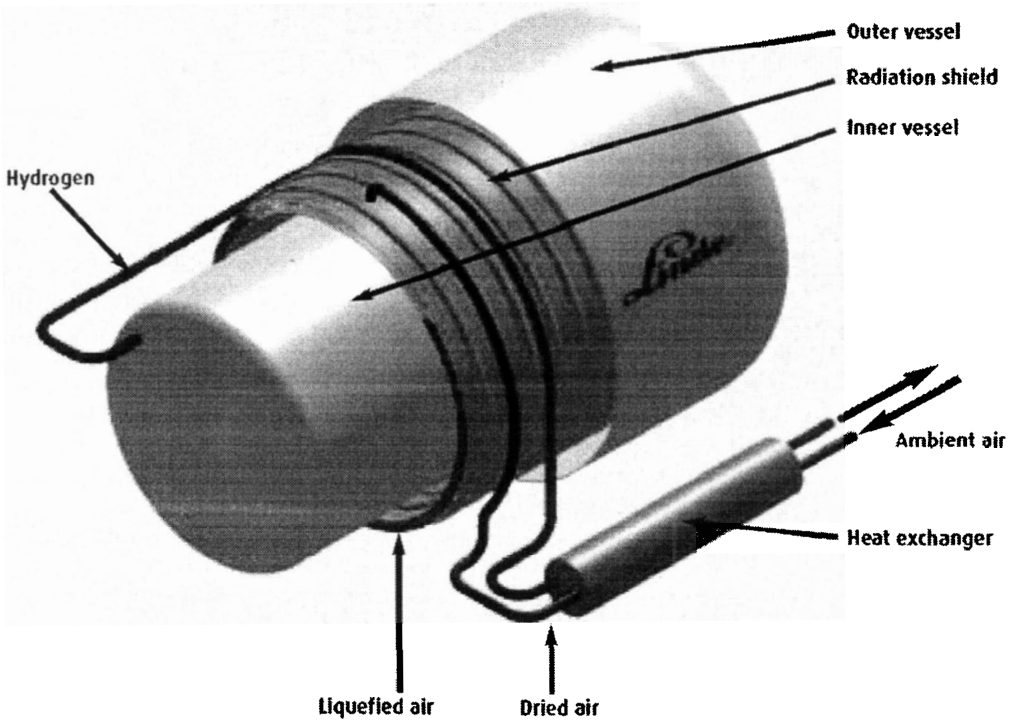

Figure 2.5: Linde-AG LH_2 Fuel Tank [13]

2.2.2 Magna Steyr

Magna Steyr, in cooperation with the BMW Group, was the first company to develop a liquid-hydrogen tank system for vehicular use. Magna Steyr's latest tank stores hydrogen in its liquid form at a temperature of 20 K and under low pressure. Table 2.1 shows technical data for the LH_2 tank [14]. In the future, Magna Steyr plans to develop freeform tanks, reduce tank weight, and optimize the isolation/active cooling system design.

Table 2.1: Technical Data for the Magna Steyr Liquid Hydrogen Tank

Design	Double-walled cylinder tank
Material	Inner and outer tank of austenitic steel
Storage	Liquid hydrogen at –253 °C
Volume of Hydrogen	Approx. 9.5 kg (equivalent to 50 L of gasoline)
Insulation	MLI with high vacuum (10^{-9} bar) between the inner/outer tanks
Inner tank support	Coaxial tubes of fiber-glass reinforced plastic
Safety	Crash test accelerations up to 30 G
Tank volume	Approx. 170 L
Weight	Approx. 145 kg (empty)
Target boil-off rate	Under 1 % per day when vehicle is idle for about 15 days
Application	Energy supply for automobiles with internal combustion engine and fuel-cell technology

2.2.3 The Lawrence Livermore National Laboratory

The Lawrence Livermore National Laboratory (LLNL) has been involved with the development of cryogenic vessels, specifically LH_2 vessels, in conjunction with Structural Composites Inc and Sunline Transit for use in mobile applications. Patent No. 6,708,502 has been granted to the LLNL for its pressure vessel design. The tank design can contain cryogenic fluids as well as compressed gases at cryogenic or ambient temperatures. The patent also details the tank structure assembly that would keep the vacuum intact. Of particular relevance is the use of a composite wrapped aluminum liner as the inner vessel which allows high pressure storage that the other liquid storage vessels cannot achieve. Out-gassing introduces gas particles into the evacuated space. Substances known as getter materials are used to adsorb residual gas and maintain the high vacuum required.

LLNL's first attempt at building a double-walled cryovessel is shown in Figure 2.6 [15]. This vessel is a 1/5 scale model and stores approximately 1 kg of hydrogen. Features of this tank design include knife-edge vacuum seals, radial and longitudinal supports, and fuel lines leading directly to the exterior.

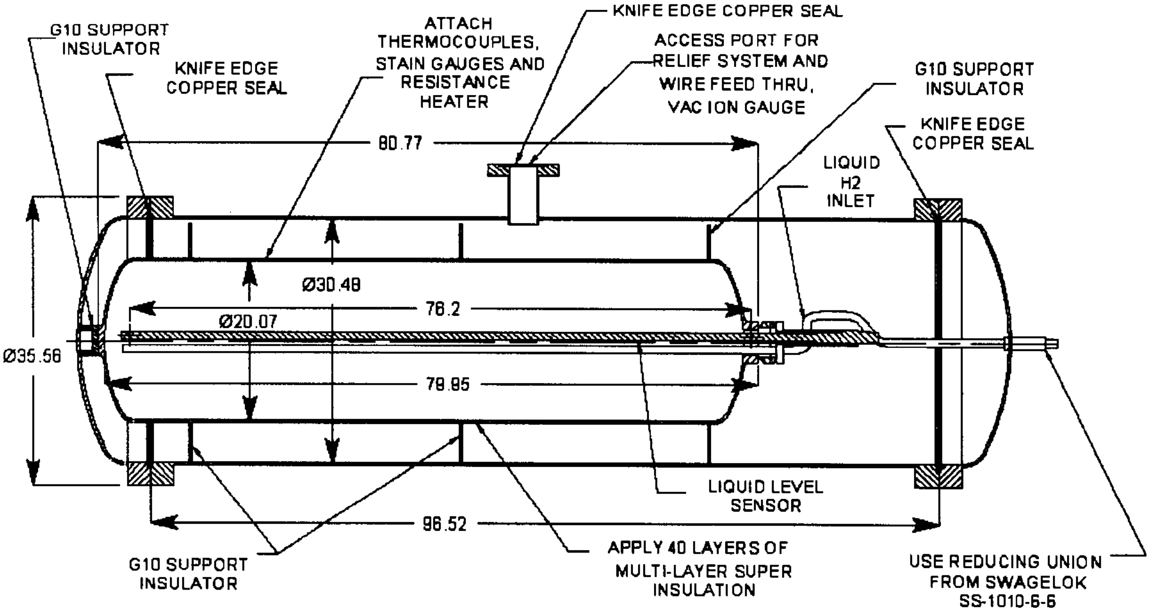

Figure 2.6: LLNL Generation 1 Tank [15]

LLNL made some changes in its second attempt at a cryovessel. The most notable change was that the fuel lines were wrapped around the tank in a helical fashion, creating a long heat conduction path and reducing the heat flux into the tank. Figure 2.7 shows the second generation tank [15]. A vapour shield has been incorporated into the second generation design to further reduce the heat flux to the inner vessel. The vapor shield is required since radiation heat leaks are higher for LH_2 vessels than for LNG vessels since LH_2 is stored at a lower temperature.

Currently, LLNL is testing their 2nd generation tank in conjunction with SunLine Transit. All the necessary performance and certification tests were completed and they have installed the vessel on several vehicles. Safety, performance and durability tests are being conducted and a next generation tank is in development.

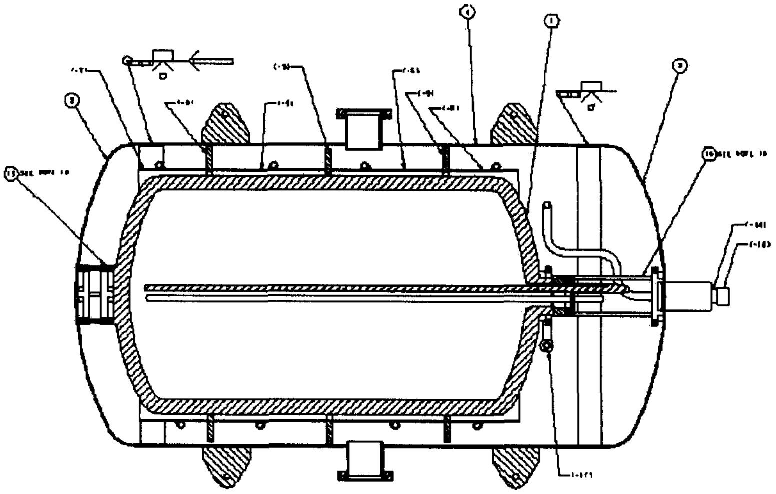

Figure 2.7: LLNL Second Generation Tank [15]

2.2.4 Chart Industries

Chart Industries' NexGen division produces onboard LNG tanks and provides small scale fueling stations to service these tanks. The cost for one of Chart's smallest tanks (177 litres) was quoted as roughly $8000 US [16]. Figure 2.8 shows the Chart LNG tank system. The numbers on the diagram correspond to the following components [17]:

1 – LNG dispenser
2 – Top fill
3 – Fuel receptacle
4 – Fuel gauge
5 – Vapour space
6 – Economizer regulator
7 – Heat exchanger
8 – Over pressure regulation

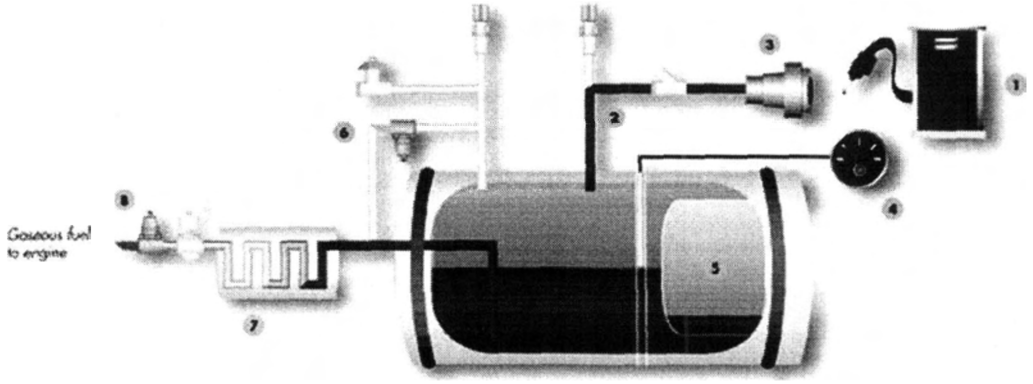

Figure 2.8: Chart LNG Tank System [16]

2.2.5 Taylor-Wharton

Taylor-Wharton produces LNG fuel tanks and hydrogen fuel tanks. The LNG vehicle fuel tanks are double-walled vacuum insulated pressure vessels, with the inner vessel designed to safely operate at temperatures as low as -195 °C and pressures up to 230 psig. The inner vessel and outer jacket are constructed of type 304 stainless steel. The tanks have been designed to not require venting for a period of three days after being filled to 100% net capacity. Venting occurs when heat absorption causes the fuel pressure to reach the vent pressure. Once venting begins, the rate of venting is 1% nominal per day by weight, based on the full weight of the fuel. A pressure control system reduces tank pressure when it exceeds set limits, and is adjustable to accommodate engine manufacturers' requirements for adequate fuel pressure. Figure 2.9-2.10 illustrate the Taylor-Wharton LNG fuel tank [18]. Technical specifications for Taylor-Wharton LNG-119V model IPV are outlined in Table 2.2 [18].

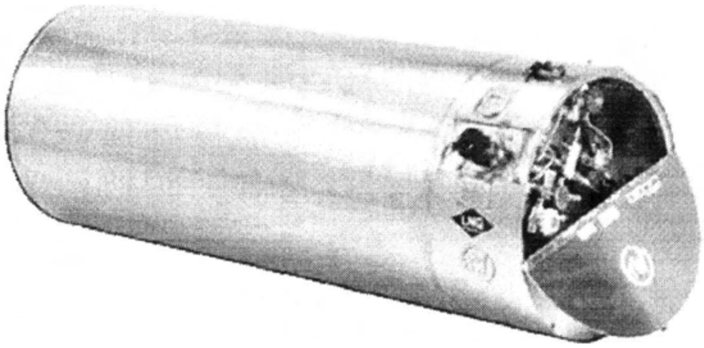

Figure 2.9: Taylor-Wharton LNG Fuel Tank [18]

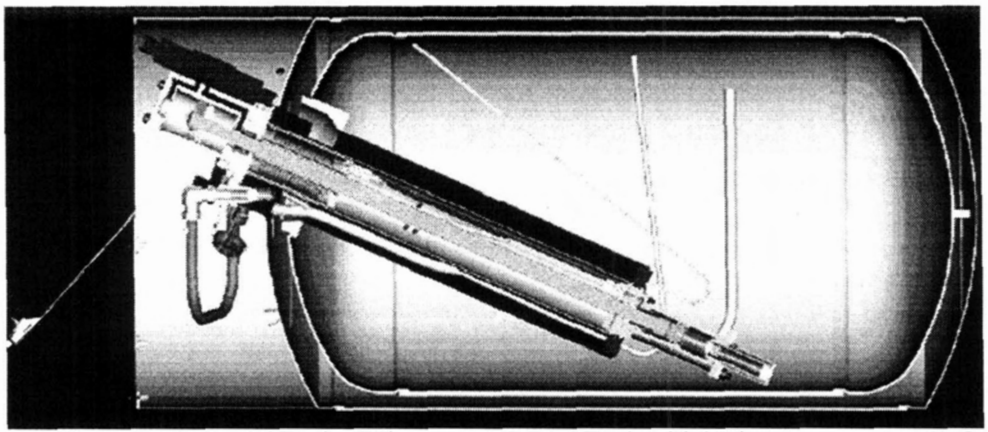

Figure 2.10: Section view of Taylor-Wharton LNG Fuel Tank with high pressure pump [18]

Table 2.2: Taylor-Wharton LNG Fuel Tank Specifications

Model	**LNG-119V**
Weight Empty	254 kg (560 lbs)
Weight Full	400 kg (880 lbs) (Assuming an LNG density of 420kg/m^3).
Liquid Container:	
Gross Volume	450 L (119 Gallons)
Net Volume	404 L (107 Gallons)
Material Specification	ASTM A-240 Type 304 stainless steel
Jacket:	
Material Specification	ASTM A-240 Type 304 stainless steel
Safety Devices:	
Primary Relief Valve	230 psig
Secondary Relief Valve	350 psig
Design Specifications	DOT-4L 200psig / NFPA 57 / SAE J2343

2.2.6 Messner Company

Messner's liquid hydrogen tank [19] consists of inner and outer vessels separated by a high grade super insulation. The tank is 5 m long and has a diameter of 420 mm. The prototype is built completely from stainless steel and stores 350 L of liquid hydrogen at a maximum operating pressure of 5 bar. The tanks have connections for filling, a withdrawal and a pressure relief valve, and a liquid level sensor and pressurization device. Energy densities of up to 22 MJ/kg of tank and evaporation rates of 1% per day are possible. During normal vehicle operation, no fuel losses are experienced. The tank is pressurized to transfer liquid hydrogen using an electric heater.

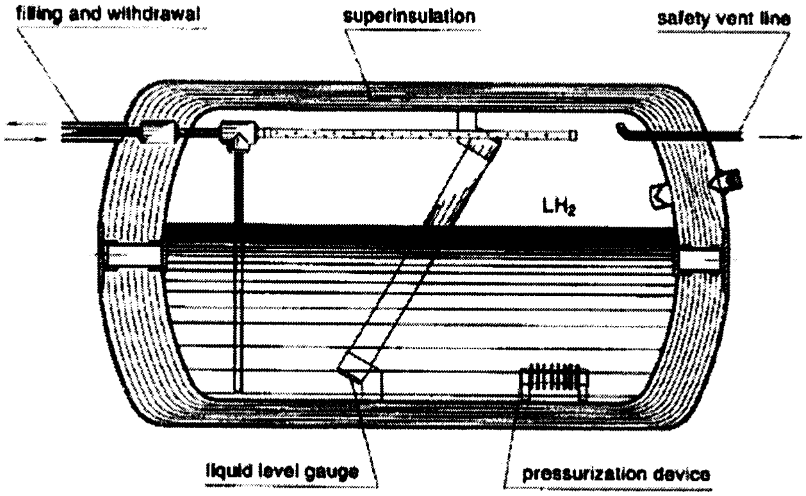

Figure 2.11: Messner company mobile liquid hydrogen unit [19].

2.2.7 University of Victoria

The University of Victoria (UVic) IPV design (Figure 2.12) was developed in 2004 as part of a feasibility study [12].Technical specifications for the UVic IPV model are outlined in Table 2.3. The IPV design uses a Dynetek ZD154 liner (19.9"OD x 55" LG) as the inner vessel and a Dynetek ZM180 liner (21.7"OD x 75" LG) as the outer vessel. The inner vessel is to be supported within the outer vessel using valve blocks that insert into the ports of both tanks which are then separated by a G-10 sleeve to reduce heat flux to the inner vessel. There is also a G-10 pin at the opposite end of the tank that fits into a steel plate. To provide a gross storage volume comparable to the current ~400 L tanks used by Westport, the Dynetek's ZD154 liner lengths would have to be increased by approximately 80-90 cm. It is envisaged that the ullage volume would be manufactured by inserting and welding a divider plate in the seamless shell (an orifice would be drilled through the liner to connect the two). The UVic IPV is the only known vessel constructed entirely from aluminum which makes it significantly lighter than current stainless steel vessels. The IPV is also much less expensive than composite tanks and should have a vacuum performance equivalent to or better than current stainless steel LNG tanks since outgassing of composite material is not an issue. Other benefits of the IPV design include a heat leak (6.5 W) that is much lower than current vessels, and a hold time (10 days) that is higher than current vessels. In Chapters 5-6, a newer version of the UVic IPV design will be developed that can store fuel volumes comparable to current Taylor Wharton and Chart Industry tanks. The redesigned IPV will consist of an extended length inner and outer vessel. The design of other IPV components will not be discussed.

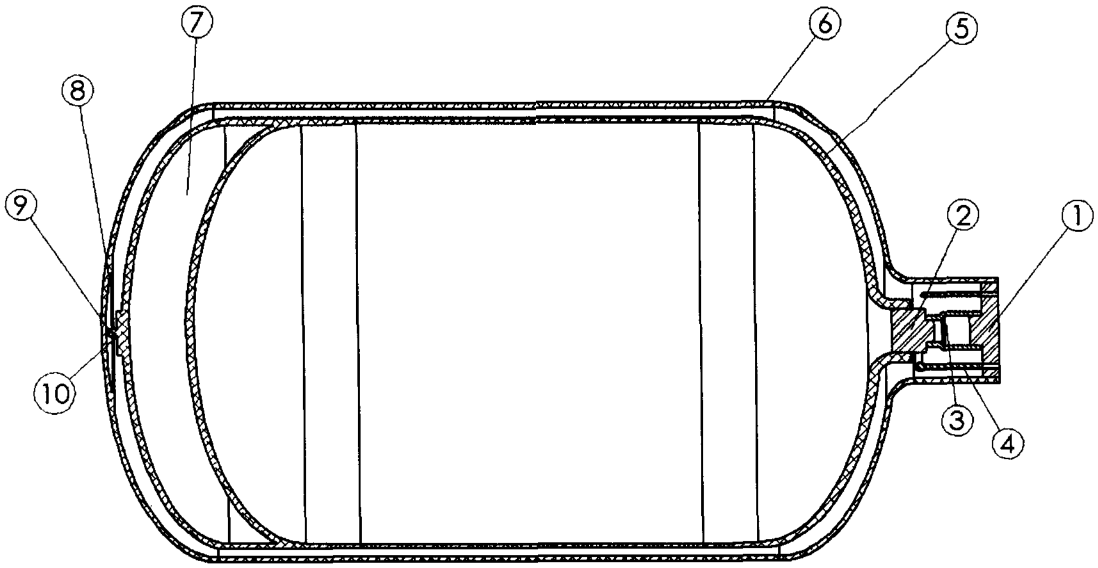

Figure 2.12: Section view of the University of Victoria IPV design [12].

Table 2.3: List of IPV components with description

	Component	Material	Description
1	Outer Port Block	Stainless Steel 304	Valve block components used to connect the inner and outer vessels together at their port boss location.
2	Inner Port Block	Stainless Steel 304	
3	G-10 Sleeve	G-10	
4	Fuel Lines (Input/Output)	Stainless Steel 304	The fuel input line is used to fill the tank with LNG. The fuel output line is used to transport fuel to the vehicle's engine
5	Inner Vessel	Aluminum 6061-T6	Used to store fuel for the IPV
6	Outer Vessel	Aluminum 6061-T6	The IPVs external housing
7	Ullage Space	Aluminum 6061-T6	Used to store excess fuel that transfers from the inner vessel when it becomes full
8	Support Plate	Stainless Steel 304	Rear support components used to support the inner vessel's closed end
9	G-10 Support Pin	G-10	
10	Spring	Stainless Steel 304	Used to compensate for thermal expansion occurring due to expansion and contraction of the inner liner

2.2.8 Other Companies

Other companies developing cryogenic tanks include Air Liquide, Sierra Lobo and Ball Aerospace. Air Liquide is developing LO_2 and LH_2 vessels for aerospace applications. Sierra Lobo is developing systems for storage and delivery of liquid hydrogen and oxygen for on-board as well as large scale refueling stations. Sierra Lobo is developing the "No-Vent Liquid Hydrogen Storage and Delivery System" for ground transportation vehicles. Ball Aerospace is primarily involved with aerospace applications of their LO_2 and LH_2 vessels.

2.3 Summary

The review of existing IPV designs in this chapter provided information that will facilitate design of the IPV discussed in Chapters 5 and 6. The IPV being developed will be used for low pressure storage of LNG. Therefore, the composite overwrap that is typically required for high pressure storage will not be required. No previous aluminum IPV designs with a seamless inner vessel were found. Therefore the IPV design discussed in Chapters 5 and 6 represents an opportunity to develop a unique lighter weight vessel design. The only LNG storage vessels that were found for vehicular applications were developed by Taylor Wharton and Chart Industries. The IPV design being developed will need to be lighter and less expensive than current tanks if it is to be a feasible LNG storage alternative. In addition, it will need to satisfy the design criteria shown in Appendix A1.1.

Chapter 3

Finite Element Model Development and Validation

3.0 Introduction

Simple pressure vessel shapes, for which closed-form solutions are available, are modeled using the commercial finite element (FE) code, ANSYS [25]. Possible elements that could be used for the FE model are then investigated and a mesh refinement study is used to determine a suitable mesh density for modeling pressure vessels. The results of the FE analyses are compared with the closed form analyses to validate the FE model results obtained in Chapters 4 and 5.

3.1 Modeled Pressure Vessels

The four pressure vessel geometries that were analyzed are a hemispherical dome, an ellipsoidal dome, a torispheroidal dome, and a cylinder with a hemispherical end cap. The dimensions and material properties used in the models were based on those of the Dynetek ZD154 aluminum liner. Relevant values are shown in Table 3.1.

Table 3.1: Summary of Modeled Pressure Vessels Dimensions and Material Properties

Region	**Value**
Outer Radius [mm]	253
Wall Thickness [mm]	5.25
Modulus of Elasticity [GPa]	70
Poisson's Ratio	0.3
Material	Aluminum 6061-T6
Yield Stress [MPa]	290

A pressure of 1.38 MPa (200 psi) was applied to each modeled liner. This pressure is the proposed maximum allowable working pressure (MAWP) for the Dynetek liners in the context of the insulated pressure vessel.

The hemispherical vessel shown in Figure 3.1 has an outer radius r_{sphere} and a uniform wall thickness t.

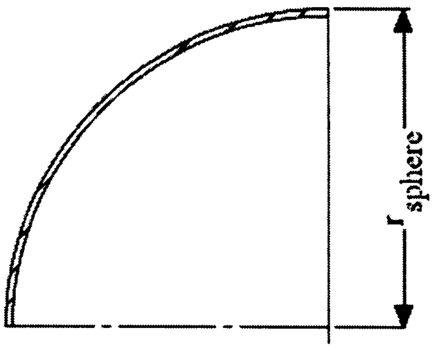

Figure 3.1: Hemispherical Dome Vessel

The ellipsoidal vessel shown in Figure 3.2 has a major radius r_{major}, a minor radius r_{minor}, and a wall thickness t. Values for the variables are given in Table 3.2.

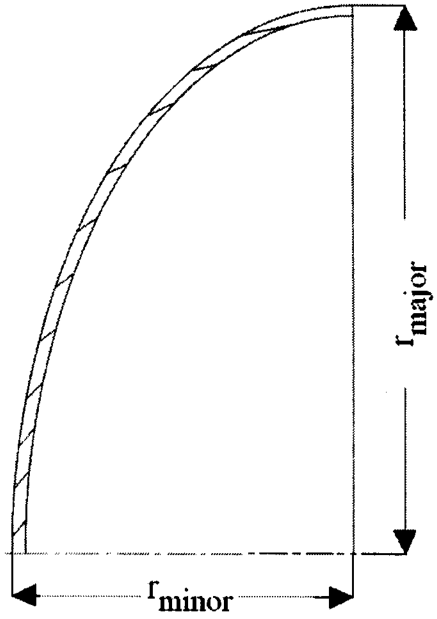

Figure 3.2: Ellipsoidal Dome Vessel

Table 3.2: Variables used to define Ellipsoidal Dome Vessel

Variable	Value [mm]
r_{major}	253
r_{minor}	135
t	5.25

The torispheroidal vessel shown in Figure 3.3 was modeled with a spherical knuckle region radius $r_{knuckle}$, a spherical region radius r_{sphere}, an outer pressure vessel radius L, and wall thickness t. The angle θ is defined in Equation 3.1. Values for the variables are given in Table 3.3.

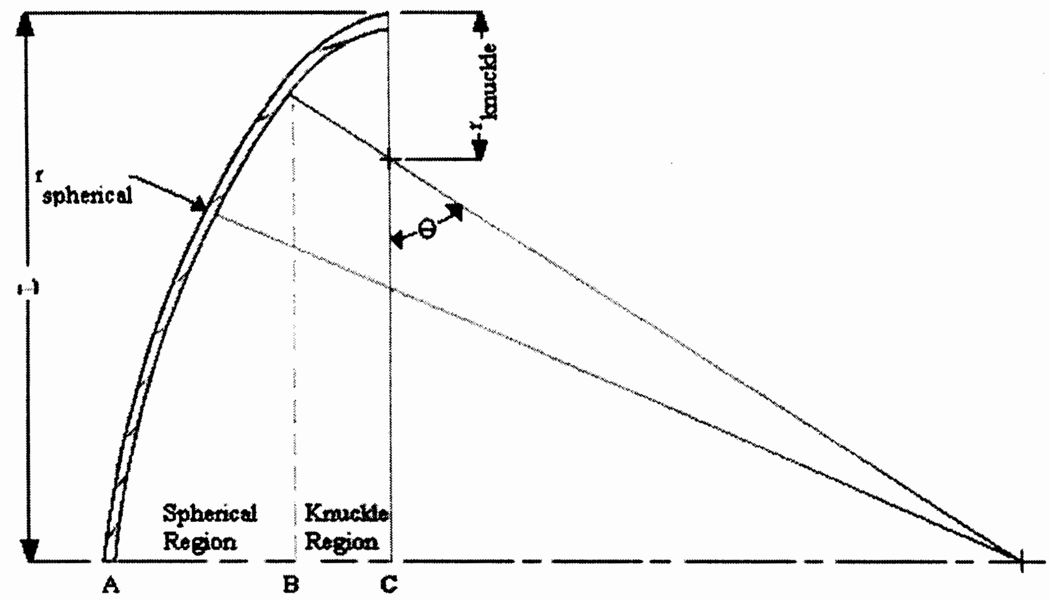

Figure 3.3: Torispheroidal Dome Vessel

$$\theta = \cos^{-1}\left(\frac{L - r_{knuckle}}{R - r_{knuckle}}\right) \tag{3.1}$$

Table 3.3: Variables used to define Torispheroidal Dome Vessel

Variable	Value [mm]
$r_{knuckle}$	67
r_{sphere}	307
L	256
t	5.25

A cylindrical vessel attached to a hemispherical end cap was modeled. The vessel consists of three regions: spherical, transition, and cylindrical. The transition region is the region between the spherical and cylindrical regions where transition stresses are observed. Variables used are a hemisphere outer radius $r_{spherical}$, wall thickness t, and a cylindrical region outer radius r_{outer}.

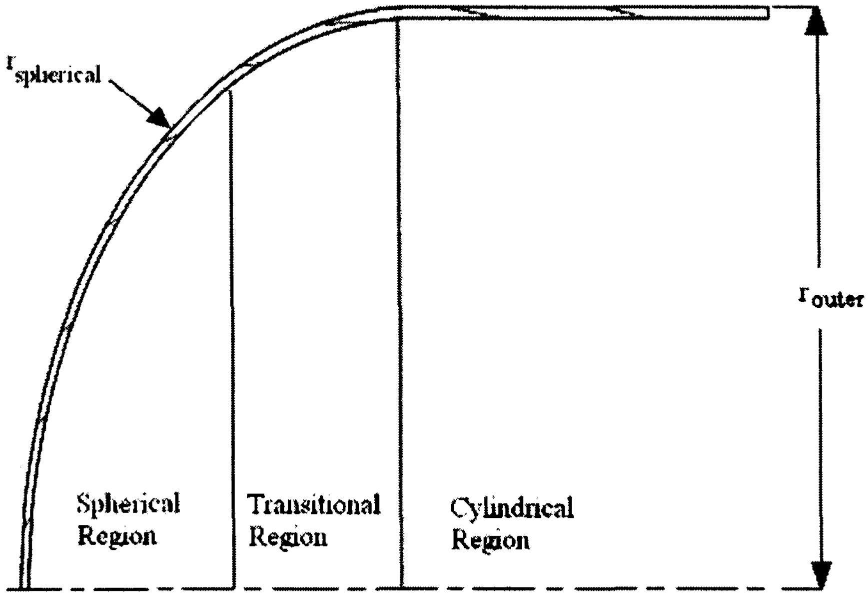

Figure 3.4: Cylinder with Hemispherical End Cap

Table 3.4: Variables defining Cylindrical Vessel attached to Hemispherical End Cap

Variable	Value [mm]
r_{outer}	253
$r_{spherical}$	253
t	5.25

The four vessel shapes were analyzed for several reasons. The torispheroidal dome shape maximizes the tank volume but has the highest vessel stresses. This shape is often used in vehicular applications where available vessel space is minimal. The hemispherical dome shape minimizes the tank volume but has the lowest vessel stresses. This shape is often used in applications where available vessel space is not a significant factor. The ellipsoidal dome shape is a compromise between the torispheroidal and hemispherical dome shapes. The cylinder with hemispherical end cap was analyzed to determine the stresses occurring at the interface between the spherical and cylindrical region.

3.2 FE Model Development

3.2.1 Element Selection

As mentioned in Section 3.0, the finite element models discussed here are all developed using the commercial finite element (FE) code, ANSYS. An axisymmetric shell element and an axisymmetric planar element were considered for the development of the pressure vessel models. These elements are discussed in the following sections.

3.2.1.1 Shell51 Element

Shell51 is a commonly used axisymmetric element suitable for modeling 2D axisymmetric structures. In its axisymmetric implementation, Shell51 has 2 nodes and each node has 3 degrees of freedom: 2 translational and one rotational. Shell51 can model membrane stress and inner and outer wall stress. This feature makes it possible to determine the bending and membrane stresses separately.

There are several disadvantages associated with using Shell51 elements. It is difficult to use these elements to model liners that have variable thicknesses because an individual thickness value would need to be defined for each element.

The spatial resolution that can be obtained with Shell51 is limited by its maximum allowable aspect ratio of 4. Aspect ratio is the ratio of element thickness to length. If the aspect ratio is too high, the elements behave like short cantilever beams which give poor nonlinear bending results.

Only one shell element is used in the thickness direction and hence, the smallest allowable element spacing is one fourth of the shell thickness. In regions of high stress gradients, this resolution is not adequate.

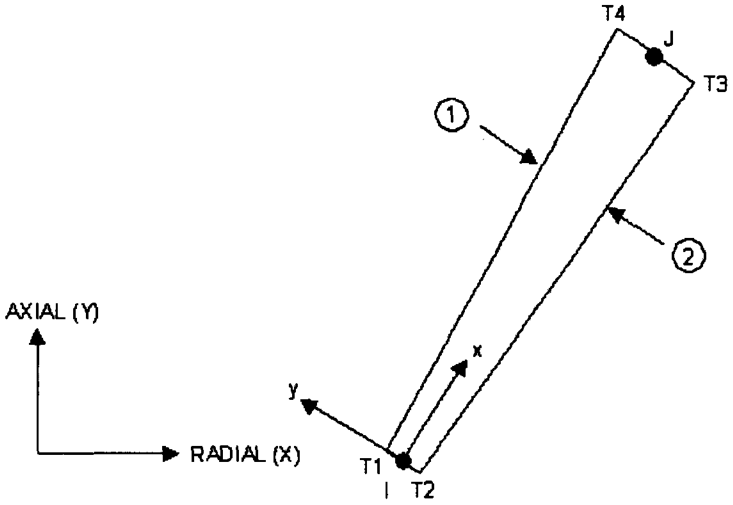

Figure 3.5: ANSYS Shell51 Element [25].

3.2.1.2 Plane42 Element

Plane42 is an element commonly used for modeling 2D axisymmetric structures. This element has 4 nodes and each node has 2 translational degrees of freedom, and no rotational degrees of freedom.

Plane42 can model linear stress variations so one element through the vessel wall thickness can model stress variation. However, to accurately capture stress variations due to bending in regions of non-uniform curvature such as the transitional region shown in Figure 3.4, multiple elements are required through the thickness of the vessel wall. Therefore, one disadvantage with using Plane42 is that its element meshes can be much more complicated than meshes created using Shell51.

Plane42 is capable of modeling liner stress and does not have any of the disadvantages associated with the Shell51 element. Therefore, it was the element that was used to create FE models in Chapter 3-5.

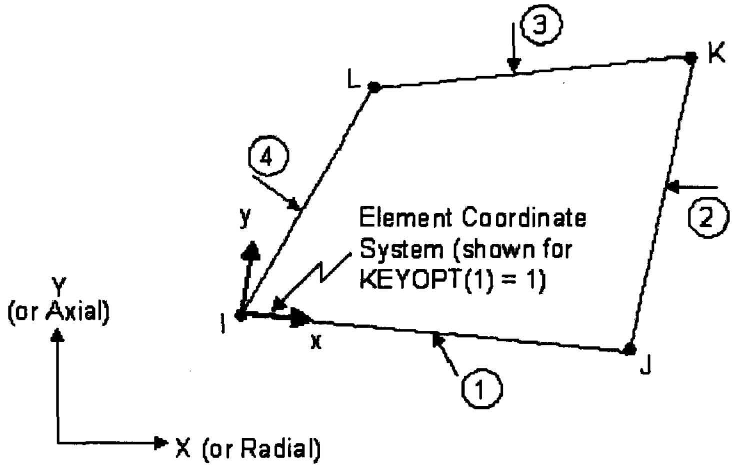

Figure 3.6: ANSYS Plane42 element [25].

3.3 Boundary Conditions and Modeled Stresses

The pressure vessel is defined to be axisymmetric with respect to its principal axis, as shown in Figure 3.7. A boundary condition constraining displacement in the axial direction u_{axial} ,was applied at the liner's cylindrical region to prevent rigid body motion. In the model, stresses are calculated in the thru orthogonal direction. Hoop stress σ_θ ,is a stress in the vessel's hoop direction. Meridonial stress σ_ϕ ,is the stress in the vessel's meridonial direction. Radial stress σ_{radial} ,is the stress normal to the vessel surface.

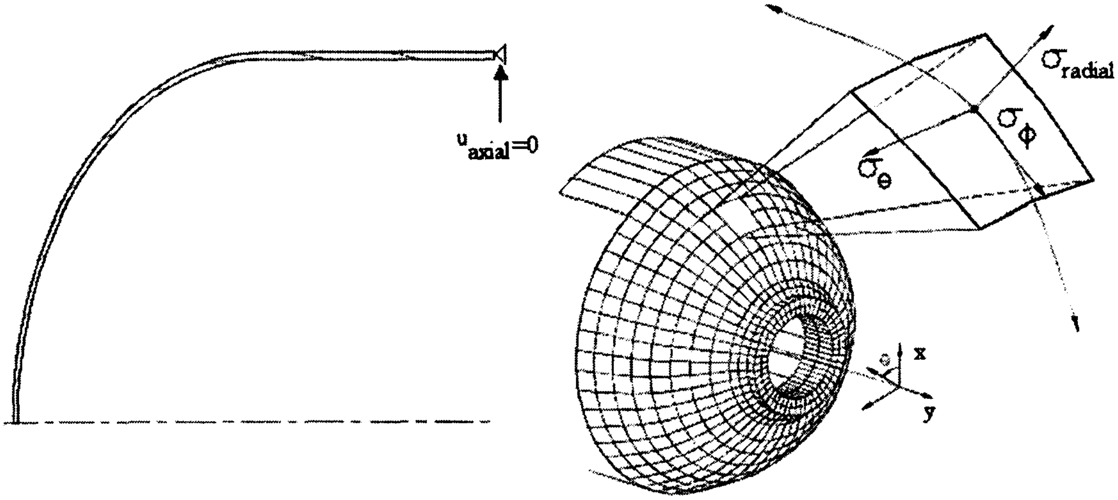

Figure 3.7: Liner model showing typical boundary conditions applied to FE models (left), and the stresses modeled by the FE model (right) [26].

3.4 Mesh Refinement

A mesh refinement study was performed on a vessel consisting of a cylinder with hemispherical end caps. The model was created using keypoints and meshed using Plane42 elements. The objective of mesh refinement is to determine the mesh density and keypoint density required to obtain accurate FE solutions.

Model results are compared to mathematically derived membrane theory results [27]. Membrane theory assumes that vessel is a thin shell that experiences no bending stresses.

3.4.1 Keypoint Refinement

The keypoint refinement study assessed the effect of the number of keypoints (KP) on convergence. Various models were created that contained a high number of elements and a variable number of keypoints. The aspect ratio (thickness/length) of elements used in each model is approximately 1. Table 3.5 summarizes the keypoint densities used for each model. Keypoint density is defined as the number of keypoints used per meter of liner surface.

Table 3.5: Characteristics of various meshes used for keypoint refinement study

Region	**Characteristic**	**Keypoint Density**		
		Low	**Medium**	**High**
Entire Vessel	Number of Elements	499	499	499
	Number of Nodes	738	738	804
	Number of Keypoints	95	200	312
Spherical	Keypoints	60	63	160
	Keypoint Density [KP/m]	187	197	500
Transitional	Keypoints	23	125	140
	Keypoint Density [KP/m]	100	543	609
Cylindrical	Keypoints	12	12	12
	Keypoint Density [KP/m]	80	80	80

Results of the study are summarized in Figures 3.8-3.10. In the figures, the inner surface stresses of the vessel were plotted as a function of path length where path length is the distance along the liner's inner or outer surface. Results were compared to closed form membrane theory solutions given in Section 3.6 [27].

Model stresses are slightly different than membrane theory stresses. The reason for the difference is the model measures the inner surface vessel stresses, and membrane theory calculates the neutral axis stresses. The inner surface has a smaller radius than the neutral axis and will therefore have lower stresses than the membrane theory model in the spherical and cylindrical region.

For the low density keypoint model, vessel stress has a series of spikes in the spherical and transitional region. The spikes likely occur because the FE model geometry is created within ANSYS by linking the keypoints using linear interpolation. It is believed that the resulting geometric discontinuities at the keypoints act as stress raisers which can cause a localized increase in the modeled stress. Each spike corresponds to a keypoint in the liner model. The low keypoint density model results in the cylindrical region are consistent with membrane theory results. Therefore, this model has a sufficient keypoint density in the cylindrical region.

The medium key point density model results in Figure 3.9 are similar to the high keypoint density model results in Figure 3.10. In addition, medium keypoint density model results are consistent with membrane theory results. These results indicate that the medium keypoint density model has a sufficient keypoint density. Therefore, it should not be necessary to use the large number of keypoints required in the high keypoint density model.

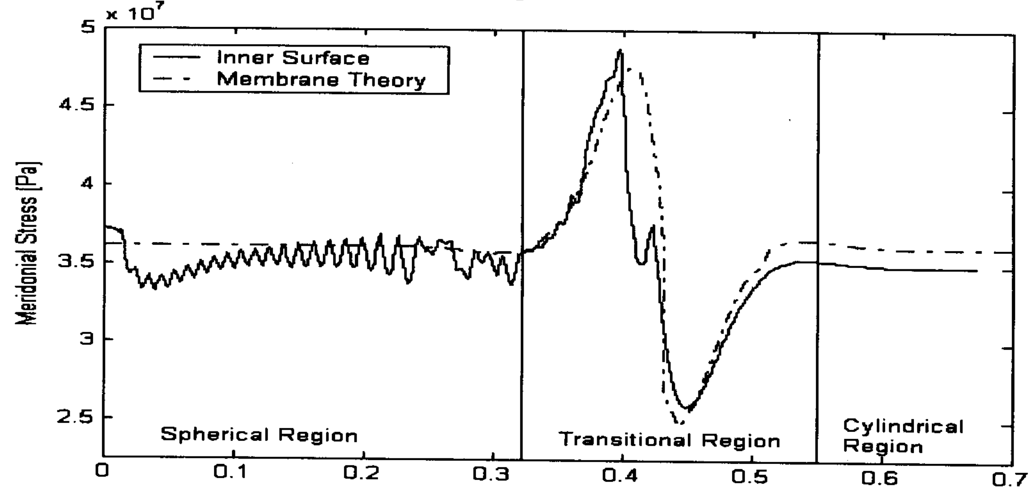

Figure 3.8: Meridonial Stress for small key point density model

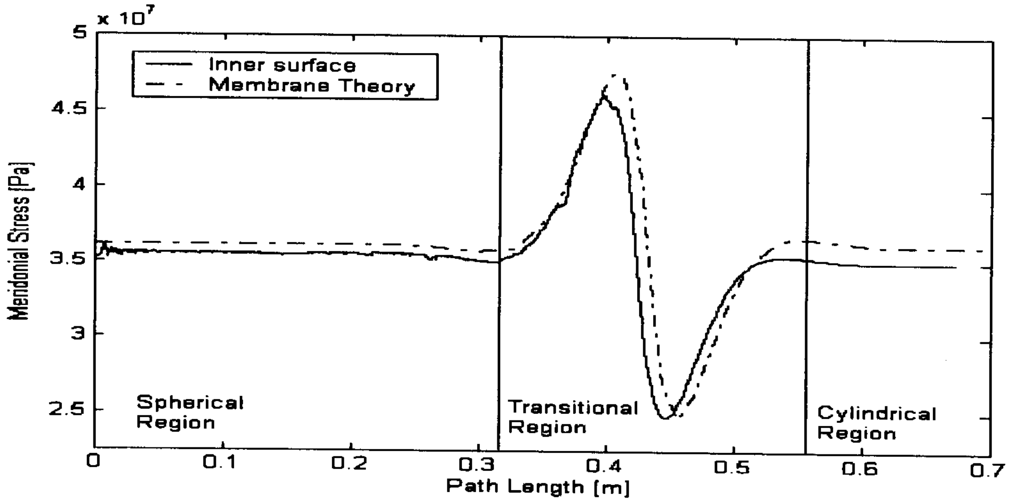

Figure 3.9: Meridonial Stress for medium key point density model

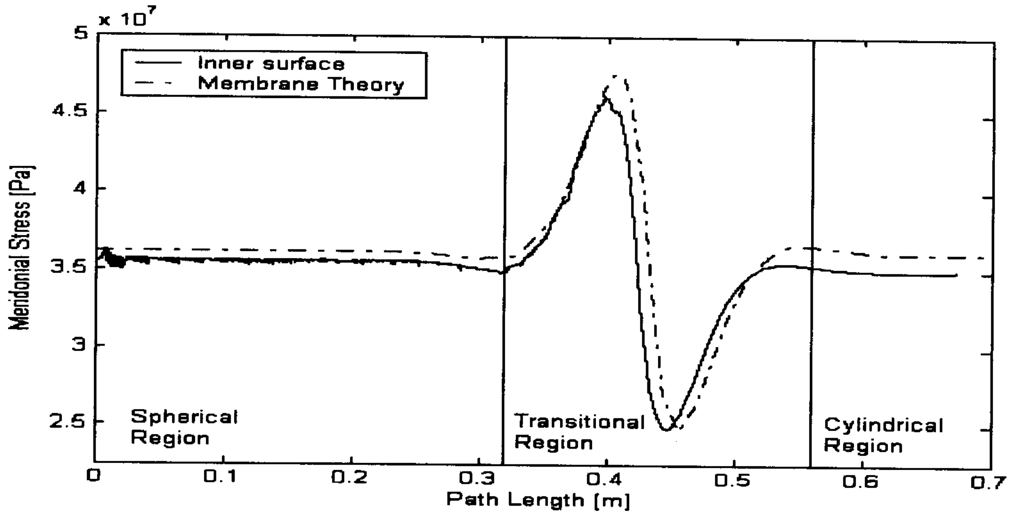

Figure 3.10: Meridonial Stress for high key point density model

3.4.2 Element Refinement

In the element refinement study the effect of varying the number of elements on convergence was assessed. Three models were created with a different number of Plane42 elements but the same 200 keypoints. Typical meshes obtained in the transition region are shown in Figure 3.11. Mesh density characteristics are summarized in Table 3.6. Results of the study are summarized in Figures 3.12-3.14.

Figures 3.12-3.14 show that convergence between the theoretical and FE results occurs as the number of elements increases. However, increasing the mesh density does not improve convergence with respect to membrane theory results as much as increasing the number of keypoints used to create the model.

The low mesh density model gives poor results in the spherical and transitional region of the vessel because of the high aspect ratio of the elements and lack of defined elements in these regions. The model's cylindrical region mesh density is high enough to give good results.

The medium and high mesh density models give results that are more consistent with membrane theory than the low mesh density model. These results show that increasing the mesh density causes the theoretical and mathematical results to converge. The high mesh density model has a higher mesh density than is required to model the vessel since its results are similar to the medium mesh density model.

As the mesh density increases from medium to high, the results in the spherical region become more irregular. These irregularities are caused by stress concentrations at keypoints, as discussed in Section 3.4.1. Increasing the keypoint density would result in a vessel shape with smaller stress concentrations at each keypoint. This would help reduce the magnitude of the irregularities.

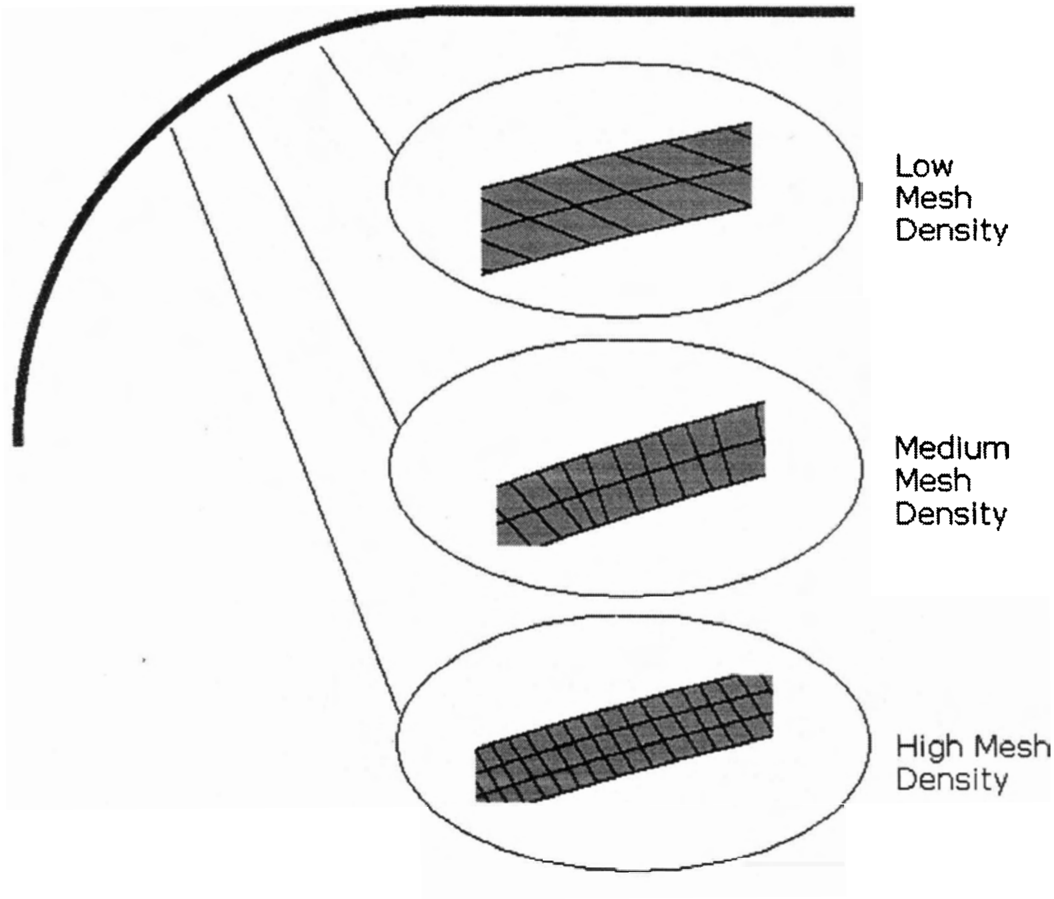

Figure 3.11: Mesh density in the transition region of vessels analyzed in element refinement study

Table 3.6: Characteristics of various meshes used for element refinement study

Region	**Characteristic**	**Mesh Density**		
		Low	**Medium**	**High**
Entire Vessel	Number of Elements	364	499	1149
	Number of Nodes	549	738	1536
	Number of Keypoints	200	200	200
	Number of Elements Through Thickness	2	2	3
Spherical	Aspect Ratio	1	1	1
Transitional	Aspect Ratio	2	1-2	1
Cylindrical	Aspect Ratio	1	1	1

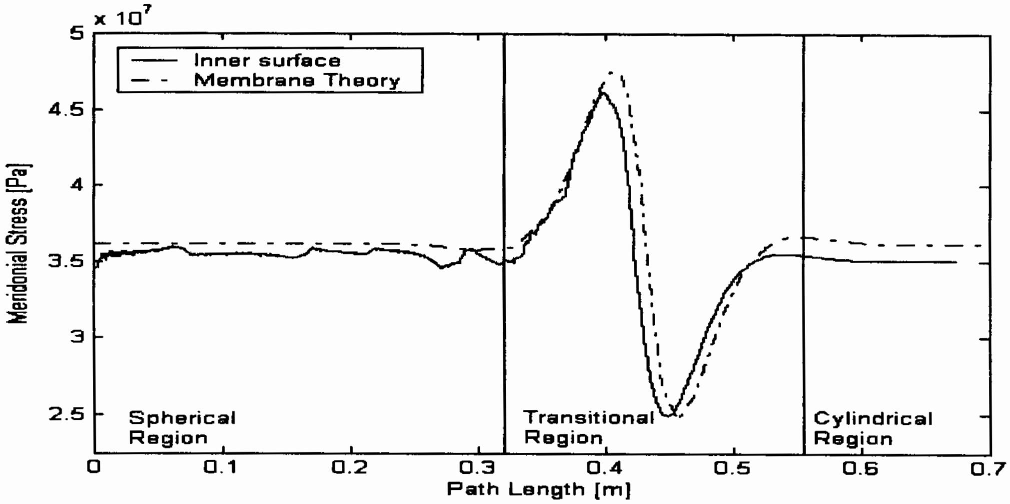

Figure 3.12: Meridonial Stress for low mesh density model

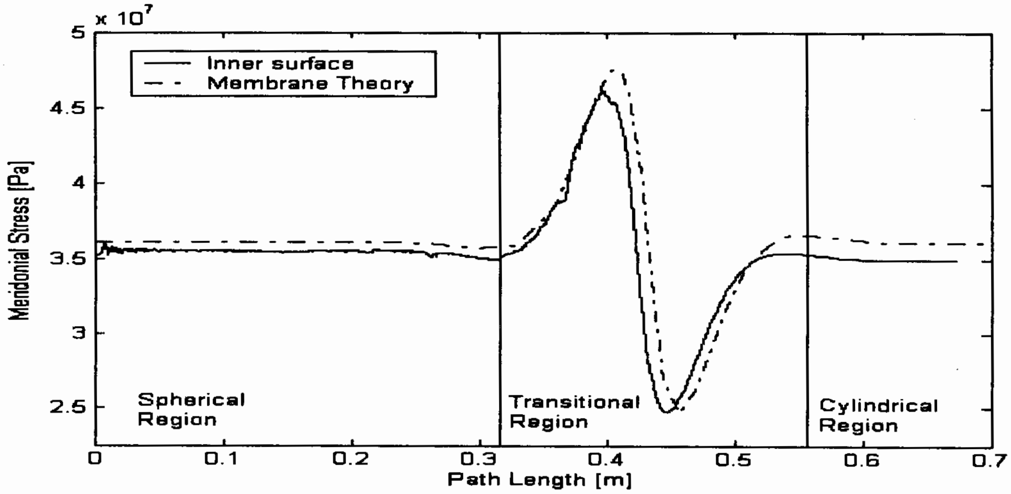

Figure 3.13: Meridonial Stress for medium mesh density model

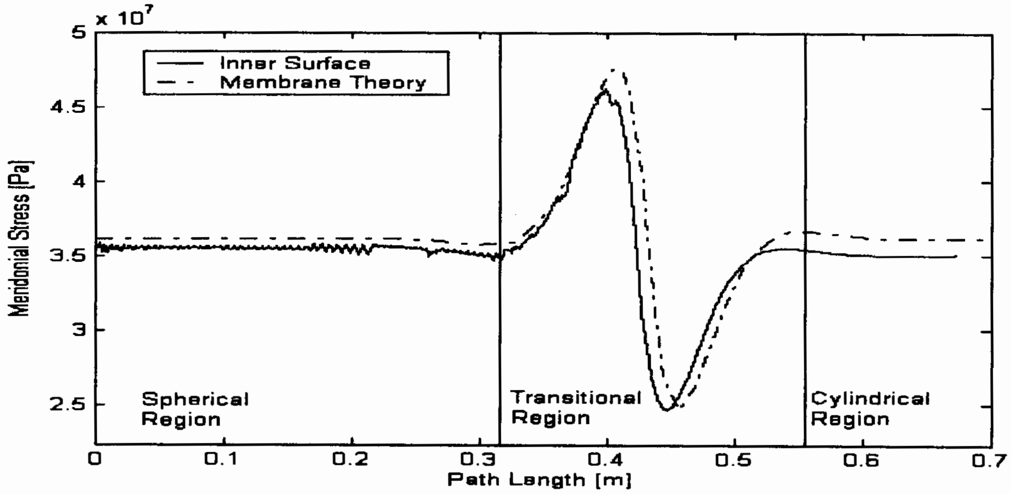

Figure 3.14: Meridonial Stress for high mesh density model

3.5 Model Validation

FE models of simple pressure vessel designs were compared to closed-form solutions based on membrane theory solutions. The models are developed based on the results of the keypoint and mesh refinement studies.

3.5.1 Hemispherical Dome

The FE model was meshed used 109 Plane42 elements with an aspect ratio of 1, and has 2 elements through the thickness of the dome.

Equation 3.1 provides an expression for hoop and meridonial stress for a thin-walled hemispherical dome vessel. The hemispherical dome model stresses can be investigated using the thin-walled vessel equation since the vessel has a radius that is at least 5 times the wall thickness [27]. In this equation, P is the internal vessel pressure 1.38 MPa (200 psi), r_{in} is the inner radius of the hemisphere (275 mm), and t is the wall thickness of the hemisphere (5.25 mm) [24]. Hoop and meridonial stresses are the same throughout the dome due to the uniform curvature of the spherical dome.

$$\sigma_\theta = \sigma_\phi = \frac{P \cdot r_{in}}{2t} \tag{3.2}$$

FE stress results for a hemispherical dome in Figure 3.1 are summarized in Table 3.7. Closed-form results are within 0.2% of the FE model results.

Table 3.7 Summary of Stresses for Hemispherical Dome Model

	Mathematical Model	**FE Model**
Hoop Stress [MPa]	88.6	88.8
Meridonial Stress [MPa]	88.6	88.8

3.5.2 Ellipsoidal Dome

A FE model of the ellipsoidal dome in Figure 3.2 was created using Plane 42 elements for the mesh. FE mesh characteristics are summarized in Table 3.8.

Table 3.8: FE mesh characteristics for Ellipsoidal Dome Model

Number of Elements	**Aspect Ratio**	**Number of Nodes**	**Number of Keypoints**	**Keypoint Density [KP/m]**	**Number of Through Thickness Elements**
251	1	378	80	258	2

Meridonial stress σ_ϕ, derived using membrane theory, is defined in Equation 3.3 with a non-dimensional variable u defined in Equation 3.4, and the ellipsoidal dome's eccentricity e is defined in Equation 3.5 [28].

$$\sigma_\phi = \frac{P \cdot (r_{major})^2 \cdot u}{2t \cdot r_{\min or}} \tag{3.3}$$

$$u = \sqrt{1 - e^2 \cdot \left(\frac{r_{axial}}{r_{major}} \right)^2} \tag{3.4}$$

$$e = \sqrt{1 - \left(\frac{r_{\min or}}{r_{major}} \right)^2} \tag{3.5}$$

Hoop stress σ_θ ,is defined in Equation 3.6 using variables obtained in Equations 3.3-3.5. Equation 3.6, was derived using the membrane theory assumption that no bending occurs in the ellipsoidal dome [28].

$$\sigma_\theta = \sigma_\phi (2 - \frac{1}{u^2}) \tag{3.6}$$

Meridonial stress for the ellipsoidal dome is shown in Figure 3.15. Bending stress is the cause of the deviation in stress from the theoretical membrane stress. At locations near the axis of symmetry, the dome bends outwards causing the outer dome surface to experience tension and the inner dome surface to experience compression. At locations away from the axis of symmetry, the dome bends inwards causing the outer dome surface to experience compression and the inner dome surface to experience tension. This effect can be seen in Figure 3.16 as a divergence of the inner and outer surface stresses.

Hoop stress for the ellipsoidal dome is shown in Figure 3.16.The membrane theory hoop stress given in Equation 3.6 closely agrees with the FE derived hoop stress data.

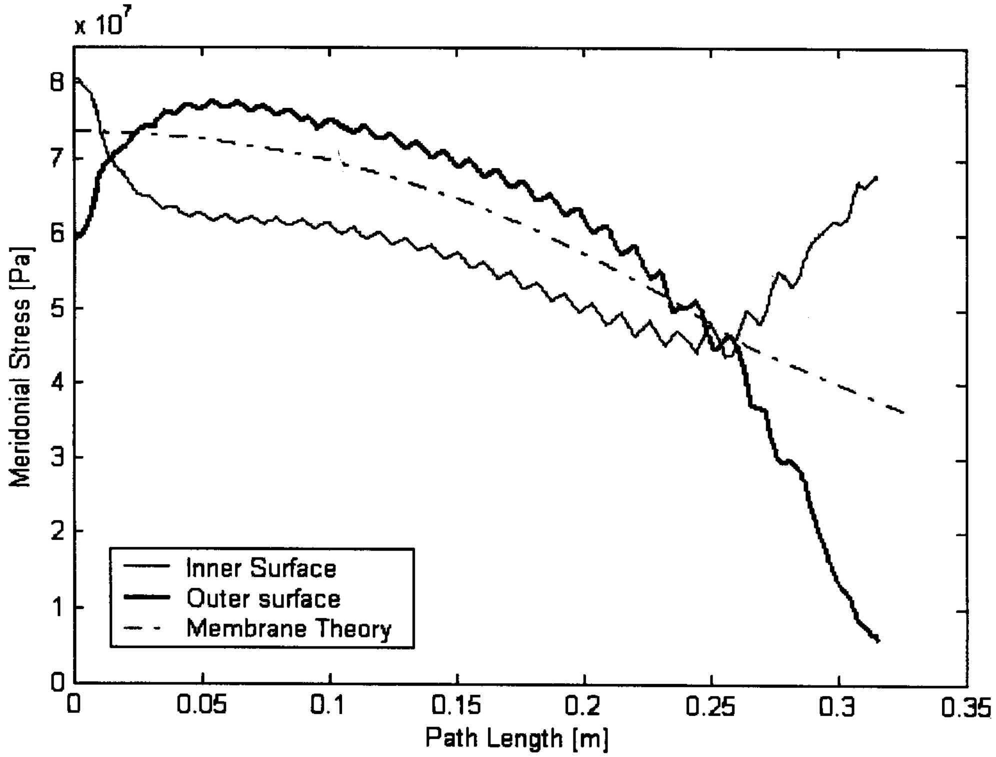

Figure 3.15: Meridonial Stress for the Ellipsoidal Dome

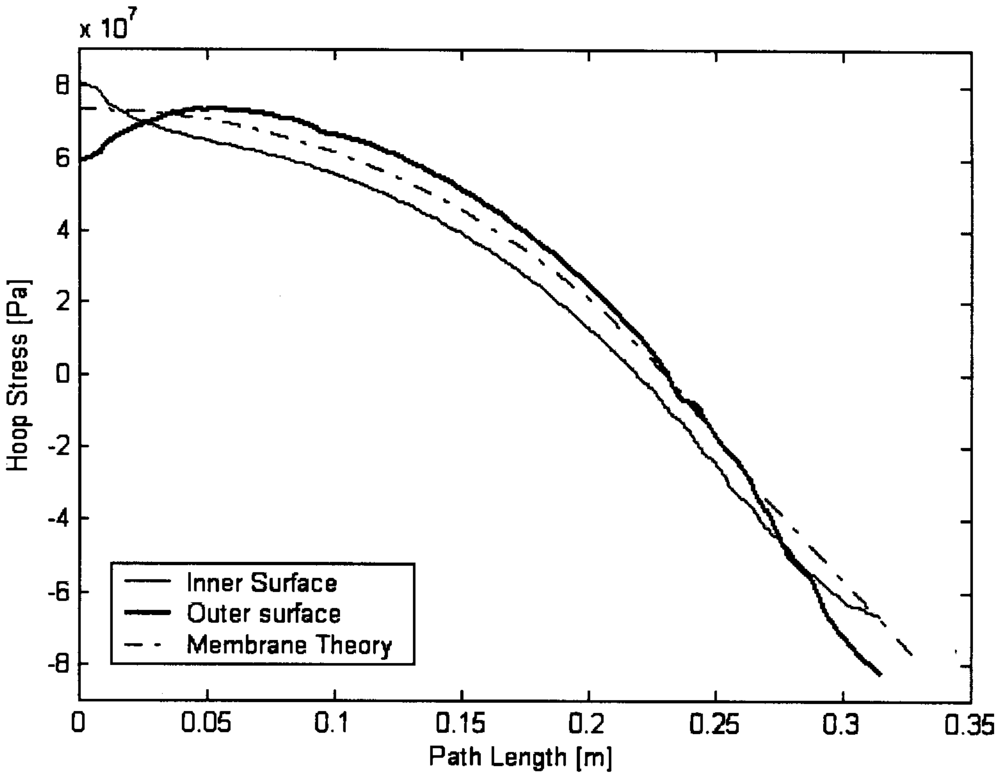

Figure 3.16: Hoop Stress for the Ellipsoidal Dome

3.5.3 Torispheroidal Dome

A FE model of a torispheroidal dome shown in Figure 3.3 was created using Plane42 elements for the mesh. FE mesh characteristics are summarized in Table 3.9.

Table 3.9: FE mesh characteristics for Torispheroidal Dome Model

Number of Elements	**Aspect Ratio**	**Number of Nodes**	**Number of Keypoints**	**Keypoint Density [KP/m]**	**Number of Through Thickness Elements**
687	1	1836	230	742	2

A literature search found no closed form solutions for the theoretical stresses of a torispheroidal shell. However, Equations 3.7-3.9 determine the hoop and meridonial stresses at key positions along the torispheroidal shell [27].

Equation 3.7 gives the hoop and meridonial stress in the torispheroidal dome's spherical region where P is the internal pressure, $r_{spherical}$ is the radius of the spherical cap region, and t is the dome's wall thickness.

$$\sigma_\theta = \sigma_\phi = \frac{P \cdot r_{spherical}}{2t} \tag{3.7}$$

Equation 3.8 gives the theoretical meridonial membrane stress at the base of the torispheroidal dome's knuckle region (section line C) where r_{axial} is the axial radius of the torispheroidal shell's knuckle region.

$$\sigma_\phi = \frac{P \cdot r_{axial}}{2t} \tag{3.8}$$

Equation 3.9 gives the hoop stress at the boundary between the torispheroidal dome spherical and knuckle region (section line B) where $r_{knuckle}$ is the knuckle region radius.

$$\sigma_\theta = \frac{P \cdot r_{spherical}(3r_{knuckle} - r_{spherical})}{4 \cdot t \cdot r_{knuckle}} \tag{3.9}$$

The hoop and meridonial stress in the spherical region was calculated to be 41 MPa using Equation 3.7. The calculated value is close to the FE derived stress of 40 MPa shown in Figures 3.17 and 3.18.

Figure 3.18 shows that significant bending occurs in the spherical knuckle region of the dome that is not accounted for in theoretical equations such as Equation 3.8. Bending causes the dome to deform inwards causing the outer dome surface to experience compression and the inner dome surface to experience tension. The average of the inner and outer FE model meridonial stresses in the spherical knuckle region is 36 MPa which is close to the theoretical membrane stress of 33.2 MPa given in Equation 3.8. In the portion of the spherical region near the knuckle region, the liner bends outwards causing tension in the outer dome surface and compression in the inner dome surface.

The hoop stress at the boundary between the spherical region and knuckle region (section line B) was calculated to be -28.7 MPa using Equation 3.9. The calculated value is approximately equal to the FE hoop stress values shown in Figure 3.17.

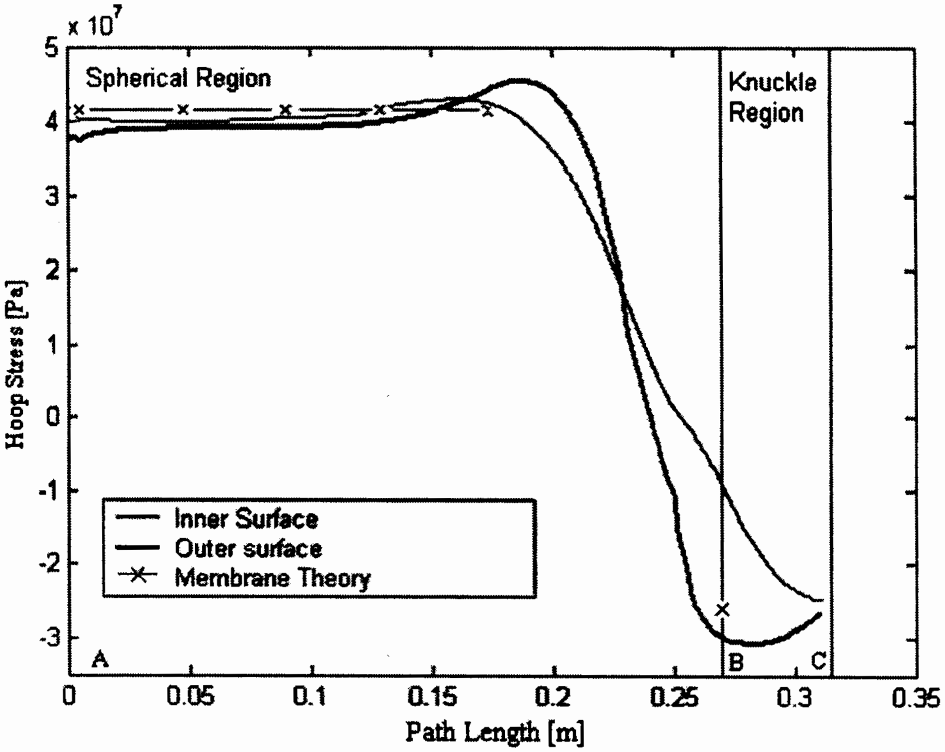

Figure 3.17: Hoop Stress for the Torispheroidal Dome

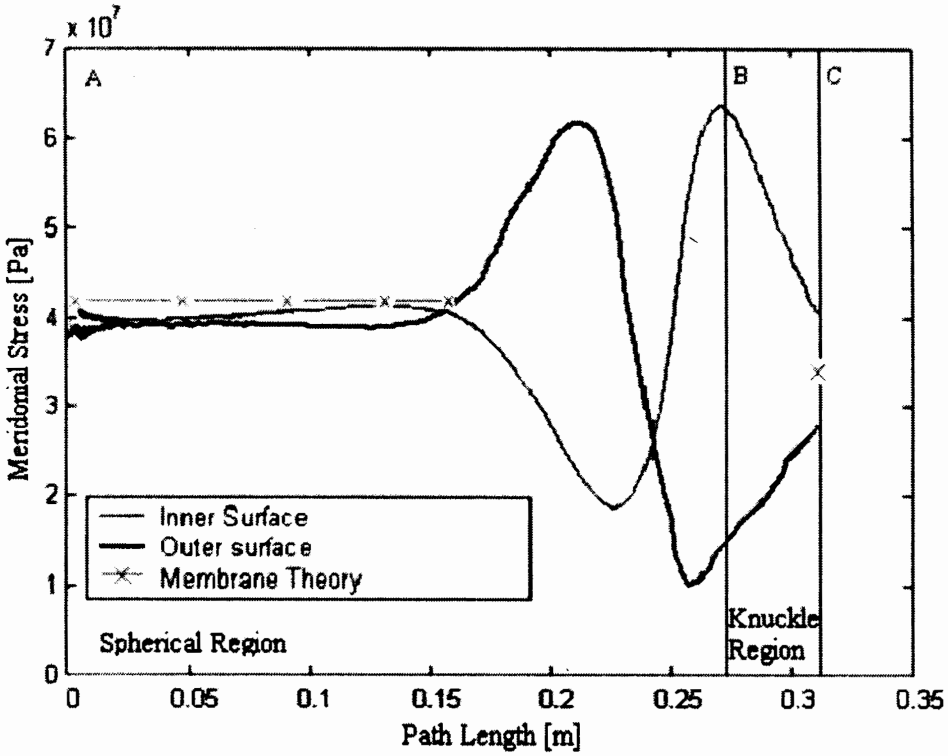

Figure 3.18: Meridonial Stress for the Torispheroidal Dome

3.6 Cylinder with Hemispherical End Cap

A FE model of the cylinder with a hemispherical end cap shown in Figure 3.4 was created. The FE model used was the medium mesh density model described in the mesh refinement section, with specifications provided in Table 3.10.

Table 3.10: Variables defining Cylindrical Vessel attached to Hemispherical End Cap

Variable	Value [mm]
r_{outer}	253
$r_{spherical}$	253
t	5.25

Equation 3.10 gives an expression for the theoretical hoop stress in the vessel's transition region [28]. In this equation, P is the internal vessel pressure, x is the position along the liner transition region, r_{in} is the inner radius of the spherical region, and k and λ are independent variables defined in Equations 3.11 and 3.12.

$$\sigma_\theta = \frac{P \cdot r_{in} \cdot (1 - 0.25 \cdot e^{-\lambda \cdot x / r_{in}} \cdot \cos(\lambda x / r_{in}))}{t} \tag{3.10}$$

$$k = \frac{E \cdot t^3}{12 \cdot (1 - \nu^2)} \tag{3.11}$$

$$\lambda = \left(\frac{E \cdot t \cdot r_{in}^{\ 2}}{4 \cdot k} \right)^{0.25} \tag{3.12}$$

Equation 3.13 gives an expression for the meridonial membrane stress.

$$\sigma_\phi = \frac{P \cdot (r_{in})}{2t} \tag{3.13}$$

Equation 3.14 gives the meridonial bending stress in the transition region [28]. In this equation, M_ϕ is the bending moment defined in Equation 3.15. This stress is tensile on the outer surface and compressive on the inner surface of the liner.

$$\sigma_{\phi} = \frac{\pm 6M_{\phi}}{t^2} \tag{3.14}$$

$$M_{\phi} = \frac{(Pa^2)(e^{-\lambda\theta})(\sin(\lambda\theta))}{8\lambda^2} \tag{3.15}$$

Hoop Stress data in Figure 3.19 shows that theoretical hoop stress results are similar to FE results.

The meridonial membrane stress was calculated to be 36.2 MPa using Equation 3.13. Calculated results are similar to FE results in the cylindrical and spherical regions of Figures 3.20-3.21.

Meridonial stress in the transition region is the sum of the membrane stress and bending stress calculated in Equations 3.13 and 3.15. The theoretical meridonial stress results agree closely with FE results shown in Figures 3.20-3.21.

The hoop and meridonial stresses are not constant in the transitional region between the cylinder and sphere because internal pressure causes the cylindrical region to deform more than the spherical dome region. As a result, compressive stress occurs in the cylindrical region and tensile stress occurs in the spherical dome region.

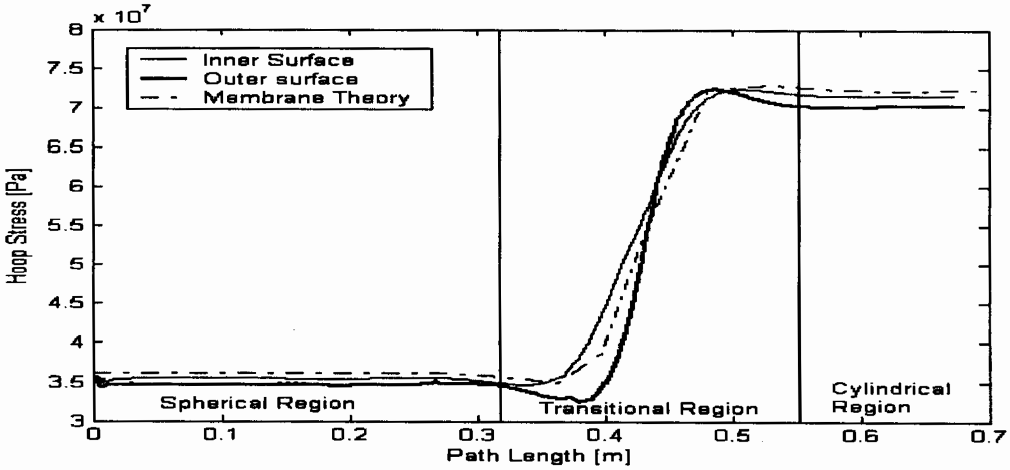

Figure 3.19: Hoop Stress for the Cylinder with Hemispherical End Cap

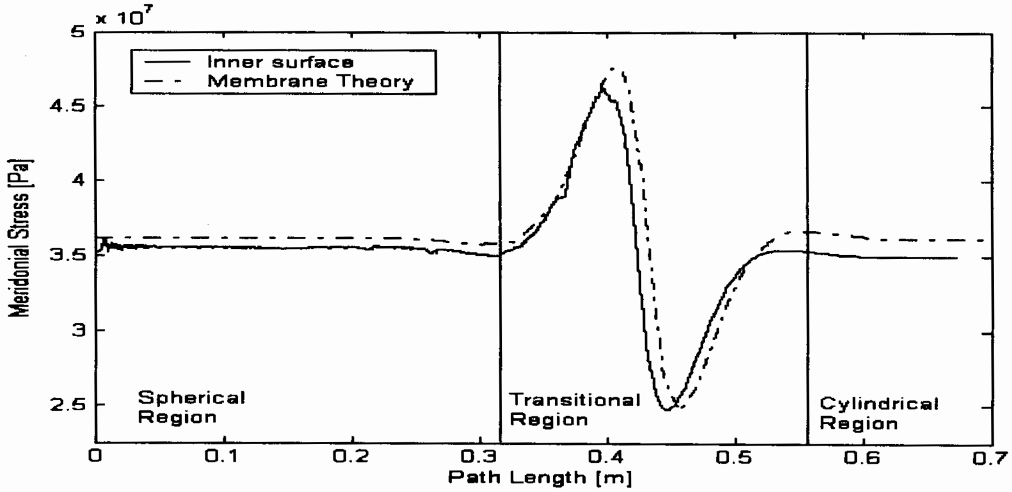

Figure 3.20: Meridonial Stress for the inner surface of the Cylinder with Hemispherical End Cap

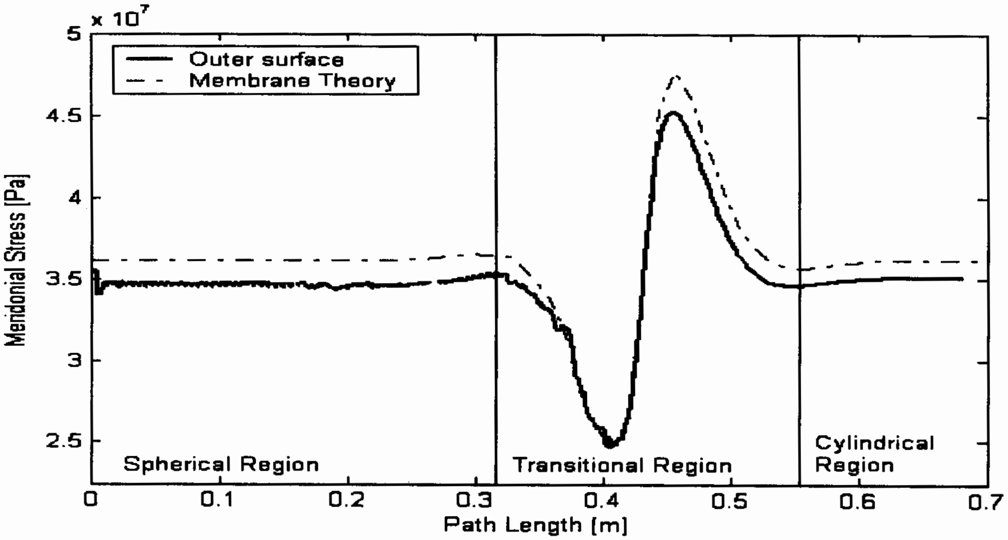

Figure 3.21: Meridonial Stress for the outer surface of the Cylinder with Hemispherical End Cap

3.7 Summary

The models developed in this report were meshed using Plane42 elements. The Plane42 element is used for FE models since it is easier to create models for vessels with variable thickness and measure stresses in regions of high stress gradients using Plane42 than with Shell51.

The mesh refinement study determined the mesh and keypoint densities required to obtain reliable results in various regions of a vessel consisting of a hemispherical dome with a cylinder. The methods used for the mesh refinement study will be applied to more complicated liner shapes in Chapter 4-5.

The FE models that were created agreed closely with closed-form equations. These results helped validate the FE modeling procedure that will be used in Chapter 4 to model vessels such as the Dynetek ZD154 liner that contains no closed-form solutions.

Chapter 4

Analysis of Dynetek Liners

4.0 Introduction

In this chapter, the FE method that was developed and validated in Chapter 3 is used to analyze two Dynetek Canada liners. The Dynetek ZD154 liner was analyzed because its length and diameter are similar to current fuel tank designs for transport trucks [10,29]. The Dynetek W320 liner is one of the few liners that Dynetek has burst test [29]. Therefore, an FE model for the W320 liner can be validated by comparing vessel stresses to Dynetek burst test results [29].

4.1 FE Model Description

FE analysis of the Dynetek ZD154 and W320 liners were performed to determine vessel liner stresses such as the hoop, meridonial, and Von Mises stresses. Hoop and meridonial stress is discussed in Section 3.3. Von Mises stress is a measure of the total vessel stress. Appendix A2.3 gives an expression for the Von Mises stress. The FE model geometries were created in ANSYS using a series of keypoints whose values were obtained using Dynetek Canada drawings [10,29].

Dynetek liners were modeled using the material properties of aluminum 6061-T6 which is the material used by Dynetek for their pressure vessel liners. The modulus of elasticity E of the aluminum was 70 GPa and the Poisson's ratio ν was 0.3.

A pressure P of 1.38 MPa (200 psi) was applied to each modeled liner. This pressure is the proposed maximum allowable working pressure (MAWP) for the Dynetek liners that will be used for fuel storage. Hydrostatic pressure caused by the weight of the fuel was neglected since it is less than 0.021 MPa (3 psi) as calculated in Appendix A2.1.

4.2 Dynetek W320 Liner

The FE analysis method will be validated by comparing the predicted burst pressure to burst test results for a Dynetek W320 liner. A section view of the Dynetek W320 liner with the applied boundary conditions is shown in Figure 4.1. Table 4.1 outlines the different regions of the W320 liner.

4.2.1 FE Model for Dynetek W320 Liner

The boundary conditions that are applied to a Dynetek W320 liner are shown in Figure 4.1. Only the dome region and a portion of the cylindrical region were modeled due to the symmetry of the W320 liner shape. The boundary condition constraining displacement in the axial direction was applied at the end of the modeled liner's cylindrical region.

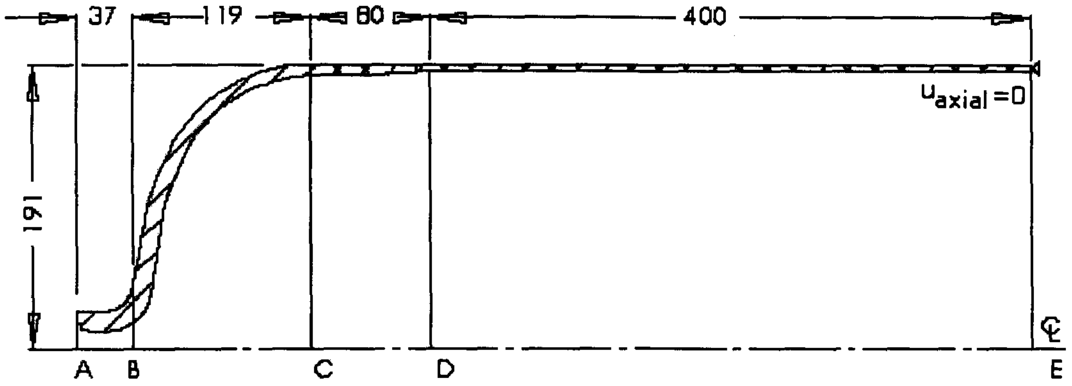

Figure 4.1: Section of a Dynetek W320 liner [29]. Units in mm.

Table 4.1: Summary of Sections in the W320 Liner

Section	Description	Wall Thickness [mm]
A-B	Port Boss	14.0 -13.0
B-C	Dome	13.0 - 7.3
C-D	Transition	7.3 - 4.25
D-E	Cylindrical	4.25 - 4.25

4.2.2 FE Model Results

Table 4.2 provides a summary of the FE mesh characteristics of the W320 liner. The FE mesh was created using Plane42 elements. The keypoint densities used are comparable to those used in the medium mesh density model discussed in the previous chapter's keypoint refinement study. The number of through thickness elements ranges from 2 to 4, and are higher in regions such as the dome which require a finer mesh.

Table 4.2: FE Mesh Characteristics of the W320 Liner model

	Dome	**Dome Taper**	**Cylindrical**
Keypoint Density [KP/m]	138	467	122
Through Thickness Elements	4	4	2

FE results showing the Von Mises, Hoop, and Meridonial Stress are summarized in Figures 4.2-4.4. The liner's inner surface has a path length that is slightly longer than the outer surface. Therefore, the inner liner surface stress data is slightly offset from the outer surface stress data. In the dome region (section line B-C), the meridonial stress results are irregular. This behavior is caused because the dome region shape used in the FE model does not perfectly represent the actual dome region shape. The results could be less irregular by increasing the number of keypoints. This was not done since the objective is not to determine localized stress behavior but rather to determine regions of the liner where stresses are highest.

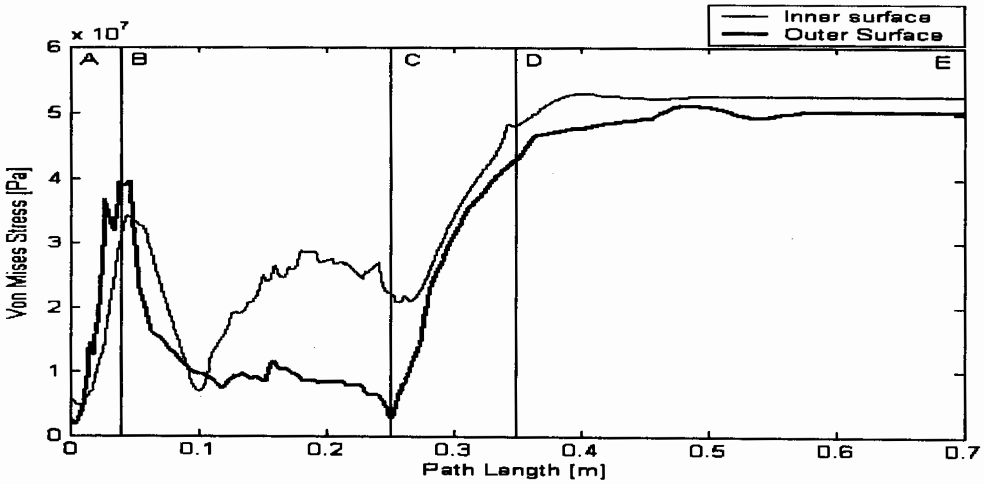

Figure 4.2: Von Mises Stress for the Dynetek W320 liner

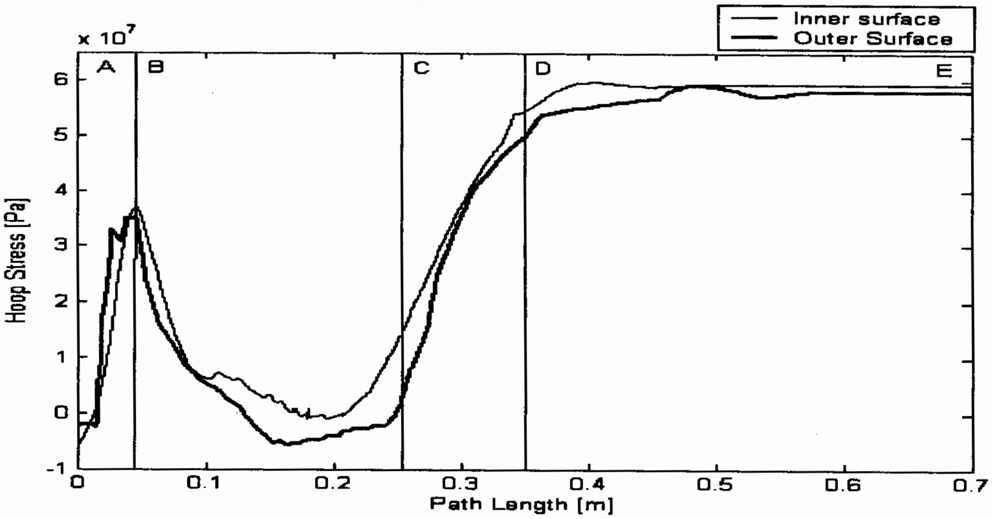

Figure 4.3: Hoop Stress for the Dynetek W320 liner

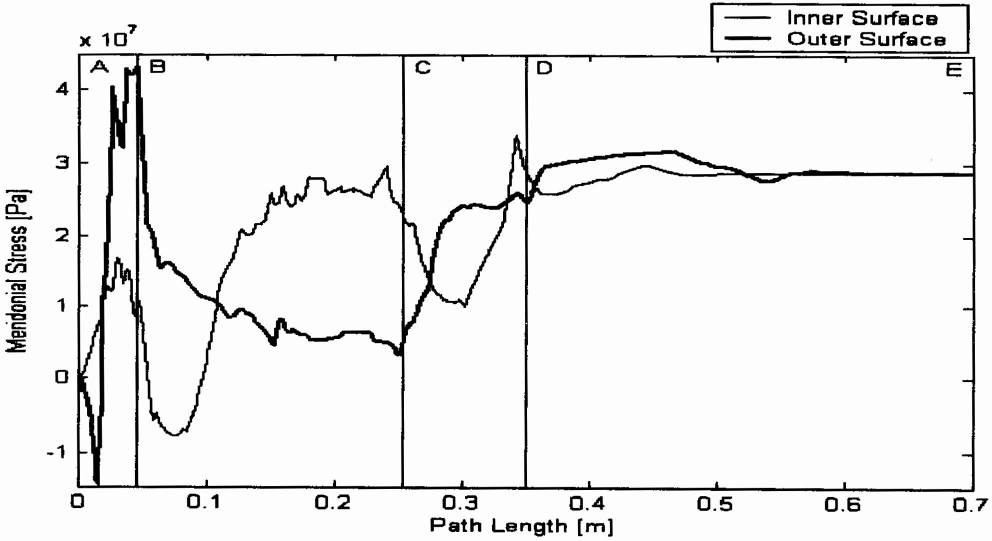

Figure 4.4: Meridonial Stress for the Dynetek W320 liner

Von Mises stresses throughout the W320 liner vessel are shown in Figure 4.2. Table 4.3 shows the maximum FE stresses in the regions with the highest observed stresses. In addition, failure pressure and factor of safety based on yield, and ultimate failure are calculated using a yield stress of 290 MPa, and ultimate tensile stress (UTS) of 320 MPa.

Table 4.3: Highest Calculated Stresses Observed in Key Regions of the W320 Liner

			Failure based on Yield Stress		**Failure based on UTS**	
Region	**Applied Pressure**	**Max Stress**	**Failure Pressure**	**FS**	**Failure Pressure**	**FS**
Dome	1.38 MPa (200 psi)	40 MPa	10.01 MPa	7.25	11.04 MPa	8
Cylinder	1.38 MPa (200 psi)	53 MPa	7.55 MPa	5.47	8.34 MPa	6.04

Dynetek performed a burst test on a W320 liner that involved increasing the liner pressure until vessel burst occurred [29]. The vessel burst in the liner's cylindrical wall region when the vessel pressure reached 11.9 MPa (1726 psi). The measured burst test pressure is higher than the FE model predicted burst pressure of 8.34 MPa (1208 psi) shown in Table 4.3.

There are several possible reasons for the discrepancy between theoretical and burst test results. Dynetek has found that W320 liners have typical yield stresses of 330 MPa that have been measured in tensile tests. The measured yield stresses are higher than the yield stress of 290 MPa, and the UTS of 320 MPa required by design specifications. In addition, Dynetek's current manufacturing process strengthens the manufactured liner using work hardening. However, the liners are subsequently heat treated so the effect of work hardening should be removed. Another reason for the discrepancy could be that only one liner was burst test. Therefore it is possible that the burst liner had a higher than average burst pressure.

FE results, shown in Figure 4.2 are consistent with Dynetek burst test results which indicated that liners initially fail in the cylindrical wall region. The hoop and meridonial stress results for the W320 liner are shown in Figures 4.3 and 4.4. These results have a similar qualitative behavior to the ZD154 liner results in Section 4.2. Therefore, they will not be discussed in this section.

4.3 Dynetek ZD154 liner

4.3.1 FE model for ZD154 liner

Figure 4.5 shows a cross-sectional view of the Dynetek ZD154 liner with the required boundary conditions. Table 4.4 outlines the different regions of the Dynetek ZD154 liner and the wall thickness range at each region. Rigid body motion was prevented by constraining axial motion at the liner's closed end. No other boundary conditions were needed because the model is axisymmetric.

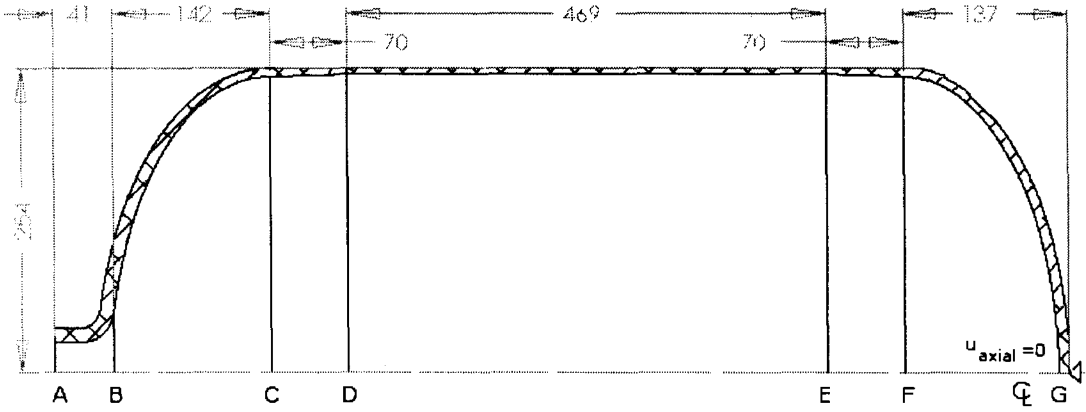

Figure 4.5: Section view of a Dynetek ZD154 liner [28]. Units in mm.

Table 4.4: Summary of ZD154 liner sections and wall thicknesses

Section	Description	Wall Thickness [mm]
A-B	Port Boss	15.8-13.2
B-C	Dome	13.2-9.2
C-D	Port Boss End Transition	9.2-5.25
D-E	Cylindrical	5.25-5.25
E-F	Closed End Transition	5.25-10.1
F-G	Closed End	10.1-11.2

4.3.2 FE Model Results

Table 4.5 provides a summary of the FE mesh characteristics of the ZD154 liner. The FE mesh was created using Plane42 elements. The keypoint densities used are comparable to those used in the medium mesh model discussed in Section 3.4.1. The number of through thickness elements varies from 2 to 4, and is higher in regions that require a finer mesh such as the dome.

Table 4.5: FE Mesh Characteristics for various regions of the ZD 154 Liner

	Dome	**Dome Taper**	**Cylindrical**	**Base Taper**	**Base**
Keypoint Density [KP/m]	160	160	97	160	109
Through Thickness Elements	4	3	2	3	4

FE results showing the Von Mises, Hoop, and Meridonial Stress are summarized in Figures 4.6-4.8. The liner's inner surface has a path length that is slightly longer than the outer surface. Therefore, the inner liner surface stress data is slightly offset from the outer surface stress data.

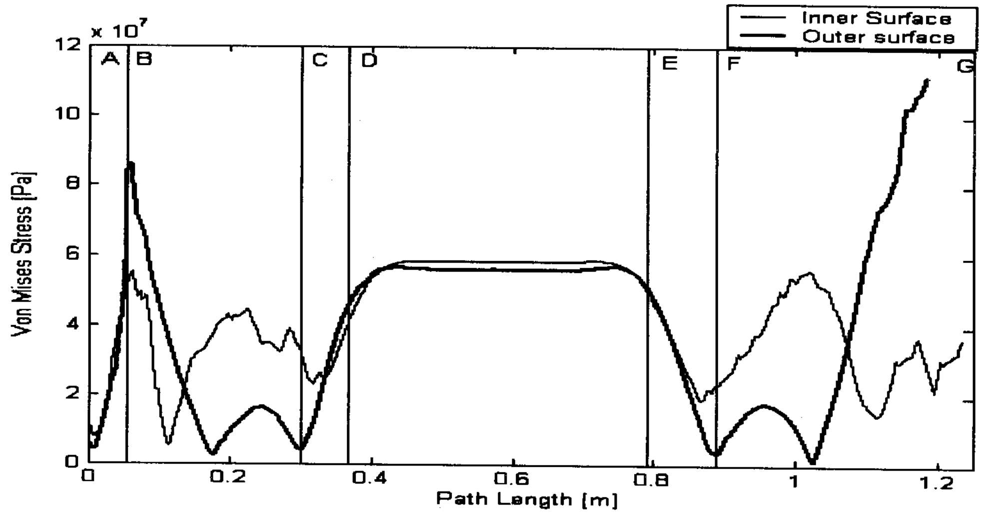

Figure 4.6: Von Mises Stress for the Dynetek ZD154 liner

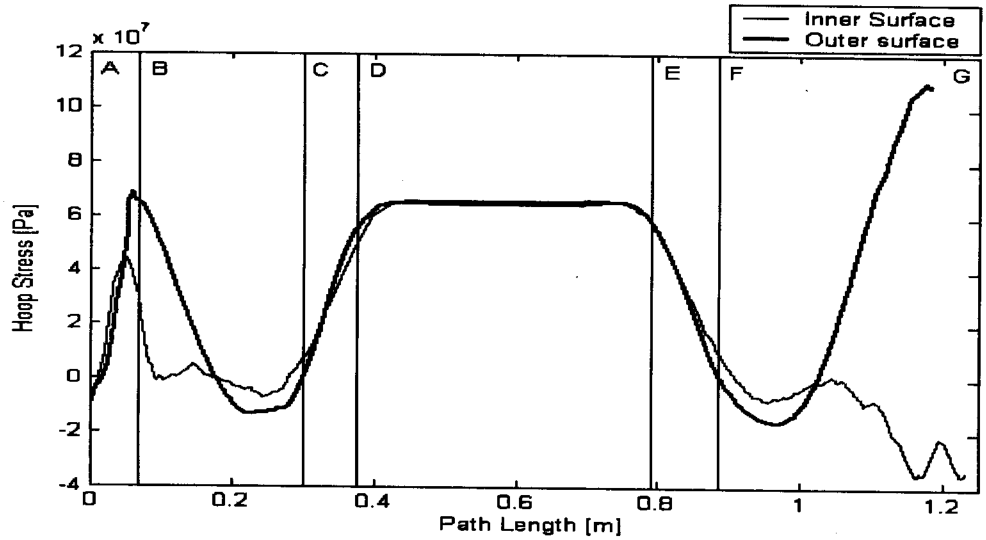

Figure 4.7: Hoop Stress for the Dynetek ZD154 liner

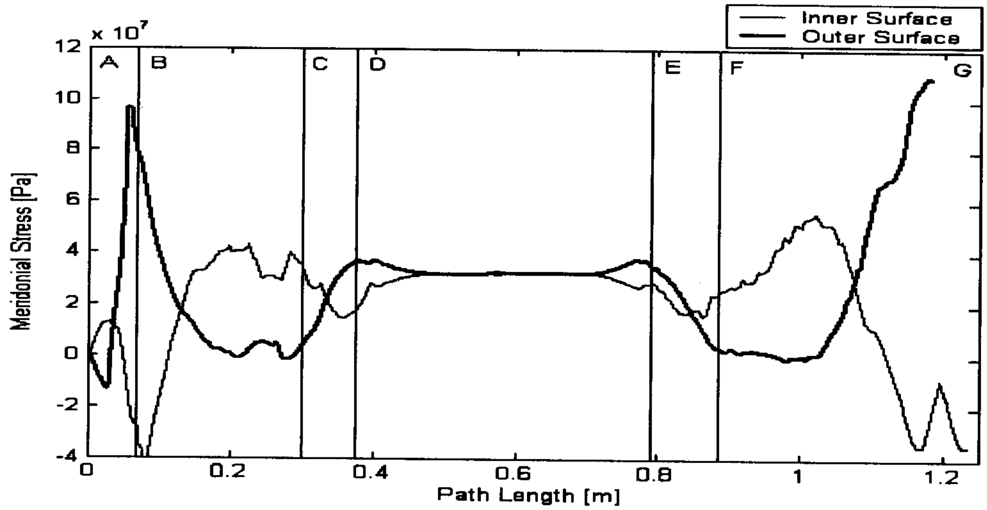

Figure 4.8: Meridonial Stress for the Dynetek ZD154 liner

Von Mises stresses throughout the ZD liner vessel are shown in Figure 4.6. Table 4.6 shows the FE stresses in regions with the highest observed stresses. The factor of safety is calculated using a liner yield stress of 290 MPa. All of the liner's regions satisfy the factor of safety of 2.35 required by cylinder standards [29,30].Results indicate the ZD154 liner will not initially fail in the cylindrical region which was the failure location of the W320 liner when it was burst test. There is currently no burst test data for ZD154 liners.

Table 4.6: Highest Stresses Observed in Key Regions of the ZD154 Liner

Region	Max Stress [MPa]	Factor of Safety
Dome	84	3.45
Cylindrical	56	5.18
Closed End	112	2.59

Hoop stress throughout the ZD154 liner is shown in Figure 4.7. In the dome region the stress is highest at the port boss–dome boundary (section line B) and decreases steadily from section line B to C. The hoop stress increases in the port boss end transition region from section line C to D. This increase in hoop stress is partly due to the decrease in the liner's wall thickness as a function of the distance from the dome region to the cylindrical region. Hoop stress in the cylindrical region is constant because this region has a uniform radius, and thickness.

Meridonial stress throughout the ZD154 liner is shown in Figure 4.8. In the dome region, the meridonial stress magnitudes are highest near the beginning of the dome region (section line B) and decrease steadily towards the base of the dome (section line C). In the dome and closed end regions, applied pressure causes the liner to bend outwards. The result is that the outer liner surface experiences tension and the inner dome surface experiences compression. In the cylindrical region, the meridonial stress is constant because this region has a uniform, radius, and thickness.

4.4 Summary

The FE model for the W320 liner predicts that failure will occur in the vessel's cylindrical region. This prediction is consistent with experimentally determined burst test results. The burst pressure of a Dynetek W320 liner was found to be 11.9 MPa (1726 psi). The experimental burst pressure is higher than the burst pressure predicted by the FE model. Reasons for the discrepancy are that only one liner was burst test, and Dynetek has found that their liners have measured yield stresses that are higher than the theoretical ultimate tensile stress (UTS) for the Al 6061-T6 liner material.

The FE model that was validated in Chapter 3 was used to model the Dynetek ZD154 liner. The vessel pressure was 1.38 MPa (200 psi). The FE model for the ZD154 liner determined that all of the liner's regions satisfy the factor of safety of 2.35 required by cylinder standards [29,30]. Maximum stresses occur in the liner's dome and closed end regions. In the dome region, the factor for safety for burst failure was 3.45. In the closed end region, the factor for safety for burst failure was 2.59. In Chapter 5, an IPV inner vessel that is an elongated version of the ZD154 liner is developed.

Chapter 5

IPV Design

5.0 Introduction

In this chapter, an IPV is designed using two standard Dynetek liners that are lengthened to attain a required volume. The IPV inner vessel will have the 318 L fuel storage volume required by the design criteria in Appendix A1.1. The IPV outer vessel will have the 416 L volume needed to enclose the inner vessel. The first part of this chapter provides calculations to determine the required dimensions of the inner and outer vessel design. The second part of this chapter provides a thermal analysis to determine the IPV heat leak, hold time, boil off rate, thermal expansion of the inner vessel, and the IPV fuel storage density.

5.1 Design of IPV Inner Vessel

Dynetek's current manufacturing process involves a pressing operation followed by a forming operation. The IPV inner vessel will be constructed from a ZD154 liner that will require an additional stretching operation prior to the forming operation. Section 5.1.1–5.1.3 discuss the pressing, stretching, and forming operations.

5.1.1 Pressing Operation

The pressing operation involves pressing plates using a press machine to create liner cups that consist of the closed end (pressed end), cylindrical region, and dome region shown in Figure 5.1.

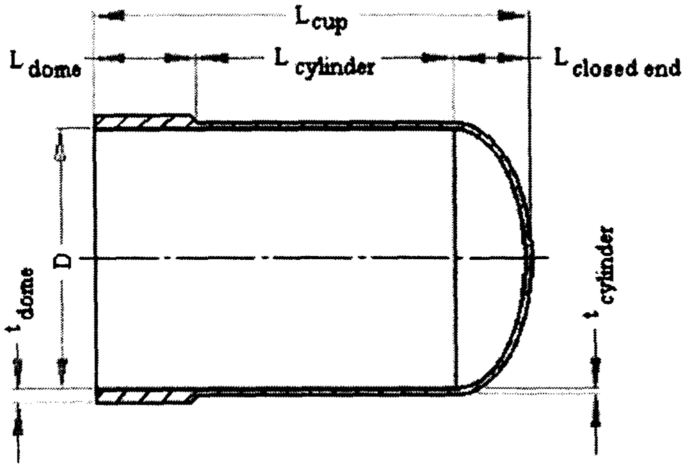

Figure 5.1: Section view of a ZD154 liner cup created in the pressing operation.

Equation 5.1 calculates the length of the liner cup L_{cup} as the sum of the ZD154 liner's cylinder region $L_{cylinder}$, closed end region $L_{closedend}$, and dome region length L_{dome}.

Table 5.1: Variables used in liner cup length equation

Variable	Description	Value [m]
L_{dome}	ZD154 dome region length	0.230
$L_{cylinder}$	ZD154 cylinder region length	0.630
$L_{closedend}$	ZD154 closed end region length	0.136

$$L_{cup} = L_{cylinder} + L_{closedend} + L_{dome} \tag{5.1}$$

Using Equation 5.1 and the values in Table 5.1, a ZD154 liner cup length of 0.996 m was calculated.

5.1.2 Extending Operation

The extending operation involves lengthening the dome and cylindrical regions of the liner cup shown in Figure 5.1 by an amount required to store a fuel volume required by the design criteria given in Appendix A1.1. Dynetek is able to increase the ZD154 liner length using a process that involves cold working and then lengthening the liner [29]. This process subsequently reduces the wall thickness in the dome and cylinder regions by equal amounts. Figure 5.2 shows a section view of the liner cup after the extending operation. The thickness and shape of the liner cup's closed end region will remain the same as the current ZD154 liner's closed end region since it is not extended.

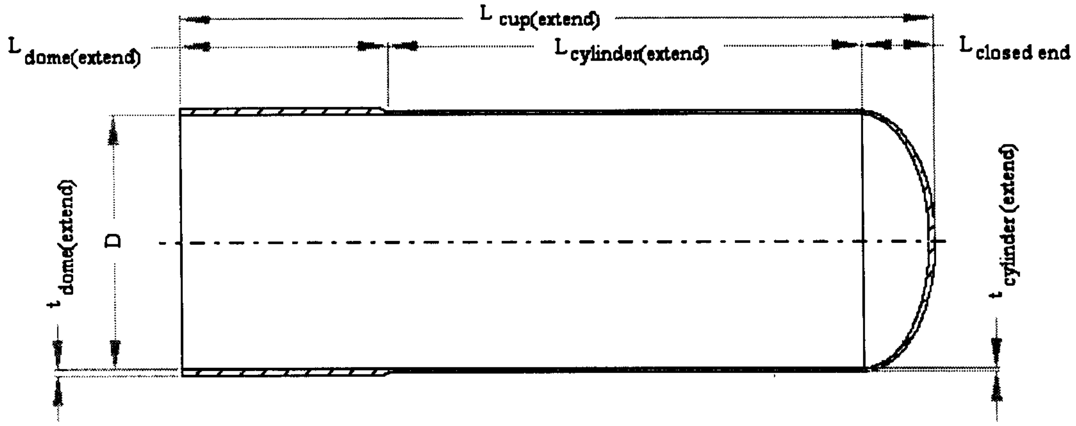

Figure 5.2: Section view of ZD154 liner cup after extending operation.

Dynetek is able to increase the ZD154 liner. The final length of the extended ZD154 liner cup's dome region $L_{dome(extend)}$ is calculated using Equations 5.2-5.4. Equation 5.2 represent the assumption that the volume of material in the dome region is assumed to remain unchanged as a result of extending of the liner. Table 5.2 shows the variables used in Equations 5.2-5.3.The extended ZD154 dome thickness, $t_{dome(extend)}$,was chosen to be $0.5t_{dome}$ because this thickness corresponds to the extended liner cup length required to create an inner vessel with the required 318 L volume.

$$V_{dome(extned)} = V_{dome} \tag{5.2}$$

$$\pi L_{dome(extend)} \cdot D \cdot t_{dome(extend)} = \pi L_{dome} \cdot D \cdot t_{dome} \tag{5.3}$$

Table 5.2: Variables used in dome region equations

Variable	Description	Value [m]
L_{dome}	ZD154 dome length	0.230
D	IPV inner diameter	0.507
t_{dome}	ZD154 dome thickness	0.008
$t_{dome(extend)}$	Extended ZD154 dome thickness	0.004

Equation 5.3 is rearranged to give the expression for the extended ZD154 dome length shown in Equation 5.4.

$$L_{dome(extend)} = \frac{t_{dome} \cdot L_{dome}}{t_{dome(extend)}} \tag{5.4}$$

Values for variables in Table 5.2 were substituted into Equation 5.4 to give an extended dome region length of 0.460 m.

The final length of the extended cylindrical region is calculated by assuming that the cylindrical region is extended by the same amount as the dome region. Therefore, the ratio of the extended and unextended wall thickness is the same in the cylindrical and dome regions as shown in Equation 5.5. Equation 5.5 represents the assumption that the volume of material in the cylinder region is not assumed to change due to extending of the liner. Table 5.3 describes the variables used in Equations 5.5-5.8.

$$\frac{t_{dome}}{t_{dome(extend)}} = \frac{t_{cylinder}}{t_{cylinder(extend)}} \tag{5.5}$$

$$V_{cylinder(extend)} = V_{cylinder} \tag{5.6}$$

$$\pi L_{cylinder(extend)} \cdot D \cdot t_{cylinder(extend)} = \pi L_{cylinder} \cdot D \cdot t_{cylinder} \tag{5.7}$$

Table 5.3: Variables used in cylindrical region equations

Variable	Description	Value [m]
$L_{cylinder}$	ZD154 cylinder length	0.630
D	IPV diameter	0.507
$t_{cylinder}$	ZD154 cylinder thickness	0.00525
$t_{cylinder(extend)}$	Extended ZD154 cylinder thickness	0.0026

Equation 5.7 is rearranged to give the expression for the extended ZD154 liner cup cylinder region length shown in Equation 5.8.

$$L_{cylinder(extend)} = \frac{t_{cylinder} \cdot L_{cylinder}}{t_{cylinder(extend)}} \tag{5.8}$$

Using Equation 5.8, the extended ZD154 cup's cylindrical regions length is 1.260 m. The extended ZD154 cup length is equal to the sum of the extended cylinder region, closed end region, and the extended dome region length before it is formed.

$$L_{cup(extend)} = L_{cylinder(extend)} + L_{closedend} + L_{dome(extend)} \tag{5.9}$$

Using equation 5.9, the extended ZD154 cup length is 1.876m.

5.1.3 Forming Operation

The forming operation involves shaping the dome region of the extended liner cups to form the dome shape shown in Figure 5.3. The ZD154 liner length L_{ZD154} equals the ZD154 liner cup length after forming, $L_{cup(form)}$. This length equals the sum of the ZD154 liner's cylinder region, closed end region, and formed dome region lengths as shown in Equation 5.10.

Table 5.4: Variables used in forming operation equations

Variable	Description	Value [m]
$L_{cylinder}$	ZD154 cylinder length	0.630
$L_{closedend}$	Length of Closed End	0.136
L_{dome}	Length of Dome Region	0.163

$$L_{ZD154} = L_{cup(form)} = L_{cylinder} + L_{closedend} + L_{dome(form)} \tag{5.10}$$

Using Equation 5.10, and the values in Table 5.4, the ZD154 cup length after forming is 0.929 m.

The IPV inner vessel's final length, L_{IPV} equals the extended ZD154 cup length after forming, $L_{cup\ (extend,\ form)}$. Equation 5.11 represents the assumption that the ratio of the ZD154 liner lengths before and after forming is the same for the ZD154 liner cup and the extended ZD154 liner cup.

$$\frac{L_{IPV}}{L_{cup(extend)}} = \frac{L_{cup(extend,form)}}{L_{cup(extend)}} = \frac{L_{cup(form)}}{L_{cup}} \tag{5.11}$$

Equation 5.11 is rearranged to give the expression for the IPV vessel's final length given in Equation 5.12.

$$L_{IPV} = L_{cup(extend,form)} = L_{cup(extend)}\left(\frac{L_{cup(form)}}{L_{cup}}\right) \tag{5.12}$$

Using Equation 5.12, the IPV vessel's final length is 1.75 m. An IPV with this length is capable of storing a fuel volume of 318 L (75 Gallons). In Chapter 6, different inner vessel volumes are obtained by varying the amount that the liner is lengthened in the extending operation.

5.1.4 Cost Analysis

Dynetek provided a cost estimate for construction of an extended liner based on a previous project they completed for a client [28]. Tooling costs are estimated to be 20,000 USD to order and install the new mandrel for the flow former. Development costs are estimated to be 6000 USD (60 hours engineering time x 100 USD/hr) and (20 production technician hours x 50 USD) 1000 USD. Prototype costs are estimated to be 2000 USD/prototype for construction of 5-10 prototypes. The total cost to produce 5 prototypes is estimated to be 37,000 USD.

5.1.5 Stress Analysis

A cross-section view of the IPV vessel with labeled section lines is shown in Figure 5.2. The IPV vessel sections and their thicknesses are listed in Table 5.5.The FE model's Von Mises stresses for the proposed IPV inner vessel design are shown in Figure 5.3. A pressure P of 1.38 MPa (200 psi) was applied to the IPV liner. The yield stress of the liner is assumed to be 290 MPa [28].

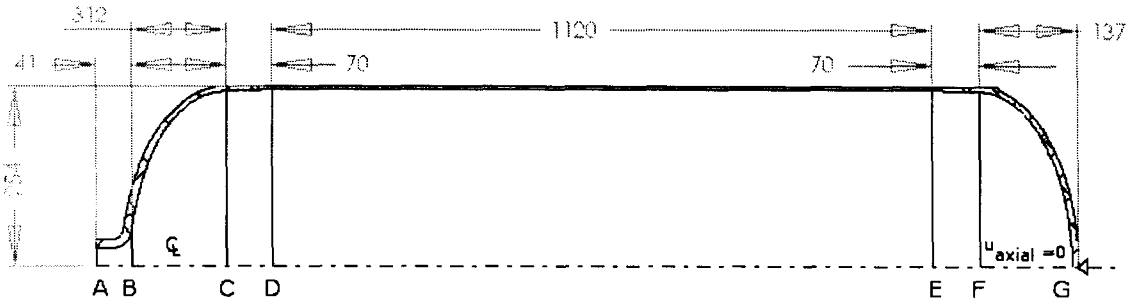

Figure 5.3: Section view of IPV Inner Vessel. Units in mm.

Table 5.5: Summary of IPV inner vessel sections and thicknesses

Section	Description	Thickness [mm]
A-B	Port Boss	7.9-8.2
B-C	Dome	8.2-5.8
C-D	Port Boss End Transition	5.8 -2.6
D-E	Cylindrical	2.6-2.6
E-F	Closed End Transition	2.6-10.1
F-G	Closed End	10.1-11.2

In the dome region from section line B to C, stresses are much lower for the IPV than for the ZD154 liner (Figure 4.2) because the IPV dome region has the same shape as the Dynetek W320 vessel dome region that was analyzed in Section 4.2.

In the cylindrical region from section line D to E, the factor of safety against yield is 2.40 which is above the factor of safety of 2.35 the design criteria requires. Cylindrical region stress is higher for the IPV than for the ZD154 liner since the IPV vessel's 2.6 mm wall thickness is half the wall thickness of the ZD154 liner in the cylindrical region.

In the closed end region from section line F to G, the factor of safety against yield is 2.59 which is above the factor of safety the design criteria requires. Closed end region stresses for the IPV are identical to those for the ZD154 liner since both vessels have identical closed end regions.

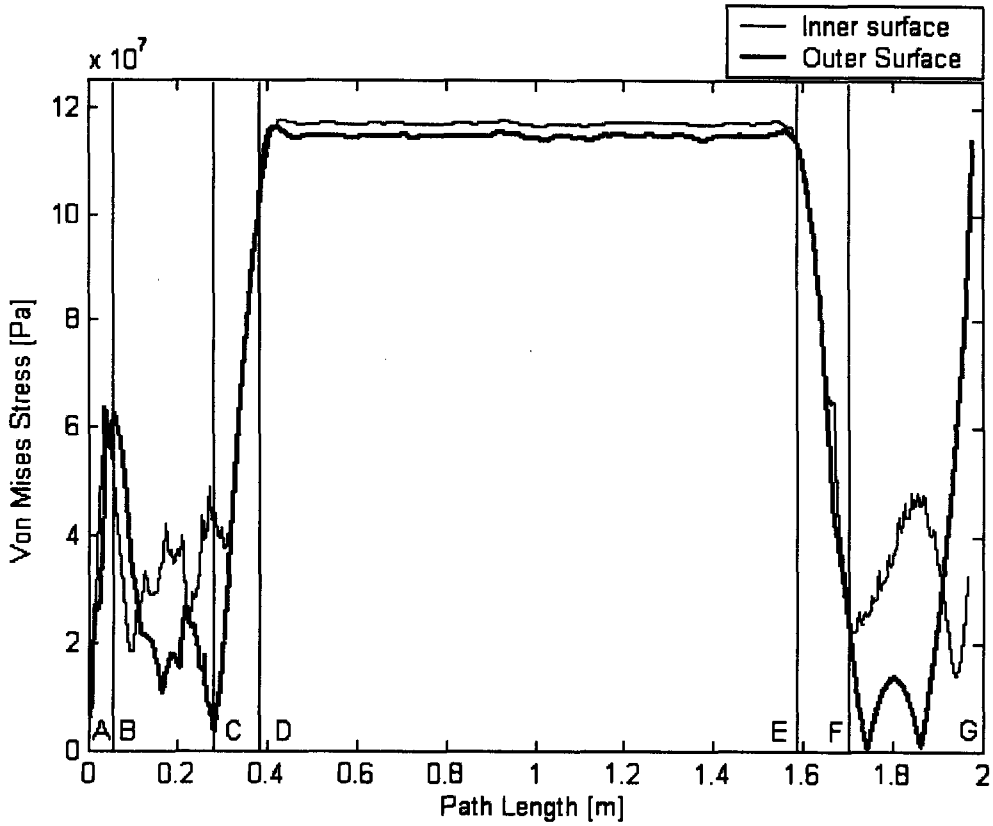

Figure 5.4: Von Mises Stress for the proposed IPV inner liner.

5.1.6 Possible Design Modifications

IPV stresses could be reduced by creating an IPV vessel with thicker walls by using a thicker plate in the pressing operation. To develop an increased thickness vessel new tooling is required for Dynetek's press. Tooling cost will be similar to the manufacturing costs listed in Section 5.1.4. Dynetek has recently created a thicker liner for a 700 bar cylinder using a pressed cup with an increased wall thickness of 9 mm.

5.2 Design of IPV Outer Vessel

The IPV outer vessel will be manufactured by welding the dome portion of the Dynetek ZM180 liner to an extended length cylindrical portion of the ZM180 liner.

The outer vessel could fail due to buckling since it experiences a pressure of 1atm externally and a vacuum internally. Appendix A2.1 provides an estimate of external pressure required for buckling. These calculations assume a thin walled cylindrical vessel with closed end. It was determined that this vessel collapses when the external pressure is 5 atm. These results suggest that the IPV outer vessel wall thickness could be reduced. However, the results are not able to predict the collapse pressure in the IPV outer vessel's dome region, closed end region, and weld locations.

5.3 Thermal Analysis of IPV

A key aspect of any cryogenic storage vessel is thermal isolation. Ideally, the fluid in the cold space remains cold as long as the vehicle operating profile dictates. This is obviously not possible and the degree of thermal isolation has a direct impact on the tank cost and size. In the following section, the concept tanks are reduced to a simple thermal network and a coarse thermal analysis that determines the IPV's heat leak, boil off rate, and hold time values is performed.

Significant heat leak occurs due to radiative heat transfer between the cold inner vessel and the warm outer vessel, and conduction through the stainless steel tubing and the

Significant heat leak occurs due to radiative heat transfer between the cold inner vessel and the warm outer vessel, and conduction through the stainless steel tubing and the supports. The multi layer insulation (MLI) is wrapped around the inner wall of the pressure vessel. MLI is a type of cryogenic insulation that consists of alternating layers of a highly reflective material such as aluminized Mylar, and a low conductivity spacer such as fiberglass or nylon [31].

The stainless steel tubing is used to deliver and withdraw fuel from the IPV. The valve blocks are used to support the inner pressure vessel. A thermal network model of the IPV is schematically represented in Figure 5.5.

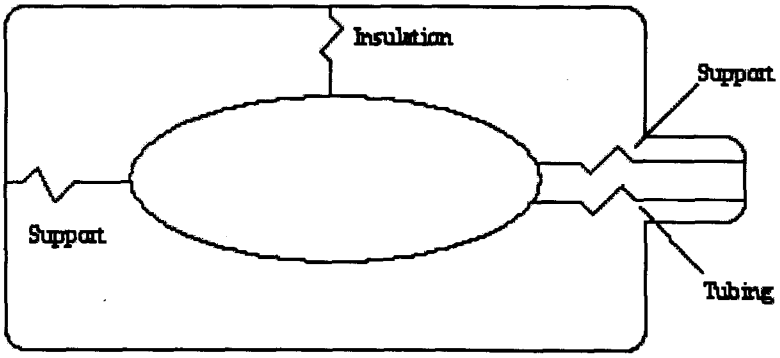

Figure 5.5: Thermal network model of IPV [12].

5.3.1 Calculation Methods for Thermal Performance Variables

Thermal performance values such as the heat leak, hold time, and boil off rate for the IPV design are calculated in Appendix A3. The heat leak through a component is determined using Equation 5.13.

$$Q = \frac{T_2 - T_1}{R} = S \cdot (K(T_2) - K(T_1)) \tag{5.13}$$

In Equation 5.13, R is the thermal resistance of the component, and S is the shape factor given in Equation 5.14. The shape factor is calculated using a cross-sectional area $A(x)$, and a component position that varies from x_1 to x_2. The thermal conductivity integral $K(T)$

is defined using empirically derived equations contained in Appendix A3.1. In Equation 5.13 the temperature of the component varies from T_1 to T_2.

$$\frac{1}{S}=\int_{x1}^{x2}\frac{dx}{A(x)} \tag{5.14}$$

The following methods were used to calculate heat leak in various IPV components. Heat leak from the multi layer insulation is determined using empirically derived equations that determine effective thermal conductivity, k_t. Determining heat leaks occurring in multilayer insulation is an inexact science since the empirically derived equations for thermal conductivity can vary significantly. Several parameters are required to solve for the heat leak. These include the emmisivity of the MLI ε, the Stefan-Boltzman constant σ, the number of MLI layers N, and the thickness of the MLI layers ΔX. Details of determining the thermal resistance of MLI can be found in Appendix A3.1. The valve block consists of the stainless steel port blocks, the G-10 sleeve, and ports for the stainless steel tubing. The temperatures at the end of the inner port block T_C and outer port block T_H are assumed to be 115 K and 300 K respectively. The total resistance for the valve block is calculated by adding the resistances of the G-10 connector, and the stainless steel pin and bushing. The intermediate temperatures found at each node of the network diagram were determined using an iterative procedure which is described in Appendix A3.1.

Hold time is the time required for pressure in the IPV to reach the maximum allowable working pressure (MAWP). When the MAWP is reached, the IPV will begin to vent. Hold time is estimated using Equation 5.15. This equation is a function of heat leak Q, change in internal energy u_2-u_1, and mass of LNG being stored m_{LNG}. The hold time equation is derived in Appendix A3.2.

$$t_{hold}=\Delta t=\frac{(u_2-u_1)\cdot m_{LNG}}{Q} \tag{5.15}$$

Boil-off rate is the rate that LNG leaves an IPV that is open to the environment. Boil-off rate $m_{boil\ off}$ is calculated using Equation 5.16 where Q is the heat leak, and h_{fg} is the enthalpy for the LNG. The boil-off rate equations are derived in Appendix A3.3.

$$m_{boil\ off} = \frac{Q}{h_{fg}} \tag{5.16}$$

5.3.2 Thermal Performance Results

Table 5.6 provides data for heat leak, hold time, and boil-off rate for the ALOSS and prototype IPV designs. The ALOSS design is discussed in Appendix A3.1.2.

Table 5.6: Thermal performance of each design[†]

Design	**Taylor Wharton (68 Gallon)**	**IPV**
Heat Leak	20.1 W* (12.5 W)**	6.5 W
Hold Time	60 hr* (100 psi start, 200 psi relief) (89 hr)**	209 hr (100 psi start, 200 psi relief)
Boil Off Rate	146 g/hr* (126 g/hr)**	60 g/hr

*Experimental values from ALOSS. Predicted ALOSS heat leak under-estimates the real heat leak because only heat leak occurring from the major components was considered.
** Predicted values calculated in Appendix A3.
[†] Refer to Appendix A3 for a breakdown of values found in the table.

A summary of the different heat leak path contributions for the IPV are shown in Table 5.7 and the supporting calculations are given in Appendix A3.1.1. The most significant heat leak is due to structural supports such as the valve block and rear supports while the MLI has the highest thermal resistance.

Table 5.7: Heat Leak occurring in various IPV Components

Component	**Heat Leak [W]**
MLI	2.28
Stainless Steel Tubing	0.27
Valve Block support	2.10
Rear support	1.80
Total	6.45

5.3.3 Discussion of Thermal Performance Results

The total heat leak that occurs in the IPV is equal to the sum of the heat leaks in the supports, MLI insulation, and tubing: approximately 6.5 W. The heat leak due to the MLI insulation is approximately 2.3 W assuming 15 layers of aluminized Mylar are used as the MLI blanket. Since the heat leak in the MLI is not very large, it may be possible to use alternative materials for insulation that are less complicated than MLI. Heat leak through the stainless steel tubing is small. A worst case scenario assuming the two fuel lines conduct heat to the inner vessel while no LNG is being removed or put into the tank gives a heat leak of approximately 0.27 W. Heat leak in the supports (valve block and rear support) is 3.9 W. This heat leak could have been much higher if a G-10 sleeve was not used for the valve block and a G-10 support pin was not used for the rear support.

The calculated heat leak of the ALOSS tank (Taylor-Wharton 68 gallon) is less than the experimentally determined value. Calculations are shown in Appendix A3.1.2. The deviation can be attributed to the simplified nature of the thermal model, and the fact that MLI thermal conductivity values can vary by an order of magnitude depending upon the specific installation. In fact, MLI thermal conductivity values in real applications are rarely as good as the values determined in controlled laboratory tests. In any case, the order of magnitude of the calculated value is comparable to the experimental value suggesting the methodology is valid.

The prototype tank's calculated hold time of 8.7 days compares to the experimentally determined ALOSS hold time of approximately 3 days. Detailed calculation can be found in Appendix A3.2.

The boil off rate of the cryogenic fluid is estimated using the enthalpy of evaporation h_{fg} and the heat leak into the tank. The IPV boil off rate was calculated to be approximately 60 g/h which is much less than the ALOSS tank's experimentally determined boil of rate of 146 g/h. The large discrepancy in boil off rates is due to the different heat leak values for the ALOSS tank and the IPV. Detailed calculations can be found in Appendix A3.4.

5.3.4 Thermal Deformation of IPV Inner Vessel

Thermal analysis was performed to determine the axial expansion of the IPV inner vessel due to a change in temperature from 298 K to a cryogenic temperature of 115 K.

Knowing the axial expansion of the vessel is important when creating a detailed IPV design since it helps determine an appropriate stiffness and configuration for the spring-like mechanism that separates the IPV's inner and outer vessel and is used to accommodate expansion. A thermal model will also assist in determining the deformation occurring in critical regions such as the port bosses that contain structural support components that consist of dissimilar materials.

5.3.4.1 Finite Element Method Validation

The Finite Element (FE) method used to determine the IPV's thermal deformation was validated by creating a model of a 1.75 m long cylindrical rod whose results are compared to closed form solutions. The FE model was meshed with the three dimensional element Solid45. This element is convenient for modeling simple shapes such as cylindrical rods. Axial expansion caused by a change in temperature from 298 K to 115 K was determined.

Equation 5.17 is a mathematical expression for the thermal expansion. This equation assumes that the vessel expansion varies linearly with change in temperature. The thermal coefficient of expansion for aluminum *CTE* was 23.6 x 10^{-6} deg K^{-1}. Results are given in Table 5.8.The percent difference between the calculated axial expansion and the FE model's axial expansion is less than 0.01%.

$$\Delta L = CTE \cdot \Delta T \cdot L_{liner} \tag{5.17}$$

Table 5.8: Comparison between FE model and calculated axial expansion for rod

	Axial Expansion [mm]
FE Model	7.833
Closed Form	7.832

5.3.4.2 FE Analysis of IPV Inner Vessel

A FE thermal model of the IPV inner vessel was created using Plane42 elements. Axial expansion caused by a change in temperature from 298 K to 115 K was calculated using Equation 5.17.

Table 5.9 shows the FE model and mathematically derived thermal expansion results. The percent difference between the calculated axial expansion and the FE model's axial expansion is less than 0.15%. IPV design will have to account for the significant amount of axial expansion occurring in the inner vessel.

Table 5.9: Comparison between IPV FE model and IPV calculated axial expansion

	Axial Expansion [mm]
FE Model	7.691
Closed Form	7.681

5.4 IPV Fuel Storage Density

The IPV fuel storage density is defined in Equation 5.18. Fuel storage density equals the mass of LNG stored by the inner vessel divided by the volume of the outer vessel. Variables used to calculate fuel storage density are given in Table 5.10.

$$\rho_{storage} = \frac{m_{LNG}}{V_{total}} = \frac{\rho_{LNG} \cdot V_{LNG}}{V_{total}} \tag{5.18}$$

Table 5.10: Variables used to Calculate Fuel Storage Density

Variable	**Value**	**Description**
ρ_{LNG}	424 kg/m^3	Density of LNG
V_{LNG}	318 L	Inner Vessel Volume
V_{total}	413 L	IPV Volume
m_{LNG}	135 kg	Mass of LNG

Equation 5.18 gives a fuel storage density, $\rho_{storage}$ of 0.33 kg/L. Therefore, the IPV satisfies the design criterions 0.30 kg/L fuel storage density requirement.

5.5 Summary

The IPV inner vessel design was created by stretching a Dynetek ZD154 to the length required to satisfy the design criteria fuel storage requirement listed in Appendix A1.1. The developed IPV inner vessel design had a length of 1.75 m, and a cylindrical region wall thickness of 2.6 mm. In Chapter 6, a sensitivity analysis will be performed to determine the inner vessel volume as a function of length.

Stress analysis results for the IPV inner vessel indicate that it can operate at 1.38 MPa (200 psi) with a factor of safety of at least 2.35 against burst. These results show that it is possible to construct a lightweight seamless aluminum liner that can store LNG at the same operating pressure as stainless steel tanks without an unacceptable increase in size or mass.

An IPV outer vessel design was developed. The design involves welding the dome portion of the Dynetek ZM180 liner to an extended length cylindrical liner portion.

The thermal performance of the IPV and its individual components was estimated based on initial conditions of T =115 K, P =1 atm, and 10% ullage. Calculations gave an IPV heat of 6.5 W, a hold time of 209 hours, and a boil off rate of 60 g/hr. Thermal performance results were found to be superior to ALOSS vessel results given in Appendix A3.

A FE model was used to calculate thermal expansion of the IPV inner vessel. Thermal expansion was calculated as 7.69 mm. FE results are consistent with mathematical results. The thermal expansion is significant and will need to be considered for future designs.

The IPV fuel storage density was calculated to be 0.33 kg/L, which satisfies the design criteria requirement given in Appendix A1.1.

Chapter 6

Sensitivity Analyses

6.0 Introduction

A sensitivity analysis was conducted on the IPV design shown in Figure 5.3 to determine how its performance is affected by changes in various design variables. The first section of this chapter contains the thermodynamic sensitivity anlaysis. IPV fuel mass and ullage fraction are plotted as a function of the maximum working pressure. It was assumed that the end condition is 100% liquid. The second was of hold time as a function of start pressure. The second section of this chapter contains a structural sensitivity analysis. IPV volume and pressure are plotted as a function of length. Additionally, maximum pressure versus IPV wall thickness in the cylindrical region was found.

6.1 Thermodynamic Sensitivity Analysis

6.1.1 Ullage fraction versus Maximum Pressure

A phase diagram for methane showing the fuel pressure and phase changes that occur due to increasing temperature is given in Figure 6.1. The fuel storage volume is constant so the fuel density is assumed to be constant. When the IPV is filled with fuel at time t_o, the fuel is a mixture of liquid and vapour and the liquid fuel is stored in the inner vessel. Heat leak causes the fuel temperature and pressure to rise until the fuel is 100% liquid at time t_{hold}. Ullage space V_{ullage}, is a storage volume used to compensate for the expansion of liquid fuel as the fuel temperature increases due to heat leak into the inner vessel.

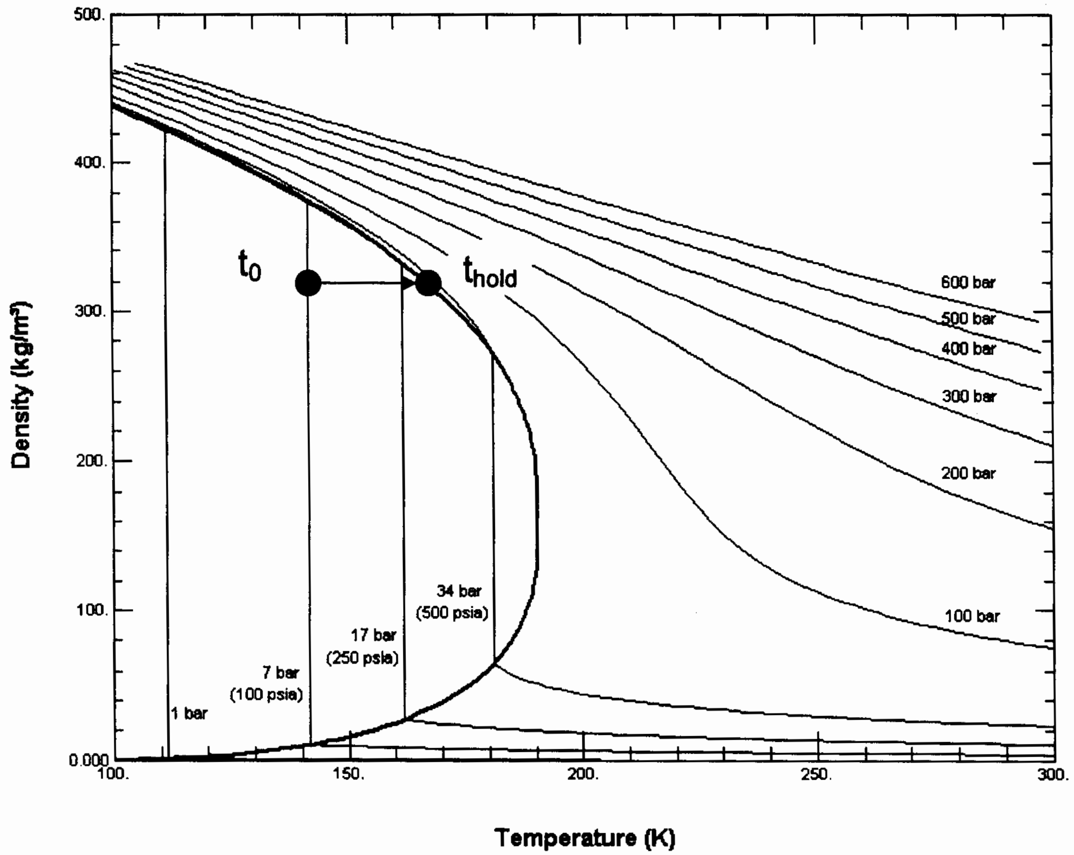

Figure 6.1: Phase diagram for methane showing density versus temperature at various pressures. The change in fuel pressure that occurs due to a change in temperature assuming a constant density is indicated by the arrow. Fuel becomes 100% liquid at t_{hold}.

Ullage fraction V_{ullage}/V_{total} ,is the portion of the IPV volume occupied by the ullage space. The IPV ullage fraction versus maximum pressure was determined using Equation 6.1. This equation is derived in Appendix A3.4 and calculates ullage fraction as a function of liquid and vapour densities (ρ_{liquid}, ρ_{vapor}) and volumes calculated at the IPV start and maximum pressure. The variable X represents the vapor mass fraction for the LNG, m_{vapor}/m_{total} ,that was calculated at the start pressure.

$$\frac{V_{ullage}}{V_{total}} = X \cdot \frac{\left(\dfrac{\rho_{liquid}}{\rho_{vapor}}\right)}{1 + X \cdot \left(\dfrac{\rho_{liquid}}{\rho_{vapor}}\right) - X} \tag{6.1}$$

Results in Figure 6.1 indicate ullage fraction increases as maximum pressure increases.

6.1.2 Fuel mass versus Maximum Pressure

The IPV fuel mass versus maximum pressure was determined using Equation 6.2. This equation was derived in Appendix A3.4. Fuel mass is calculated by solving for the fuel's liquid density and vapor density at the starting pressure. Liquid volume and ullage volume at a given maximum pressure are determined using ullage fraction calculations described in Section 6.1.1.

$$m_{total} = (\rho_{liquid} \cdot V_{liquid}) + (\rho_{vapor} \cdot V_{ullage}) \qquad (6.2)$$

Results shown in Figure 6.1 indicate that fuel mass decreases as maximum pressure increases. The reason for the decrease in fuel mass is that the ullage space requirement increases as maximum pressure is increased with the constraint that the end condition is 100% liquid. Therefore, the fraction of the IPV occupied by the inner vessel decreases causing the fuel mass to decrease.

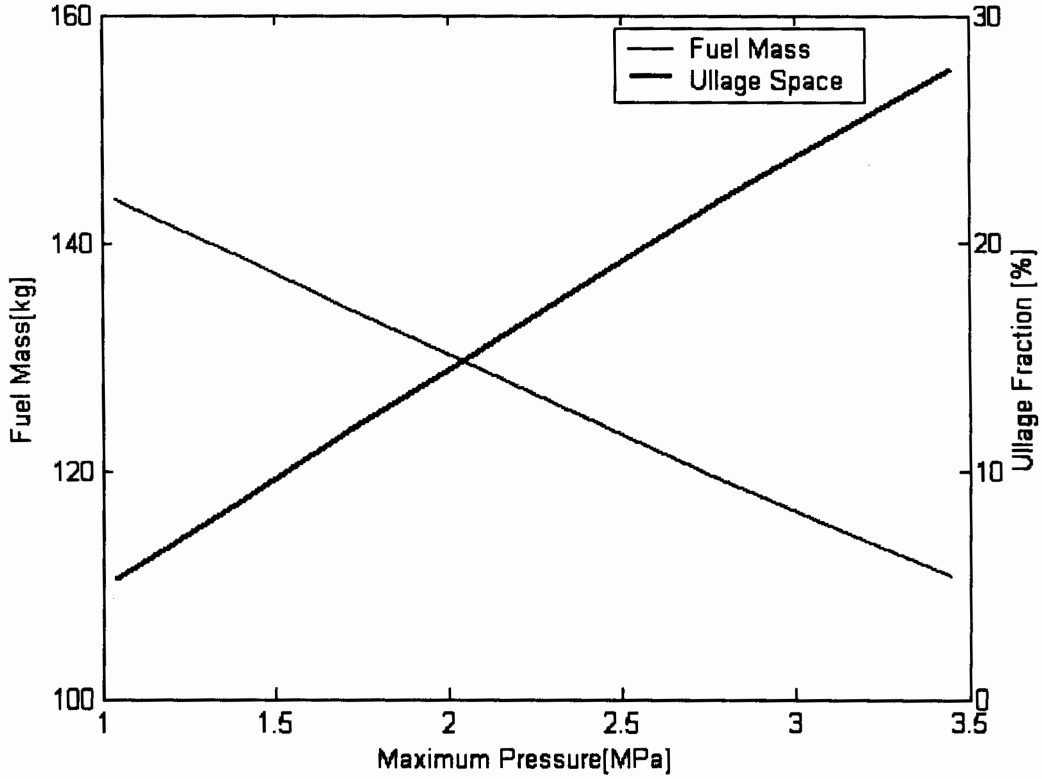

Figure 6.2: Mass of fuel and ullage fraction versus maximum pressure. Start pressure is 0.69 MPa (100 psi), and a 100 % liquid end condition is assumed.

6.1.3 Hold Time versus Start Pressure

Hold time is the time required for the LNG pressure to build up to a critical maximum pressure (vent pressure) when the tank is closed to the external environment. The variation in the hold time caused by varying the start pressure was determined using Equation 6.3. This equation was derived in Appendix A3.2. Hold time is a function of the IPV heat leak, Q, LNG mass, m_{LNG}, and the LNG internal energy at the start and maximum pressure, u_1, u_2.

$$t_{hold} = \frac{(u_2 - u_1)\cdot m_{LNG}}{Q} \tag{6.3}$$

Figure 6.2 shows the hold time results assuming the heat leak value of 6.5 W which was calculated in Appendix A3.1. The benefit associated with using a maximum pressure larger than 1.38 MPa (200 psi) is not significant if a start pressure of 0.69 MPa (100 psi) is assumed. For this start pressure, the hold time only increases by 2 days if the maximum pressure increases to 3.45 MPa (500 psi). However, the hold time drops significantly if a maximum pressure lower than 1.38 MPa (200 psi) is used. For instance, if the IPV maximum pressure drops to 1.04 MPa (150 psi), the hold time drops by 3 days.

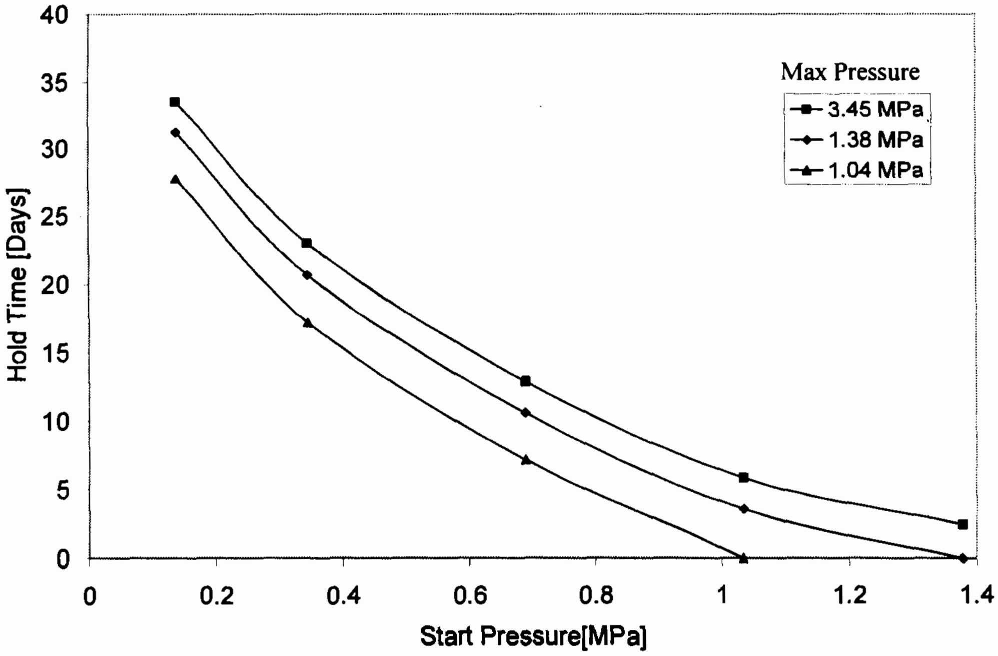

Figure 6.3: Hold time versus starting pressure, categorized by maximum pressure.

6.2 Structural and Dimensional Sensitivity Analysis

6.2.1 Variation of IPV Volume

The variation in volume caused by varying the length of the IPV inner vessel design developed in Chapter 5 was determined. Volume versus length was calculated using Equation 6.4. In this equation, V_{total} is the IPV volume, L_{IPV} is the IPV length, and r_{ave} is the average internal radius of the IPV inner vessel.

$$V_{total} = \pi \cdot r_{ave}^{2} \cdot L_{IPV} \tag{6.4}$$

Results shown in Figure 6.3 indicate that IPV volume increases linearly with length. The IPV inner vessel shown in Figure 5.3 has a length of 1.75 m that was calculated in Chapter 5. Therefore, Figure 6.3 indicates the inner vessel fuel storage volume is 318 L.

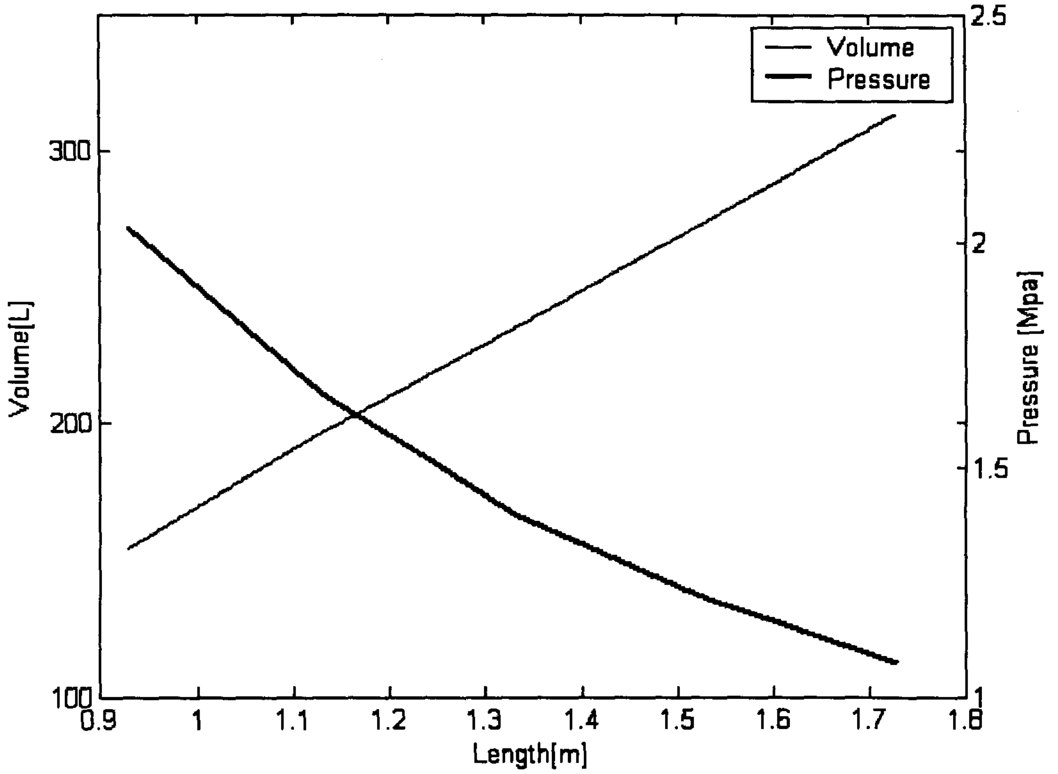

Figure 6.4: IPV inner vessel volume and maximum pressure versus vessel length

6.2.2 Variation of IPV Maximum Allowable Pressure

The IPV maximum allowable working pressure (MAWP) versus the cylindrical region wall thickness is calculated using Equation 6.5. This equation is derived in Appendix 2.3. Variables used in this equation are summarized in Table 6.1.

$$P = t\left(\frac{\sigma_Y}{SF}\cdot\frac{4}{\sqrt{3}}\cdot\frac{1}{2r_{out}-t}\right) \tag{6.5}$$

Table 6.1: Variables used to determine Pressure versus Wall Thickness and Length

Variable	Value	Description
σ_y	290 MPa	Yield Stress for Aluminum
SF	2.35	Safety Factor for Burst
r_{out}	253 mm	Outer radius of Vessel
$L_{cylinder}$	0.630 m	ZD154 cylinder length
$t_{cylinder}$	0.00525 m	ZD154 cylinder thickness

The IPV maximum allowable pressure P versus axial length L is calculated by assuming the IPV length is increased using the stretching operation described in Chapter 5. Therefore, an increase in IPV length results in a decrease in wall thickness. Equation 6.5 gives the MAWP versus wall thickness. Equation 5.8 gives wall thickness versus IPV length for a vessel being stretched. Equation 5.8 is substituted into Equation 6.5 to obtain the IPV MAWP versus axial length expression in Equation 6.6. Variables used in this equation are summarized in Table 6.1.

$$P = \frac{t_{cylinder}\cdot L_{cylinder}}{L}\left(\frac{\sigma_Y}{SF}\cdot\frac{4}{\sqrt{3}}\cdot\frac{1}{2r_{out}-\dfrac{t_{cylinder}\cdot L_{cylinder}}{L}}\right) \tag{6.6}$$

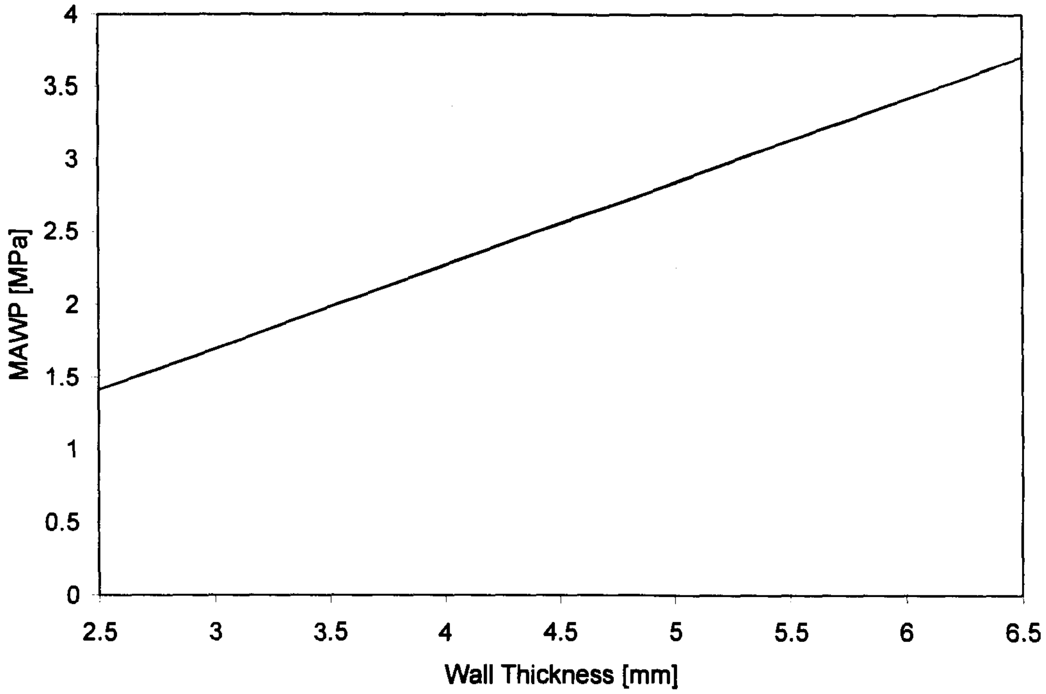

Figure 6.5: Maximum allowable working pressure (MAWP) versus wall thickness for a cylindrical wall section with the same outer diameter as the ZD154 liner, and a FS of 2.35 against yield failure. Current cylindrical region wall thickness for the ZD154 liner is 5.25 mm.

The vessel stress was assumed to be the cylindrical wall's Von Mises stress. The MAWP corresponds to a Von Mises stress with a factor of safety of 2.35 against yield which the IPV inner vessel requires to satisfy the design criteria outlined in Appendix 1.1. Results shown in Figure 6.4 indicate that maximum pressure decreases when the vessel length is increased due to stretching of the vessel. Results shown in Figure 6.4 indicate that MAWP increases with increasing vessel wall thickness. In Section 5.1, the cylindrical section's wall thickness was calculated to be 2.6 mm. Therefore, Figure 6.5 indicates MAWP will be 1.38 MPa (200 psi).

6.2.3 Variation of Material

Changes in the IPV's material and structural properties caused by varying the IPV material were investigated. Materials considered include Al 6061-T6 used for Dynetek liners, and Stainless Steel SA 304 used for Taylor Wharton tanks discussed in Section 2.2.5. Material properties are shown in Table 6.2 [32].

Taylor Wharton tanks are required to follow DOT 4L standards. These standards require the vessel material to have a minimum yield stress of 207 MPa (30,000 ksi), and a minimum elongation at break of 30%. According to Taylor Wharton, the stainless steel material they use is cold rolled so it will have a yield stress that is significantly higher than the DOT 4L standard requirement [33]. The material properties will be based on cold rolled SS304 with a yield stress of 517 MPa and a percent elongation at break of 30% since it is the strongest SS304 material found that satisfies the DOT 4L minimum 30% elongation specification [33].

The IPV inner vessel described in Chapter 5 is manufactured by stretching a ZD154 vessel. Therefore, the inner vessel weight equals the ZD154 vessel's 29.4 kg weight [11,29]. An IPV inner vessel with similar dimensions but constructed using stainless steel weighs 85.5 kg. This weight was calculated using the stainless steel and aluminum density values in Table 6.2.

If the IPV is constructed using stainless steel, the wall thickness can be reduced since stainless steel is stronger than aluminum. The cold rolled stainless steel SA304 material has a yield stress of 620 MPa. Aluminum has a yield stress of 290 MPa. Therefore, the stainless steel inner vessel will have a safety factor for burst that is (620 MPa/290 MPa) 2.14 times that of the aluminum vessel. Therefore, an IPV vessel constructed using stainless steel can have its wall thickness and weight reduced by a factor of 1.78. This means that an IPV constructed using stainless steel having an equivalent factor of safety against burst as the aluminum IPV will weight 85.5 kg/2.14 = 40.0 kg. This weight is 10.6 kg higher than the aluminum IPV weight.

Table 6.2: Material and Structural Properties for Aluminum and Stainless Steel IPV Inner Liner. Both vessels have the same factor of safety for burst [33].

	Yield Stress [MPa]	**UTS [MPa]**	***E* [GPa]**	**ρ [kg/m^3]**	**CTE [μm·m^{-1}K^{-1}]**	**Weight[kg]**
Al 6061	290	310	70	2700	23.6	29.4
Stainless Steel 304	517	676	200	7850	17.3	40.0

A potential disadvantage with using aluminum for the IPV inner vessel is its endurance limit for cycling. A cycle occurs every time the vessel is refuelled with LNG. Endurance limit shouldn't be a problem since the number of cycles needed to reach the fatigue strength far exceeds the number of expected cycles in the vessel's lifetime. For instance, $5 \cdot 10^8$ cycles are needed to reduce the yield stress from 290 MPa to the fatigue strength of 95 MPa [33].

Thermal expansion of the IPV inner vessel is calculated using Equation 5.13. Coefficient of thermal expansion *CTE* values are given in Table 6.2, and the temperature is assumed to change from 115 K to 298 K. An aluminum IPV inner vessel has a larger length change due to thermal expansion. In Section 5.3, the linear expansion of an aluminum IPV inner vessel was calculated as 7.69 mm. If the IPV is constructed using stainless steel, the linear expansion is 5.64 mm.

6.3 Summary

Sensitivity analysis was conducted to determine how the IPV performance is affected by changes in various variables.

IPV fuel mass and ullage fraction versus maximum working pressure were determined. IPV stored fuel mass decreases and ullage fraction increases when maximum working pressure is increased. In addition, the IPV's hold time increases when the maximum pressure increases. An ideal IPV design should have a maximum fuel storage mass and hold time, and a minimum ullage fraction. The maximum pressure of 1.38 MPa (200 psi) used in Chapters 3-5 provide an acceptable fuel mass, ullage fraction, and hold time.

The IPV volume and operating pressure versus IPV length were determined. IPV volume was found to increase linearly with increasing IPV length, and IPV operating pressure decreased with increasing IPV length. The reason for the decrease in operating pressure is that the longer length IPV has a thinner wall thickness since it was created using the stretching operation discussed in Section 5.1.2.

The IPV maximum pressure versus cylindrical region wall thickness was determined. Calculations assumed a factor of safety of 2.35. IPV maximum pressure was found to increase from 1.38 MPa (200 psi) to 3.62 MPa (525 psi) as the cylindrical sections wall thickness increased from 2.5 mm to 6.5 mm.

A comparison was made of an IPV inner vessel using aluminum and stainless steel. The stainless steel IPV wall thickness was reduced so that both vessels had the same factor of safety against burst. The total weight reduction attained by using aluminum instead of steel for the inner vessel material was 10.6 kg.

7.0 Conclusion and Recommendations

7.1 Conclusion

There is a substantial market available for developing LNG vehicles. The market share of these vehicles will increase once cheaper and more reliable technologies are developed. This study investigated the feasibility of developing a cheaper, more reliable, and higher performance LNG storage vessel.

The proposed aluminum IPV design is much lighter than current stainless steel vessels, and unlike stainless steel vessels, it has a seamless inner vessel that does not require welds. The design involves using existing Dynetek liners, ZD154 and ZM180, for the inner and outer vessels so there should be lower development costs. The vessels will be elongated to hold more fuel. No composite overwrap is required so IPV costs will be much lower than current vessels using composite materials and outgassing of composite material will not be an issue. Therefore, the ability of the IPV to maintain a vacuum should be equivalent to or better than current stainless steel LNG tanks.

The finite element method used to analyze the IPV was developed and validated using simple vessel shapes with closed-form mathematical solutions. The method was used to determine stresses in the current IPV. The vessel models in this report were meshed using Plane42 elements. These models were used to analyze vessels with variable thickness, and calculated membrane and bending stresses in regions of high stress gradients.

The design criteria given in Appendix A1.1 can be achieved with an aluminum IPV design. LNG storage of 5 days is possible. The Maximum Allowable Working Pressure (MAWP) of 1.38 MPa (200 psig) is achievable using Dynetek seamless aluminum liners. The calculated IPV fuel storage density of 0.33 kg/litre satisfies the required 0.30 kg/litre fuel storage density.

The thermal analysis results indicate that the IPV heat leak will be approximately 6.5 W, and the hold time will be 11 days. The actual heat leak may be higher since the MLI thermal conductivity values in real applications are rarely as good as the values determined in controlled laboratory tests.

Sensitivity analysis results indicate that the advantage of operating the IPV with lower fuel pressures are that the inner vessel is less likely to fail due to burst, less ullage space is required, and the vessel can support a larger fuel mass. The disadvantage is that the IPV will have a reduced hold time. A pressure of 1.38 MPa (200 psi) was determined to be suitable for IPV operation.

7.2 Recommendations

More information should be acquired before a prototype IPV can be manufactured. The current Dynetek liners represent most of the overall IPV cost. Possible manufacturing methods to reduce the liner cost should be investigated.

Burst tests should be performed on Dynetek liners to validate the report's FE results. The Dynetek ZD154 liner should be burst to validate results in Chapter 4 and 5 that indicate initial failure in the liner's closed end region. A prototype IPV liner should be burst test to determine if the inner vessel's liner is strong enough to withstand a pressure of 1.38 MPa (200 psi) with a 2.35 factor of safety.

Various design changes to the IPV inner vessel should be investigated. The inner vessel's closed end region currently experiences the largest stresses. Possible design or manufacturing method changes should be considered to strengthen the closed end. The IPV's 2.6 mm wall thickness in the inner vessel's cylindrical section was determined to be sufficient to withstand a 1.38 MPa (200 psi) MAWP with a safety factor of 2.35. It may not be practical to use a 2.6 mm thick wall since a wall with this thickness is susceptible to damage due to accidental contact. However, the inner vessel will be wrapped with MLI which should protect the vessel from impact.

The outer vessel can withstand an external pressure of 1 atmosphere even if its wall thickness is reduced. A FE analysis could be done to determine the minimum wall thickness.

There are several ways that the IPV heat leak can be reduced. In Chapter 5, aluminized Mylar was chosen to be the MLI material. However, MLI materials with a lower thermal conductivity could be used to lower the heat leak. Heat leak could also be reduced by improving the MLI assembly procedure. Reasons heat leak increases during assembly are that successive layers of MLI are not uniformly wrapped around the vessel, and external particulate matter collects onto the MLI. Heat leak can be reduced by improving the IPV valve block design discussed in Section 2.1.7. Design improvements include selection of materials with lower thermal conductivity, and modification of the dimensions for components used in the current valve block design.

References

[1] Naturalgas.org Website, www.naturalgas.org, 2005.

[2] International Energy Agency Key World Statistics, 2004.

[3] Canadian natural gas vehicle alliance,www.ngvcanada.org, www.ngv.com, 2005.

[4] Q.S. Chen, J. Wegrzyn, and V. Prasad, *Analysis of temperature and pressure changes in liquefied natural gas (LNG) cryogenic tanks,* Cryogenics 44 pp. 701-709 ,2004.

[5] U.S. DOT, EPA and DOE, *Effects of the Alternative Motor Fuels Act CAFE Incentive Program*, 2002.

[6] D. Lancaster, *Some Energy Fundamentals,* The Blatant Opportunist 71, 2002.

[7] J. Wegrzyn, *Processing, Transportation and Storage of LNG*, Natural Gas Vehicle Technology Forum, 2003.

[8] J. Wegrzyn and M. Gurevich, *Liquefied Natural Gas for Trucks and Buses,* SAE Technical Paper Series, 2000.

[9] S.M. Aceves, J. Martinez-Frias and O. Garcia-Villazana, *Low Temperature and High Pressure Evaluation of Insulated Pressure Vessels for Cryogenic Hydrogen Storage*, Proceedings of the 2000 Hydrogen Program Review

[10] Westport Innovations Website, www.westport.com, 2004.

[11] Dynetek Canada Website, www.dynetek.com, 2004.

[12] G.Iuzzolino, P.Low, A.Rowe, P.Wild, *Feasibility Study for an LNG Insulated Pressure Vessel, 2004.*

[13] Wolf, J., *LH2 Makes you Mobile*, Report on Science and Technology, Linde Technology, pp 30-34, 1/2003

[14] Magna Steyr, *Liquid Hydrogen Tank,* www.magnasteyr.com/index_en.html, 2004.

[15] Salvador M. Aceves et al, *Certification Testing and Demonstration of Insulated Pressure Vessels for Vehicular Hydrogen and Natural Gas Storage*

[16] Personal Communications with Tammy Brooke of Chart Industries, May 2004

[17] Chart Industries Inc., *NexGen Fuelling Products*, www.nexgenfueling.com/products.html, 2004

[18] Taylor-Wharton, *Alternate Fuel Technologies*, www.taylor-wharton.com, 2004.

[19] F. Michel, H. Fieseler, G. Meyer and F. Theisen, *On-Board Equipment For Liquid Hydrogen Vehicles,* Int. J. Hydrogen Energy, Vol. 23, No. 3, pp. 191-199,1997.

[20] W. Peschka. *Hydrogen: The Future Cryofuel Internal Combustion Engines*. Int. J. Hydrogen Energy Vol. 23 No. 1 pp. 27-43, 1998.

[21] M. Tummula, T. Krepec, and A.K.W. Ahmed, *Optimization of Themocontrolled Tank for Hydrogen Storage in Vehicles,* Int. J. Hydrogen Energy Vol. 22 No. 5 pp. 525-530,1997.

[22] C. Cederberg, N. Newhouse, and B. Gerdes, *High Pressure Fuel Container for Hydrogen Fueled Vehicles*, General Dynamics Armament and Technical Products,2002.

[23] *High-Pressure Conformable Hydrogen Storage for Fuel Cell Vehicles*, Thiokol Propulsion, Proceedings of the 2000 hydrogen program review

[24] Quantum Technologies CH_2 and NG storage systems for vehicles Website, www.qtww.com, 2004.

[25] ANSYS Release 8.0 Helpdesk, 2004.

[26] J.S. Park, C.S. Hong, C.G Kim, Composite Structures Vol.55 (2002), p.63.

[27] W.Flügge.1973. *Stresses in Shells* (2nd ed.) New York: Springer-Verlag.

[28] H.Bednar.1986.*Pressure Vessel Design Handbook* (2nd ed.). Florida: Krieger Publishing Company.

[29] Personal communications with Teddy Townsley of Dynetek Canada, July 2004

[30] ANSI/CSA NGV 2, American National Standard for Basic Requirements for Compressed Natural Gas Vehicles (NGV) Fuel Container, CSA International, Cleveland, OH, October 2000.

[31] Barron,R, "Cryogenic Heat Transfer", Michigan: Edwards Brothers, 1999.

[32] Metals Handbook, 10th ed., vol. 1, ASM International Handbook Committee., ASM International, Materials Park, OH, (1990)

[33] US Department of Transportation Website, http://www.dot.gov/, 2005.

[34] ASME Boiler and Pressure Vessel Code Website, http://www.asme.org/bpvc/, 2005.

[35] Young, W., "Roark's Formulas for Stress & Strain", New York: McGraw-Hill, 1989.

[36] Timmerhaus and Flynn, "Cryogenic Engineering", New York: Marcel Dekker, 1997.

[37] Advanced LNG Onboard Storage System (ALOSS) Report, DOE Report Technical Report, 2003.

[38] Conversation with Greg Harper of Westport, August 2004.

Appendix A1.1 IPV Design Criteria

The IPV was designed by following a design criteria, that was developed in consultation with Westport. The design requirements are as follows.

Dimensional requirements:

- Tank diameter ~ 508-762 mm (20-30 inches).
- Tank Length < 2032 mm (80 inches).

Storage Requirements:

- Store LNG with initial conditions of approximately 115 K, 0.69 MPa(100 psig), and 90% liquid (by volume) for 5 days before pressure reaches 1.38 MPa(200 psig).
- Maximum allowable working pressure (MAWP) for first generation tanks is 1.38 MPa(200 psig).
- Fuel storage volume >318 L (75 gallons)
- Tank fuel storage density > 0.30 kg LNG / Liter of IPV

Structural Requirements:

- Designed to safely perform at up to 8g's of loading
- Outer vessel must be able to withstand 1atm of external loading while holding an internal vacuum.
- Inner vessel to have a factor of safety of 2.35 against burst [29, 30].*

* The ASME pressure vessel code requires a factor of safety of 3.5 against burst [34]. This factor of safety was not used in this report since it is believed to be too conservative for vehicular LNG storage applications [29].

Appendix A2.1 Hydrostatic Pressure Calculations

Hydrostatic pressure of LNG within the IPV vessel was calculated. An expression for hydrostatic pressure $P_{hydrostatic}$ is given in Equation A2.1.

$$P_{hydrostatic} = \rho_{LNG} g h \tag{A2.1}$$

Table A2.1 Variables used to calculate the Hydrostatic Pressure

Variable	Value	Description
ρ_{LNG}	424 kg/m^3	Density of LNG
g	9.81 m/s^2	Gravitational acceleration
h	0.5 m	Depth of LNG

Values in Table A2.1 are substituted into Equation A2.1 to give a hydrostatic pressure of 0.002 MPa (0.3 psi). If a loading of 8g is assumed, the hydrostatic pressure $P_{hydrostatic}$ becomes 2.4 psi. The hydrostatic pressure is much smaller than the proposed IPV operating pressure of 1.38 MPa (200 psi).

Appendix A2.2 Collapse Pressure Calculations

The buckling equations used in this report assume that the outer vessel is a thin tube with closed ends under uniform external pressure (lateral, and longitudinal). The dimensions used are identical to dimensions for the cylindrical section of the IPV outer vessel. Variables used are shown in Table A2.2.

Table A2.2: Variables used in Collapse Pressure Equations

Variable	**Value**	**Description**
r_{outer}	275 mm	IPV Outer Vessel Radius
t	5.25 mm	Vessel Wall Thickness
L_{vessel}	1200 mm	Outer Vessel Length
E	70 GPa	Modulus of Elasticity for Aluminum

The collapse pressure $P_{collapse}$ is given by the empirically derived Equation A2.2 [35].

$$P_{collapse} = 0.92 \cdot \frac{E}{\left(\frac{L_{vessel}}{r_{outer}}\right) \cdot \left(\frac{r_{outer}}{t}\right)^{2.5}} \qquad \text{(A2.2)}$$

$$SF = \left(\frac{P_{collapse}}{1.01 \cdot 10^5}\right) \qquad \text{(A2.3)}$$

Using Equation A2.3, the safety factor against buckling *SF* is 5. This calculation assumes an external pressure of 1 atmosphere and an internal vacuum.

Appendix A2.3 Vessel Stress and Pressure Calculations

Vessel stresses for the cylindrical region of the IPV inner vessel are calculated using standard thin-walled cylinder stress equations [35]. These equations are applicable since the radius of the vessel is greater than 5 times the wall thickness. Variables used include the vessel outer radius r_{out}, vessel inner radius r_{in}, wall thickness t, and the applied pressure P.

The radial stress is equal to the applied pressure P as shown in Equation A2.4.

$$\sigma_{radial} = P \qquad \text{(A2.4)}$$

The axial stress is given in Equation A2.5. In this equation, the vessel outer radius is r_{out}, and the vessel inner radius is r_{in}.

$$\sigma_{axial} = P \cdot \frac{r_{out}^{2}}{r_{out}^{2} - r_{in}^{2}} \qquad \text{(A2.5)}$$

The hoop stress is given in Equation A.2.6.

$$\sigma_{\theta} = P \cdot \frac{r_{out}^{2} + r_{in}^{2}}{r_{out}^{2} - r_{in}^{2}} \qquad \text{(A2.6)}$$

The total vessel stress equals the Von Mises stress given in Equation A2.7.
Equation A1.8 is solved by substituting Equation A2.4-A2.6 into Equation A2.7.

$$\sigma_{VonMises} = \sqrt{\frac{(\sigma_{axial} - \sigma_{\theta})^{2} + (\sigma_{axial} - \sigma_{radial})^{2} + (\sigma_{radial} - \sigma_{\theta})^{2}}{2}} \qquad \text{(A2.7)}$$

$$\sigma_{VonMises} = \frac{\sqrt{3}}{2} \cdot P \cdot \frac{r_{in} + r_{out}}{2} \cdot \frac{1}{t} \qquad \text{(A2.8)}$$

The design criteria given in Appendix A1.1 requires vessels to have a factor of safety *SF* against burst. Therefore, the maximum Von Mises stress is equal to the Yield Stress divided by the factor of safety as shown in Equation A2.9.

$$\sigma_{VonMises} = \frac{\sigma_Y}{SF} \qquad \text{(A2.9)}$$

Equation A2.10 gives an expression for the vessel pressure versus wall thickness for a vessel assuming a factor of safety *SF* against burst. This equation is derived by substituting Equation A2.9 into Equation A2.10.

$$P = t\left(\frac{\sigma_Y}{SF}\cdot\frac{4}{\sqrt{3}}\cdot\frac{1}{2r_{out}-t}\right) \qquad \text{(A2.10)}$$

Appendix A3.1 Heat Leak Calculations

A procedure to determine heat leak for an insulated pressure vessel was developed. Heat leak is determined by calculating the thermal resistance of each component and the intermediate temperatures at various component locations (nodes). Heat leak and thermal resistance equations are obtained from cryogenic design textbooks [31,36].

The heat leak through a component is determined using Equation A3.1.

$$Q = \frac{T_2 - T_1}{R} = S \cdot (K(T_2) - K(T_1)) \tag{A3.1}$$

In Equation A3.1, R is the thermal resistance of the component, and S is the shape factor given in Equation A3.2. The shape factor is calculated using a cross-sectional area $A(x)$, and a component position that varies from x_1 to x_2. The components thermal conductivity $K(T)$ is defined using empirically derived equations contained in this appendix. In Equation A3.1 the temperature of the component varies from T_1 to T_2.

$$\frac{1}{S} = \int_{x1}^{x2} \frac{dx}{A(x)} \tag{A3.2}$$

The iterative procedure listed below was used to obtain the intermediate temperatures.

1) Calculate thermal resistances R, and heat leaks Q assuming that the temperatures at each node of the network diagram is constant.

2) Re-estimate the nodal temperatures using the thermal resistance R, and heat leak Q values from step 1, and the equation $\Delta T=QR$

3) Re-estimate the thermal resistances R, and heat leaks Q using the temperatures obtained in step 2.

4) Go to step 2. Continue iterations until temperatures at each node converge.

Appendix A3.1.1 IPV Heat Leak Calculations

The external (ambient) temperature T_H is 300 K and the internal pressure vessel temperature T_C is 115 K. The thermal network of the IPV is given in Figure A3.1.1.

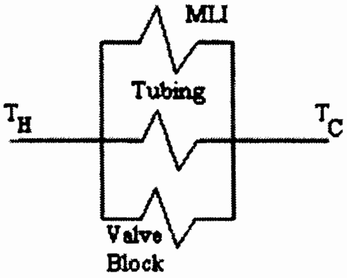

Figure A3.1.1: Thermal network diagram for IPV

Valve Block Structure

This section calculates the heat leak of the valve block shown in Figure A3.1.2. The thermal network for the valve block is shown in Figure A3.1.3.

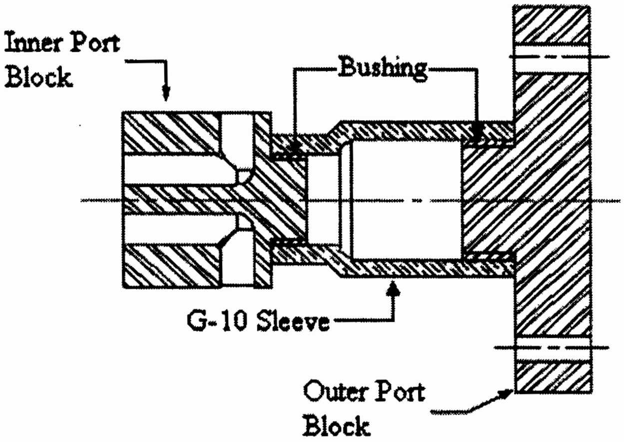

Figure A3.1.2: Section view of Valve Block

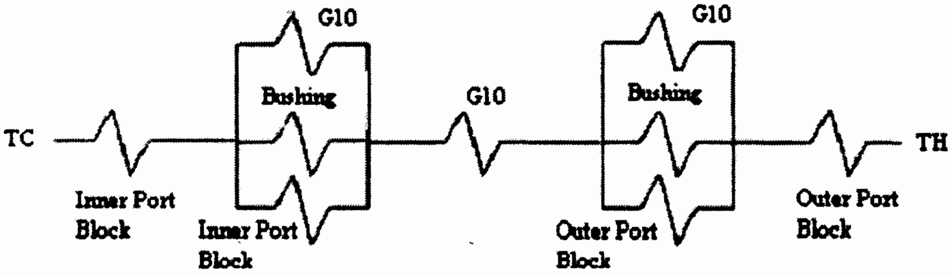

Figure A3.1.3: Thermal network diagram for Valve Block

The inner and outer port block's shape factor (Equation A3.3) is calculated using a port block length L_{block} of 0.06 m, inner radius r_{in} of 0.02 m, and outer radius r_{out} of 0.026 m.

$$S_{block} = \pi \cdot \frac{(r_{out}^{2} - r_{in}^{2})}{L_{block}} = 1.4 \times 10^{-2} m \tag{A3.3}$$

The thermal conductivity integral for the steel port blocks, and bushings is given in Equation A3.4 [31,36].

$$K_{steel}(T) = -0.0002\frac{T^{3}}{3} + \frac{0.1183}{2} \cdot T^{2} - 0.0578 \cdot T \tag{A3.4}$$

The inner and outer port block resistances are calculated using Equations A3.5-A3.6. The outer port block's external end has a temperature T_H, and the internal end has a temperature $T_{C(outer)}$ of 291 K. The inner port block's internal end has a temperature T_C and the external end has a temperature $T_{H(inner)}$ of 125 K.

$$R_{innerblock} = \frac{(T_{H(inner)} - T_{C(inner)})}{(K_{steel}(T_{H(inner)}) - K_{steel}(T_{C(inner)})) \cdot \frac{1}{S_{block}}} = 1.4 \cdot 10^{-3} KW^{-1} \tag{A3.5}$$

$$R_{outerblock} = \frac{(T_{H} - T_{C(outer)})}{(K_{steel}(T_{H}) - K_{steel}(T_{C(outer)})) \cdot \frac{1}{S_{block}}} = 8.3 \cdot 10^{-4} KW^{-1} \tag{A3.6}$$

The shape factor for the bushings is calculated using Equation A3.7. A bushing length $L_{bushing}$ of 0.01 m, an inner bushing radius r_{in} of 0.015 m, and an outer bushing radius r_{out} of 0.02m are used.

$$S_{bushing} = \frac{r_{out}^{2} - r_{in}^{2}}{L_{bushing}} = 0.055\ m \tag{A3.7}$$

The bushing resistance is calculated using Equations A3.8. The temperature of the bushing's external end $T_{C(outer)}$ is 291 K, and the temperature of the bushing's internal end $T_{H(G\text{-}10)}$ is 288K.

$$R_{bushing} = \frac{(T_{H(G-10)} - T_{C(outer)})}{(K_{steel}(T_{H(G-10)}) - K_{steel}(T_{C(outer)})) \cdot \frac{1}{S_{bushing}}} = 3.6 \cdot 10^{-3} KW^{-1} \quad \text{(A3.8)}$$

The shape factor for the G-10 region that is not occupied by the bushing is given in Equation A3.9. It is calculated assuming the G-10 length L_{G-10} is 0.05m, the inner radius of G-10 r_{in} is 0.0018m, and the outer radius of G-10 r_{out} is 0.0028m.

$$S_{G-10} = \pi \cdot \frac{(r_{out}^2 - r_{in}^2)}{L_{G-10} - 2 \cdot L_{Bushing}} = 0.059 \ m \quad \text{(A3.9)}$$

The thermal conductivity integral for the G-10 region $K_{G-10}(T)$ is given in Equation A3.10 [32].

$$K_{G-10}(T) = \frac{2 \cdot 10^{-8}}{4} \cdot T^4 - \frac{0.00002}{3} \cdot T^3 + \frac{0.0051}{2} \cdot T^2 + 0.0828 \cdot T \quad \text{(A3.10)}$$

The G-10 regions resistance is calculated using Equations A3.11. The inner valve block external end temperature $T_{H(G-10)}$ is 288 K, and the internal end temperature $T_{C(G-10)}$ is 130 K.

$$R_{G-10} = \frac{(T_{H(G-10)} - T_{C(G-10)})}{(K_{G-10}(T_{H(G-10)}) - K_{G-10}(T_{C(G-10)})) \cdot (\frac{1}{S_{G-10}})} = 38.8 KW^{-1} \quad \text{(A3.11)}$$

The resistance of the region occupied by the bushings is calculated in Equation A3.12. The bushing resistance term is the sum of the resistances in the bushing, and the portion of G-10 and port block in the bushing region.

$$R_{bushing\_region} = \left(\frac{1}{R_{G10} \cdot \left(\frac{L_{bushing}}{L_{G-10}} \right)} + \frac{1}{R_{bushing}} + \frac{1}{\frac{R_{pins(low)} + R_{pins(high)}}{2} \cdot \left(\frac{L_{bushing}}{L_{pin}} \right)} \right)^{-1} \quad \text{(A3.12)}$$

The total resistance for the valve block given in Equation A3.13 is calculated by adding the resistances of the port blocks, G-10 connector, and bushing region.

$$R_{ValveBlock} = R_{OuterBlock} + R_{InnerBlock} + R_{G-10} + 2 \cdot R_{Bushing\_region} = 38.6 \ KW^{-1} \qquad (A3.13)$$

The total heat leak for the valve block is calculated in Equation A3.14.

$$Q_{ValveBlock} = \frac{T_H - T_C}{R_{ValveBlock}} = 2.1 \ W \qquad (A3.14)$$

Rear Support

This section calculated the heat leak of the rear support shown in Figure A3.1.4. The rear support consists of a stainless steel support plate that is connected to the outer vessel. A thermal network of the rear support is shown in Figure A3.1.5.

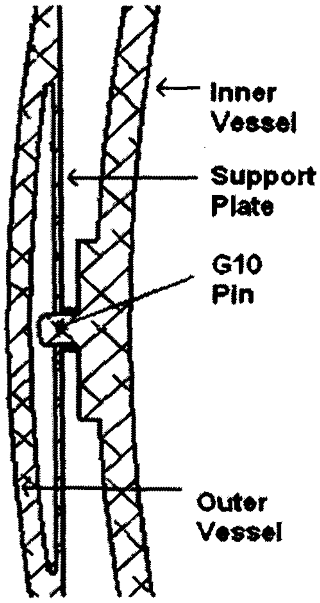

Figure A3.1.4: Section view of Rear Support

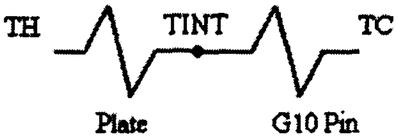

Figure A3.1.5: Thermal network diagram of Rear Support

The inner vessel is supported by the rear support using a G-10 pin. The G-10 pin has a heat path along the cross-sectional area of the plate. Variables used to calculate the plates shape factor S_{plate}, and the pins shape factor $S_{G\text{-}10}$ are given in Table A3.1. The plate and G-10 dimensions were obtained from Westport drawings [37]. The plate boundary temperatures are the ambient temperature T_H and the temperature where the G-10 pin and plates are connected T_{INT}. The G-10 pin has boundary temperatures of T_C and T_{INT}. The internal vessel temperature is T_C.

Table A3.1: Variables used to determine the Rear Support Heat Leak

Variable	Value	Description
A_{plate}	$1.1\cdot10^{-4}$m^2 (0.17 in^2)	Cross-sectional plate Area
L_{plate}	0.33 m (13 in)	Plate length
A_{G10}	0.015 m^2 (0.59 in^2)	Cross-sectional G10 Pin Area
L_{G10}	0.012 m (0.47 in)	G10 Pin Length

The shape factor of the support plate, and G10 pin are given in Equation A3.15-A3.16.

$$S_{plate} = \frac{2\cdot A_{plate}}{0.5\cdot L_{plate}} = 1.34\cdot10^{-3}m \qquad \text{(A3.15)}$$

$$S_{G-10} = \frac{2\cdot A_{G-10}}{0.5\cdot L_{G-10}} = 0.037m \qquad \text{(A3.16)}$$

The middle of the plate has a temperature T_C of 115K and the ends of the plate have a temperature T_H of 300K. The intermediate temperature of 220 K was found using the iterative procedure mentioned at the beginning of Appendix A3.1. The plate thermal conductivity integral $K_{steel}(T)$ is given in Equation A3.2, and the G-10's thermal conductivity integral $K_{G\text{-}10}(T)$ is calculated in Equation A3.17 [31,36].

$$K_{G-10}(T) = \frac{-2\cdot10^{-8}}{4}\cdot T^4 + \frac{0.00002}{3}\cdot T^3 + \frac{0.0051}{2}\cdot T^2 + 0.0828\cdot T \qquad \text{(A3.17)}$$

The resistances of the G-10 pin R_{G10} and plate R_{plate} are given in Equations A3.18-A3.19.

$$R_{G-10} = \frac{(T_{INT} - T_C)}{(K_{G-10}(T_{INT}) - K_{G-10}(T_C))\cdot S_{G-10}} \qquad \text{(A3.18)}$$

$$R_{plate} = \frac{(T_H - T_{INT})}{(K_{steel}(T_H) - K_{steel}(T_{INT}))\cdot S_{plate}} \qquad \text{(A3.19)}$$

The heat leak through the rear support is given in Equation A3.20.

$$Q_{back\,support} = \frac{(T_H - T_C)}{R_{G-10} + R_{plate}} = 1.80\,W \tag{A3.20}$$

Multi Layer Insulation

MLI is wrapped around the inner vessel. MLI effective thermal conductivities vary depending on the type of materials that are used in the MLI and production techniques used to fabricate the MLI. Heat leak from the MLI is determined using the empirically derived equations that determine effective thermal conductivity k_t [31,36].Variables used to solve for the heat leak in the IPV occurring in region containing MLI are given in Table A3.2

Table A3.2: Variables used to calculate heat leak for MLI

Variable	Value	Description
ε	0.04	Emissivity of MLI
σ	$5.67 \cdot 10^{-8} \mathrm{Wm^{-2}K^{-2}}$	Stefan Boltzman constant
N	15	Number of MLI Layers
ΔX	0.01 m	Thickness of MLI Layers
$L_{cylinder}$	1.524 m	IPV's cylindrical region length
r	0.28 m	Radius of cylindrical region
A	$2.68\ \mathrm{m^2}$	MLI surface area
C_S	$3.4 \cdot 10^{-13} \mathrm{Wm^{0.56}K^{-2}}$	Coefficient for Mylar MLI

Equations A3.21-A3.22 give the convection heat transfer coefficient and thermal conductivity for MLI using Mylar.

$$hc_{Mylar} = Cs \cdot (T_H + T_C) \cdot \left(\frac{N}{\Delta X}\right)^{2.56} = 0.019 \tag{A3.21}$$

$$kt_{Mylar} = \frac{hc_{Mylar} + \sigma\varepsilon(T_H{}^2 + T_C{}^2)\dfrac{(T_H + T_C)}{(2-\varepsilon)}}{\dfrac{N}{\Delta X}} = 4.52 \cdot 10^{-5} \tag{A3.22}$$

The heat leak through the MLI is calculated using Equation A3.23.

$$Q_{MLI} = kt_{Mylar} \cdot A \cdot \left(\frac{T_H - T_C}{\Delta X} \right) = 2.28\,W \tag{A3.23}$$

Tubing

This section determines heat leak in the IPV stainless steel tubing. The IPV will use one length of tubing to fill the IPV with fuel, and a second length of tubing to transfer fuel from the IPV to the engine. Only the thermal conductivity in the longitudinal direction is considered in heat leak calculations.

Table A3.3 Variables used to calculate heat leak in tubing

Variable	Value [m]	Description
L_{tubing}	0.125	Length of Tubing
t	0.0002	Thickness of Tubing
r_{out}	0.0048	Outer radius of tubing

Values in Table A3.3 are used to calculate the shape factor S_{tubing} in Equation A3.24. The heat leak in the tubing is given in Equation A3.25.

$$S_{tubing} = \pi \cdot \frac{r_{out}^{\,2} - (r_{out} - t)^2}{L_{tubing}} \tag{A3.24}$$

$$Q_{tubing} = (K_{steel}(T_H) - K_{steel}(T_C)) \cdot S_{tubing} = 0.136\ W \tag{A3.25}$$

There are two lengths of tubing so the heat leak for the tubing is $2Q_{tubing}$ which equals 0.27 W.

Total Heat Leak occurring in the IPV

The IPV's total heat leak equals the sum of the heat leaks in the tubing, valve blocks, MLI, and supports as shown in Equation A3.26.

$$Q = 2 \cdot Q_{tubing} + Q_{valveblock} + Q_{MLI} + Q_{support} = 6.5\ W \tag{A3.26}$$

Appendix A3.1.2 ALOSS Heat Leak Calculations

The heat leak and boil off rate for Westport's Advanced LNG Onboard Storage System (ALOSS) pressure vessel [37] are calculated so that theoretical values can be compared with experimental values. If the values are close this will give indication that the theoretical models for the prototype IPV are valid.

Regions of significant heat leak are the structural supports, MLI, and the pump The MLI is wrapped around the inner wall of the pressure vessel. The structural supports are used to support the inner pressure vessel. The pump is used to deliver fuel from the storage vessel to the engine. The thermal network for the ALOSS vessel is identical to the IPV's thermal network shown in Figure A3.1.1. The ambient temperature T_H is assumed to be 300K and the inner pressure vessel temperature T_C is assumed to be 140K.

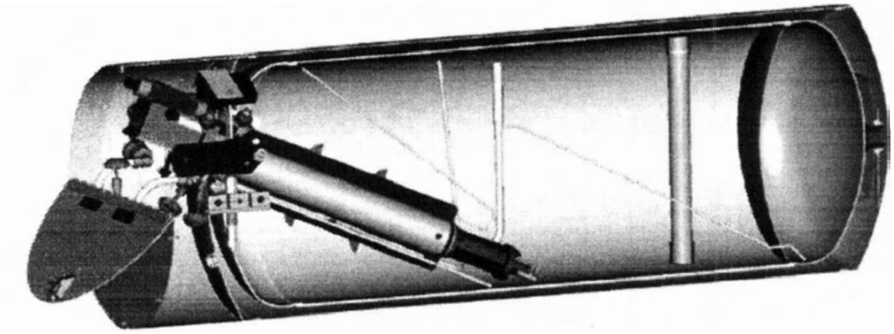

Figure A3.1.6: Section view of IPV

Structural Supports

The front and rear structural supports consist of a rectangular steel plate on the outer vessel that is mated with pins on the inner vessel (Figure A3.1.4). The shape factor S_{plate} for the stainless steel plate shown in Equation A3.27 is calculated using the parameters listed in Table A3.1.The plate has boundary temperatures of T_H and T_C. The plate dimensions were obtained from Westport drawings [38].

$$S_{plate} = \frac{2A_{plate} \cdot (0.0254)}{0.5 \cdot L_{plate}} = 1.34 \cdot 10^{-3}\, m \qquad \text{(A3.27)}$$

The heat leak occurring in each support Q_{plate} was calculated in Equation A3.28. The effective thermal conductivity $K_{steel}(T)$ term was calculated using Equation A3.4.

$$Q_{plate} = S_{plate} \cdot (K_{steel}(T_H) - K_{steel}(T_C)) \qquad \text{(A2.28)}$$

Since the ALOSS vessel uses two supports, the total heat leak occurring in the supports $Q_{supports}$ is $2Q_{plate}$ which equals 6.8 W.

Multi Layer Insulation

MLI is wrapped around the ALOSS inner vessel. Heat leak through the MLI is determined using the empirically derived equations [31,36] that determine effective thermal conductivity k_t. It is assumed that the MLI is wrapped around a Westport ALOSS vessel. Variables used to solve for the heat leak in the IPV occurring in region containing MLI are given in Table A3.4. The Westport drawings did not provide complete details regarding the MLI design. Therefore, some of the variables listed in Table A3.4 are assumed.

Table A3.4: Variables used to calculate heat leak for MLI in ALOSS IPV

Variable	Value	Description
ε	0.04	Emissivity of MLI
σ	$5.67 \cdot 10^{-8}$W m^{-2} K^{-4}	Stefan Boltzman constant
N	24	Number of MLI Layers
ΔX	0.01m	Thickness of MLI Layers
$L_{cylinder}$	0.954	IPV cylindrical region length
r	0.305m	Radius of cylindrical region
A	1.83m^2	MLI surface area
C_S	$3.4 \cdot 10^{-13}$Wm$^{0.56}$K^{-2}	Coefficient for Mylar MLI

Equations A3.20-A3.21 give the convection heat transfer coefficient h_c and thermal conductivity $k_{t(Mylar)}$ for MLI using Mylar. The heat leak through the MLI is calculated in Equation A3.29.

$$Q_{MLI} = k_{t(mylar)} \cdot A \cdot \frac{(T_H - T_C)}{\Delta X} = 1.5\ W \qquad \text{(A3.29)}$$

Pump Shaft

The pump shaft is contained within the pump housing of the Westport ALOSS vessel. The shaft transports LNG at a temperature of T_C. Therefore one end of the shaft is at a temperature of T_C, and the other end is at a temperature of T_H. Only the thermal conductivity in the longitudinal direction is considered. The pump shaft dimensions were obtained from Westport drawings [37,38].

The shape factor for the pump shaft is given in Equation A3.30. It is calculated assuming the length of the pump shaft L_{shaft} is 0.55m, and the radius of the pump shaft r_{shaft} is 0.0125m.

$$S_{shaft} = \frac{\pi \cdot (r_{shaft})^2}{L_{shaft}} \tag{A3.30}$$

The heat leak for the pump shaft Q_{shaft} is given in Equation A3.31.

$$Q_{shaft} = (K_{steel}(T_H) - K_{steel}(T_C)) \cdot S_{shaft} = 2.27\ W \tag{A3.31}$$

Pump Shaft Internal Housing

The pump shaft's internal housing surrounds the pump shaft of the Westport ALOSS vessel. The pump shaft housing is in contact with the pump shaft. Therefore one end of the shaft is at a temperature of T_C, and the other end is at a temperature of T_H. The pump shaft dimensions shown in Table A3.5 are obtained from Westport drawings [37,38].

Table A3.5 Variables used to calculate heat leak for pump shaft internal housing

Variable	Value	Description
$L_{housing}$	0.55 m	Length of Internal Housing
$t_{housing}$	$1.24 \cdot 10^{-3}$m	Thickness of internal Housing
$r_{housing}$	0.05 m	Radius of internal Housing

The shape factor for the pump housing $S_{housing}$ is calculated in Equation A3.32 using variables given in Table A3.5.

$$S_{hou\sin g} = \pi \cdot \left(\frac{r^2{}_{hou\sin g} - (r_{hou\sin g} - t_{hou\sin g})^2}{L_{hou\sin g}} \right) \tag{A3.32}$$

The pump housing's heat leak $Q_{housing}$ is given in Equation A3.33.

$$Q_{hou\sin g} = (K_{steel}(T_H) - K_{steel}(T_C)) \cdot S_{hou\sin g} = 1.8\ W \tag{A3.33}$$

Total Heat Leak occurring in the Pressure Vessel

The total heat leak that occurs in the pressure vessel is equal to the sum of the heat leaks in the housing, supports, MLI, and pump shaft as shown in Equation A3.34.

$$Q_{total} = Q_{hou\sin g} + Q_{\sup ports} + Q_{MLI} + Q_{shaft} = 12.4\ W \tag{A3.34}$$

The experimentally determined heat leak was 20.1 W [37].Predicted ALOSS heat leak under-estimates the experimental heat leak because only heat leak occurring from the major components of the ALOSS vessel was considered. Additionally, the actual heat leak may be higher since the MLI thermal conductivity values in real applications are rarely as good as the values determined in controlled laboratory tests.

Appendix A3.2 Hold Time Calculations

Hold time is a measure of the amount of time required for the LNG pressure to build up to a critical vent pressure when the tank is closed to the external environment. Hold time t_{hold} is calculated using Equation A3.26. In this equation, Q is the total heat leak as determined in Appendix A3.1, m_{LNG} is the mass of the LNG contained in the storage vessel, and u_2-u_1 is the change in internal energy of the LNG as its pressure builds up from its initial operating pressure to a final vent pressure.

The change in internal energy, u_2-u_1, is calculated using the following procedure. First, the density of the LNG is determined by calculating the total LNG mass divided by the combined tank volume and ullage space. The internal energy u_1 is obtained at the LNG operating pressure by assuming that the operating temperature equals the liquefaction temperature, and using the calculated LNG density value. The LNG is assumed to have a constant density as the pressure builds up to the vent pressure. This assumption is made because the process involves a closed volume with a constant LNG mass. The internal energy u_2 is obtained when the pressure reaches the vent pressure and the internal energy is u_2.

$$Q = \frac{dU}{dt} = m_{LNG} \cdot \frac{u_2 - u_1}{\Delta t} = Heat\ Leak \qquad \text{(A3.25)}$$

Hold time is defined in Equation A3.26 which was derived by rearranging equation A3.25.

$$t_{hold} = \Delta t = \frac{(u_2 - u_1) \cdot m_{LNG}}{Q} \qquad \text{(A3.26)}$$

Table A3.4: Values used to Calculate Hold Time

Description	**IPV**	**Taylor Wharton**
Initial LNG pressure	0.69 MPa(100 psi)	0.69 MPa(100 psi)
Final vent pressure	1.38 MPa(200 psi)	1.62 MPa(235 psi)
Tank volume	318 litres	257 liters
Ullage fraction	16 %	16%
Heat leak	6.5 W	20.1 W

Substitution of values in Table A3.4 into Equation A3.26 gives an IPV hold time of 209 hours.

Unfortunately, there is no experimental data that can be used to validate hold time calculations for the IPV. However, the hold time was experimentally determined for the ALOSS vessel. Westport's experimental results indicate that the ALOSS design has a hold time of 60 hours [37]. The hold time was calculated using Equation A3.26 and values in Table A3.1. Calculated hold time is 89 hours. One reason for the discrepancy between calculated and experimental hold time is the uncertainty in the MLI thermal conductivity caused due to non-ideal MLI installation. However, experimental results are within 30% of calculated results which helps validate the calculated IPV hold time of 209 hours.

Appendix A3.3 Estimation of the Boil off Rate

The boil off rate $m_{boil\ off}$ for the IPV is a function of the total heat leak Q, and enthalpy values for methane in its liquid state h_f, and its gas state h_g. Enthalpy values for methane at 115 K and 1 atm are given in Equation A3.27.

$$\begin{aligned} h_f &= -911 kJ/kg \\ h_g &= -400 kJ/kg \\ h_{fg} &= h_g - h_f \end{aligned} \tag{A3.27}$$

The boil off rate measured in gram per hour [g/hour] is given in Equation A3.28. The IPV heat leak of 6.5 W that was calculated in Appendix A3.1 was used.

$$m_{boil\_off} = \frac{Q}{h_{fg}} = 45.2\ g/hour \tag{A3.28}$$

A similar calculation was made for Westport's ALOSS vessel [37]. The experimentally obtained heat leak of 20 W was used. The boil off rate was calculated to be 126 g/hr. This value is comparable to the experimentally determined boil off rate of 146 g/hr.

Appendix A3.4 Fuel Mass and Ullage Fraction Calculations

Ullage space is the volume the IPV requires to store excess fuel from the inner vessel. This section presents the equations used to calculate fuel mass and ullage space.

A3.4.1 Ullage Fraction Calculations

Ullage fraction V_{ullage}/V_{total} is calculated using Equation A3.29. The variable X represents the vapor mass fraction m_{vapor}/m_{total}.

$$\frac{V_{ullage}}{V_{total}} = \frac{m_{vapor}}{m_{total}} \cdot \frac{\rho_{total}}{\rho_{vapor}} = X \cdot \left(\frac{\rho_{total}}{\rho_{vapor}} \right) \tag{A3.29}$$

The expression for ullage fraction V_{ullage}/V_{total} in Equation A3.30 is obtained by expressing the total fuel density ρ_{total} as a function of the liquid and vapor densities, and the ullage volume and total volume.

$$\frac{V_{ullage}}{V_{total}} = X \frac{1}{\rho_{vapor}} \left(\rho_{liquid} \cdot \left(1 - \frac{V_{ullage}}{V_{total}} \right) + \rho_{vapor} \cdot \left(\frac{V_{ullage}}{V_{total}} \right) \right) \tag{A3.30}$$

Equation A3.30 is rearranged to give the expression for ullage fraction shown in Equation A3.31.

$$\frac{V_{ullage}}{V_{total}} = X \cdot \frac{\left(\frac{\rho_{liquid}}{\rho_{vapor}} \right)}{1 + X \cdot \left(\frac{\rho_{liquid}}{\rho_{vapor}} \right) - X} \tag{A3.31}$$

Ullage fraction is calculated by solving for several variables using the following procedure. First, the LNG's liquid and vapor density are determined at the starting pressure. The LNG density is assumed to be constant since the LNG mass and storage volume remain constant while being stored. Therefore, an isochore (constant density curve) is used to determine LNG thermal properties as pressure increases. The LNG density is determined at the end pressure by assuming a 100% liquid full condition at the end pressure. The mass fraction X was determined at the start pressure.

A3.4.2 Fuel Mass Calculations

IPV fuel storage volume (V_{total}) is the sum of the fuel volume V_{liquid} and the ullage volume V_{ullage}. Equation A3.32 gives an expression for IPV volume.

$$V_{total} = V_{liquid} + V_{ullage} \tag{A3.32}$$

Fuel mass (m_{total}) is the sum of the fuel's liquid mass m_{liquid} and the fuel's vapor mass m_{vapor}. Equation A3.33 gives an expression for fuel mass.

$$m_{total} = m_{liquid} + m_{vapor} \tag{A3.33}$$

Equation A3.34 is obtained by entering Equation A3.32 into Equation A2.33. In this equation ρ_{liquid} is the fuel's liquid density and ρ_{vapor} is the fuel's vapor density.

$$m_{total} = (\rho_{liquid} \cdot V_{liquid}) + (\rho_{vapor} \cdot V_{ullage}) \tag{A3.34}$$

Fuel mass is calculated by solving for the fuel's liquid density and vapor density at the starting pressure. Liquid volume and ullage volume at a given maximum pressure are determined using ullage fraction calculations described in Appendix A3.4.1.